NAVAL AIR WARFARE CENTER AIRCRAFT DIVISION
PATUXENT RIVER, MARYLAND

TECHNICAL REPORT

REPORT NO: NAWCADPAX--97-257-TR

COPY NO. _____

COMPUTATIONAL FLUID DYNAMICS TOOLS FOR ESCAPE SYSTEMS AERODYNAMIC ANALYSIS

Volume 1 of 2

9 February 1998

Approved for public release; distribution is unlimited.

REPORT DOCUMENTATION PAGE

Form Approved
OMB No. 0704-0188

1. AGENCY USE ONLY *(LEAVE BLANK)*	2. REPORT DATE	3. REPORT TYPE AND DATES COVERED
	9 February 1998	

4. TITLE AND SUBTITLE

Computational Fluid Dynamics Tools for Escape Systems Aerodynamic Analysis (Volume 1 of 2)

5. FUNDING NUMBERS

6. AUTHOR(S)

S. D. Habchi V. J. Parsatharsay
S. G. Rock A. J. Przekwas
G. S. Hufford Contract No. N62269-92-C-0248

7. PERFORMING ORGANIZATION NAME(S) AND ADDRESS(ES)

CFD Research Corporation
3325 Triana Blvd.
Huntsville, Alabama 35805

8. PERFORMING ORGANIZATION REPORT NUMBER

NAWCADPAX--97-257-TR
CFDRC Report 4128/17

9. SPONSORING/MONITORING AGENCY NAME(S) AND ADDRESS(ES)

Naval Air Warfare Center Aircraft Division
22347 Cedar Point Road Unit #6
Patuxent River, Maryland 20670-1161

10. SPONSORING/MONITORING AGENCY REPORT NUMBER

11. SUPPLEMENTARY NOTES

Project Coordinator: Thomas J. Marquette (Code 4.6.2.1)
Naval Air Warfare Center Aircraft Division
Patuxent River, Maryland 20670

12a. DISTRIBUTION/AVAILABILITY STATEMENT

Approved for public release; distribution is unlimited.

12b. DISTRIBUTION CODE

13. ABSTRACT *(Maximum 200 words)*

This report documents the findings of a SBIR Phase II study entitled "CFD Analysis of Drag Reduction on an Ejection Seat During High Speed Ejection". The main objectives of this study were to develop and validate Computational Fluid Dynamics (CFD) methodologies for comprehensive aerodynamic analysis of ejection seat and occupant in free flight, and develop and adapt existing CFD technologies for analysis of ejection seat in proximity of aircraft for both steady-state and unsteady seat and aircraft separation using prescribed trajectory.

14. SUBJECT TERMS	15. NUMBER OF PAGES
Computational Fluid Dynamics (CFD)	130
	16. PRICE CODE

17. SECURITY CLASSIFICATION OF REPORT	18. SECURITY CLASSIFICATION OF THIS PAGE	19. SECURITY CLASSIFICATION OF ABSTRACT	20. LIMITATION OF ABSTRACT
Unclassified	Unclassified	Unclassified	SAR

CFD Research Corporation
3325 Triana Blvd. • Huntsville, Alabama 35805 • Tel.: (205) 536-6576 • FAX: (205) 536-6590 • info@cfdrc.com

COMPUTATIONAL FLUID DYNAMICS TOOLS

FOR ESCAPE SYSTEMS AERODYNAMIC ANALYSIS

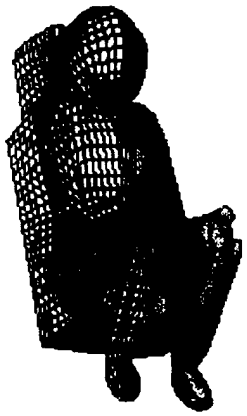

Final Report

Volume 1 of 2

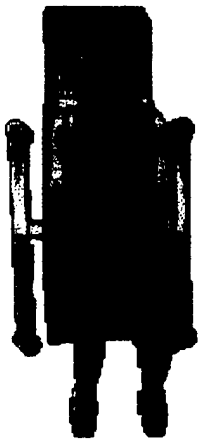

by

S.D. Habchi, S.G. Rock, G.S. Hufford, V.J. Parsatharsay and A.J. Przekwas

for

Naval Air Warfare Center - Aircraft Division
Patuxent River NAS
Lexington Park, MD 20670
Contract No.: N62269-92-C-0248
Project Coordinator: Thomas J. Marquette

CFD Research Corporation
3325 Triana Blvd. • Huntsville, Alabama 35805 • Tel.: (205) 536-6576 • FAX: (205) 536-6590 • info@cfdrc.com

COMPUTATIONAL FLUID DYNAMICS TOOLS FOR ESCAPE SYSTEMS AERODYNAMIC ANALYSIS

Final Report

Volume 1 of 2

by
S.D. Habchi, S.G. Rock, G.S. Hufford, V.J. Parsatharsay and A.J. Przekwas

December 1996

CFDRC Report 4128/17

for
Naval Air Warfare Center (NAWC)
Patuxent River NAS
Lexington Park, MD 20670

Under Contract No.: N62269-92-C-0248
Project Coordinator: Thomas J. Marquette, Code 6032

SUMMARY

This report documents the findings of a SBIR Phase II study entitled "CFD Analysis of Drag Reduction on an Ejection Seat During High Speed Ejection". The main objectives of this study were twofold:

- develop and validate Computational Fluid Dynamics (CFD) methodologies for comprehensive aerodynamic analysis of ejection seat and occupant in free flight; and
- develop and adapt existing CFD technologies for analysis of ejection seat in proximity of aircraft for both steady-sate and unsteady seat and aircraft separation using prescribed trajectory.

Mechanical Computer Aided Engineering tools were developed for geometry modeling and algebraic grid generation of ejection seat and occupant and relevant aircraft components. Also an elliptic grid generator was developed for the smoothing of the escape systems grids and for grid clustering and orthogonality control. The grid generator includes a model for adjustment of seat and occupant grids for various pitch and yaw attitudes. Several geometry models and computational grids were created for the NACES seat and occupant, ACES-II seat and occupant, F-16 aircraft including cockpit and F-18 aircraft including cockpit. These computational grids were used for several computational analysis to validate and demonstrate the developed CFD technologies.

The CFD-ACE code was adapted for ejection seat and occupant aerodynamic analysis. A comprehensive assessment of differencing schemes and turbulence modeling was conducted and several guidelines were developed for ejection seat applications. Two high order differencing schemes including Second-Order upwind and Osher-Chakravarthy schemes were implemented in the CFD-ACE code for escape system applications. A force and moment integration module was also developed and implemented into CFD-ACE to calculate the aerodynamic coefficients for the ejection seat and occupant in any orientation and in several body axis systems. Also a seat/ occupant attitude control module was implemented into CFD-ACE for unsteady simulation of seat and occupant configurations.

Two new multiple and moving bodies technologies were developed and implemented in the CFD-FASTRAN code for seat and aircraft analysis. The first one features a hybrid-overset gridding technique that utilizes structured and unstructured grids. The second one relies on traditional Chimera overset gridding techniques to model multiple bodies using multiple grid systems. The Chimera technique was adopted for seat and aircraft separation analysis. This Chimera technique features several new techniques, such as Alternating Digital tree, for automatic and efficient handling of hole cutting and tree searching interpolations.

An extensive demonstration and validation study was conducted under this project to validate the developed and adapted CFD tools. This study was performed in a systematic manner that emphasized validating the basic capabilities of the tools on simple benchmark problems first, and then validating the tools for actual seat and occupant, and seat and aircraft configurations. CFD-ACE was validated for several benchmark blunt body problems including cylinder, half cylinder and sphere problems. CFD ACE was also validate using seat/occupant geometries that included the NACES and ACES-II seat and occupants. An extensive CFD-ACE validation was also conducted using the B-1A escape capsule. CFD predictions were compared to wind tunnel test data for the ACES-II seat and B-1A escape capsule. Excellent agreement was obtained for most of the problems. For the majority of test cases, the CFD predictions were within 5-10 percent of the wind tunnel test data.

CFD-FASTRAN was also validated on an ACES-II and occupant configuration and ACES-II in proximity to F-16 configuration. CFD-FASTRAN predictions compared very well to test data for most of the calculations. Several other demonstration studies including unsteady seat separation from the aircraft were successful as correct and expected flow patterns were predicted.

In summary all the objectives of this SBIR study were accomplished. The CFD tools have already been used in several Phase III efforts for ejection seat design and qualification purposes. Most of the CFD tools have already been delivered to the Navy and are being used by Navy engineers for solving ejection seat and occupant aerodynamics problems.

CFDRC plans to continue various Phase III applications under different non-SBIR contracts from Navy and Industry. Last but not least, the developed tools and experience are also of considerable value in the commercialization of CFDRC software including geometry modelor and grid generator (CFD-GEOM), CFD flow solvers (CFD-ACE and CFD-FASTRAN) and flow visualization software (CFD-VIEW).

PREFACE

This is the final report for an SBIR Phase II study entitled "CFD Drag Reduction on an Ejection Seat During High Speed Ejection". This project was sponsored by the U.S. Navy, Naval Air Warfare Center, Aircraft Division (NAWC-A/D), under contract number N62269-92-C-0204, and conducted by CFD Research Corporation (CFDRC) under project number 4128. The principal investigator of this work was Mr. Sami D. Habchi of CFDRC and the Navy technical monitor was Mr. Thomas J. Marquette of NAWC-A/D. This contract started in April 1992. The original completion date was April 1994, however, in the spring of 1994 the contract was extended (with additional tasks and cost) until June 1996. This final report present results of the 4 year effort including the extension.

This report is divided into two volumes:

- Volume 1: Section 1 through Section 5, describing all seat and occupant methodology development CFD tools adaptations, demonstrations and validations; and

- Volume 2: Section 6 through Section 9, describing methodology selection and development for seat aircraft analysis, along with demonstration and validation results. Volume 2 also includes the conclusion and recommendations for this study.Volume 2 also includes Appendix A which includes all the technical papers documenting the work performed under this contract.

The authors of this report would like to thank the following individuals for their contributions to the overall success of this project:

- Dr. Simon Ho for his help in the NACES geometric modeling and flow analysis process.

- Mr. Mark Ostrander for his help in the OVERFLOW code simulations.

- Dr. Curtis Mitchell of CFDRC for his help in the Overset-Hybrid gridding methodology development and implementation and other CFD-FASTRAN code support and development.

- Dr. Z.J. Wang of CFDRC for his support and advice in the traditional Chimera development and implementation into CFD-FASTRAN, and for CFD-FASTRAN code support.

- Dr. Ken Wintzler of WL/FIMC for providing geometry and surface models for B-1A capsule.

- Dr. Ashok K. Singhal of CFDRC for his overall guidance and direction throughout this effort.

- Mr. Thomas J. Marquette of NAWC-A/D for his active participation in all phases of this work and his suggestions and contributions especially in the validation and design concept assessment tasks.

- Mr. Peter Ayoub of NAWC-A/D for his active participation in this project and his overall guidance and advice throughout this effort.

- Ms. Jennifer Swann of CFDRC for her careful preparation of all reports, presentation material and other documents for this project.

NOMENCLATURE

a_∞	Free-stream speed of sound.
d	Model reference length equivalent to the diameter of a circle with area equal to S.
CA	Axial-force coefficient, body axis system, positive downstream, FA/QS.
CN	Normal-force coefficient, body axis system, positive up, FN/QS.
CY	Side-force coefficient, body axis system, positive nose right, FY/QS.
CML looking	Rolling-moment coefficient, body axis system, positive clockwise upstream, ML/QSd.
CMM	Pitching-moment coefficient, body axis system, positive nose up, MM/QSd.
CMN	Yawing-moment coefficient, body axis system, positive nose right, MN/QSd.
CX	-CA
CZ	-CN
FA	Axial-force , body axis system, positive downstream.
FN	Normal-force, body axis system, positive up.
FX	-FA
FY	Side-force, body axis system, positive nose right.
FZ	-FN
Mach, M_∞	Free-Stream Mach Number, U_∞/a_∞.
ML upstream.	Rolling-moment, body axis system, positive clockwise looking
MM	Pitching-moment, body axis system, positive nose up.

NOMENCLATURE (continued)

MN	Yawing-moment, body axis system, positive nose right.
PSA	Static pressure, crewman abdomen.
PSC	Static pressure, crewman chest.
PSH	Static pressure, crewman head.
PSLL	Static pressure, crewman left leg.
PSLR	Static pressure, crewman right leg.
PSSBR	Static pressure, seat back reference.
Q	Free-Stream dynamic pressure.
Re_∞	Free-stream Reynolds number, $p_\infty V_\infty d/\mu_{.\infty}$.
S	Model reference area equivalent to the projected frontal area fo the seat and occupant.
α	Angle of attack, tan-1 w/u.
ß	Angle of sideslip, sin-1 v/V_∞.
V_∞	Free-stream velocity, m/s.
$\mu_{.\infty}$.	Free-stream viscosity, kg/ms.
p_∞	Free-stream density, kg/m^3.

TABLE OF CONTENTS

TABLE OF CONTENTS (continued)

TABLE OF CONTENTS (continued)

1. INTRODUCTION

1.1 Background

Aerodynamic characteristics of ejection seats and escape capsules have been closely studied by the U.S. Navy and Air Force research laboratories for many years. This research has been conducted to continually improve the performance of escape systems and to lesson the likelihood of pilot injury during ejection and separation from the aircraft. However, in spite of these studies and other significant advances in crew escape system technologies, statistics still show that crew injuries and fatalities are very common. The literature indicates that deficiencies in the area of aerodynamic stability is one of the major reasons for crew injuries.

Significant resources have been spent for many years on wind tunnel and ejection sled testing to improve the aerodynamic stability of the ejection seat and to assess various design concepts that will provide safe ejection during emergency conditions encountered throughout the performance envelope with speeds up to 700 Knots Equivalent Air Speed (KEAS). Wind tunnel tests have been used for static analysis to study various design concepts [1-6] while sled experiments have been used for dynamic testing to achieve the same goal. These methods have been reliable and led to tremendous improvements in the escape systems design process. However, these testing methods tend to be very expensive, time consuming and limit the number of concepts and conditions to be analyzed. Due to the expected nature of the ejection process, the trajectory and orientation of the seat, during and after separation from the aircraft, can be very unpredictable. Wind tunnel tests have shown that the loads on the pilot are highly dependent on the orientation of the seat and its proximity to the aircraft. Therefore during the seat analysis process, many seat orientations must be simulated and a data base of aerodynamic coefficients need to be developed for 6-DOF trajectory simulations, which is very expensive when using traditional experimental methods.

The U.S. Navy and Air Force have long been engaged in the development of mathematical models for escape system analysis. Various computer codes (ICARUS, GUESS, EASIEST, ACCESS) have been developed for predicting the escape system trajectory. However none of these or other codes is capable of providing full aerodynamic analysis of the seat/occupant, or seat/occupant and aircraft, and in turn provide aerodynamic coefficients for trajectory simulation and other seat design analysis.

This SBIR research and development effort seeks to develop and validate computational tools, using Computational Fluid Dynamics (CFD) techniques, for complete aerodynamic analysis of escape systems. The developed CFD tools provides flow information about the seat/occupant and seat/occupant and aircraft and their surroundings, which include pressure and Mach number profiles, velocity profiles, force and moments coefficients, etc. Such flow details can be very useful for:

- assessment of various design concepts especially those related to aerodynamic stability and drag reduction (e.g., stabilization devices, windblast protection devices, etc.),
- identification of areas of largest dynamic pressures and pressure gradients on the seat and occupant body during the ejection process,
- optimization of wind tunnel testing programs including assessment of wind tunnel wall and blockage (i.e., sting) interferences,
- analysis and assessment of seat and aircraft separation process including aircraft proximity effects on seat/occupant aerodynamics,
- assessment of various seat components such as Pitot tubes and static pressure sensors,
- providing 6-DOF codes with aerodynamic coefficients for seat/occupant trajectory simulations and analyses, and
- analyses of new generation ejection seat designs and other escape system components.

During the last two decades CFD methodology has seen significant advances in all of its disciplines, including grid generation, numerical algorithm development, parallelization, optimization and others. In the meantime, the tremendous improvement in the development of faster and cheaper computers made CFD more affordable. As a result, CFD has been very successfully used in the aerospace industry in similar fashion to this program.

1.2 Objectives of Phase I Study

The objectives of the Phase I study included:

- adaptation of an existing CFD code to conduct aerodynamic analysis for a generic ejection seat and occupant,
- validation of adapted methodology against experimental data,
- review existing drag reduction concepts and select several candidates for CFD analysis,
- document all findings in a final report.

1.3 Accomplishments of Phase I Study

All objectives of the Phase I study were successfully accomplished and the results were documented in a final report [7]. The major achievements of Phase I can be summarized as follow:

- Development of a 3D grid generation package to construct computational meshes for the seat/occupant geometry. With this grid generation package, the user can create a surface geometry and mesh for the seat/occupant and create a computational domain for the seat/occupant and smooth it using an elliptic partial differential equation solver.

- Adaptation of a selected CFD code, REFLEQS, for external aerodynamics analysis of seat/occupant configuration.

- Development of a force and moment integration module and implementation into REFLEQS code.

- Performing several demonstration and validation calculations including:
  - 2D seat alone demonstration calculations,
  - 2D seat/occupant demonstration calculations,
  - 3D seat/alone demonstration calculations,
  - 3D SIII-3ER seat demonstration calculations
  - 3D half scale F-106 limited validation calculations

- Performing a design concept review and assessment. Existing literature on escape systems was reviewed and several design concepts were selected for CFD analysis under Phase II.

The Phase I work clearly demonstrated the feasibility of the approach and built a strong foundation for further model development and validation under the Phase II program.

1.4 Objectives of Phase II Study

The overall objective of the Phase II program was to complete the development and adaptation of the grid generation program and the CFD code. More emphasis in Phase II was placed on adopting a more automated and advanced method for creating surface geometry and surface mesh for the seat and occupant. Also under Phase II, the capabilities of the CFD code were to be expanded to perform unsteady flow simulations on the ejection seat and occupant. All the developed and adapted tools must be validated against wind tunnel test data.

Another major objective of Phase II was the selection and development of a CFD methodology to conduct steady state and unsteady simulations for seat/occupant separation from an aircraft (Phase II extension).

Specific objectives of Phase II can be summarized as follow:

- completion and customization of ejection seat grid generation package,

- selection and utilization of a CAD/grid generation program for seat/occupant surface geometry definition and surface mesh creation,

- implementation of an advanced time-accurate shock capturing scheme for transient simulations,

- investigation and assessment of turbulence modeling,

- demonstration and validation of CFD code for seat/occupant analysis,
- assessment and analysis of selected design concepts,
- assessment and selection of a CFD methodology for seat/occupant and aircraft simulations both in steady fixed and unsteady moving modes,
- validation of selected and/or developed seat and aircraft methodology against steady state captive wind tunnel test data,
- demonstration of selected and/or developed seat and aircraft methodology for unsteady seat separation from an aircraft using prescribed trajectory,
- delivery of developed tools to the Navy including complete documentation and user training and support.

1.5 Accomplishments of Phase II Study

All of the objectives of this Phase II study were successfully accomplished as this final report documents, as well as the quarterly progress reports [7] and several publications [8,9,10,11] demonstrated. A CAD geometry modeling/grid generation procedure and several packages, including an elliptic grid generator and CAD geometry/grid generation code, CFD-GEOM, were developed and adapted for this project. Also two CFD-codes, CFD-ACE and CFD-FASTRAN, were adapted and validated for aerodynamic analysis of seat/occupant and seat/occupant and aircraft analysis. All the CFD tools were validated against test data and successfully demonstrated for escape systems applications.

The Accomplishments of this Phase II effort can be summarized as follow:

- A CAD geometry and grid generation package, called CFD-GEOM, was adapted and partially developed under this project for geometry modeling and algebraic grid generation for escape system configurations including ejection seat/ occupant and aircraft.
- A Partial Differential Equation program was developed for elliptic grid generation of seat and occupant grids. This program smooths seat/occupant grids with automatic clustering and orthogonality control on outside boundaries as well as seat/occupant surfaces.
- The CFD-ACE code was adapted for seat and occupant aerodynamic analysis. A numerical and turbulence modeling assessment study was conducted with CFD-ACE for blunt body flows. Two high order differencing schemes, second_order upwind and Osher Chakravarthy, were implemented into CFD-ACE for escape system applications. The results of the assessment study was the development of several guidelines for ejection seat and occupant flow analysis.
- A technology assessment and code selection study was conducted to select and/ or develop the most suitable CFD methodology for seat/aircraft analysis. Three

CFD codes were assessed and CFD FASTRAN was selected as the baseline for the seat and aircraft analysis.

- The CFD-FASTRAN code was adapted for seat and aircraft analysis for both steady-state and unsteady seat and aircraft separation. Two new multiple and moving bodies methodologies were developed and implemented into the code. The Chimera overset gridding technique was implemented and adopted for seat and aircraft separation. The Chimera technique features new hole cutting and tree searching features that resolved most of the inefficiency problems with traditional chimera techniques.
- Several geometry models and computational grids were developed for escape systems. These include NACES seat and occupant, ACES-II seat and occupant, F-16 aircraft and cockpit, F-18 aircraft and cockpit and B-1A escape capsule. Several versions of these grids were created for single and multiple bodies analysis.
- CFD-ACE was extensively validated and demonstrated against simple benchmark problems including cylinder, half cylinder and sphere problems. These validation and demonstration calculations proved the prediction accuracy, robustness and efficiency of the code for handling blunt body flow problems. Based on these calculations several guidelines were developed for the analysis of seat/occupant configurations.
- CFD-ACE was extensively demonstrated and validated against several escape system configurations including the NACES seat and occupant, the ACES-II seat and occupant and the B-1A escape capsule. These calculations showed the correct and predictable flow trends and compared very well to wind tunnel test data where available.
- CFD-FASTRAN was demonstrated and validated for seat/occupant and seat/occupant and aircraft analysis. Validations were performed using an ACES-II and F-16 wind tunnel configuration. Predictions compared favorably to wind tunnel test data. Also a demonstration calculation was performed with CFD-FASTRAN for the ACES-II separation from the F-16 aircraft using a prescribed trajectory. The demonstration calculations showed the correct flow trends and compared well to steady state predictions.

This Phase I and Phase II studies resulted in the development and adaptations of several CFD tools and methodologies for escape systems aerodynamic analysis. The CFD tools have been extensively demonstrated and validated against test data for several escape system configurations. These tools have been used in several Phase III efforts for escape system design and qualification studies. Most of the tools have already been delivered to the Navy and are being used by Navy engineers for ejection seat and occupant analysis.

1.6 Outline of Remainder of This Report

The remainder of this report will present the following:

a. discussion of computational methodologies and codes adaptations for seat and occupant analysis (Volume 1),

b. presentation of demonstration and validation results for seat/occupant analysis on simple benchmark geometries (Volume 1),

c. presentation and discussion of code demonstration validations on escape system configurations, (Volume 1)

d. presentation and discussions of seat/occupant unsteady demonstration calculations (Volume 1),

e. discussion of methodology selection and development for seat/aircraft analysis (Volume 2),

f. discussion of CFD-FASTRAN code development and adaptation for multiple and moving bodies problems (Volume 2),

g. presentation and discussion of seat/aircraft steady-state and unsteady simulations (Volume 2),

h. conclusions from Phase I and Phase II studies, commercialization status and outlook for Phase III (Volume 2).

2. COMPUTATIONAL METHODOLOGY DEVELOPMENT AND ADAPTATION FOR SEAT AND OCCUPANT ANALYSIS

This section describes the development, adaptation and application of the various tools and methodologies, to the seat and occupant flow analysis. Geometry modeling and grid generation processes are discussed first followed by the flow solver, CFD-ACE, discussions.

2.1 Geometry Modeling

Due to the complexity of the seat and occupant geometry, from a CFD modeling standpoint, this task was regarded as one of the most crucial to the overall success of this study. During Phase I, simple analytical and mathematical functions were used to define the surface of the seat and occupant. The geometry data was extracted from drawings. The seat and occupant geometry was subdivided into several planes and several points were identified on each plane. These points were connected to form each plane, and then all the planes were put together to form the surface of the seat and occupant. The resultant surface mesh from this procedure is shown in Figures 2-1 and 2-2. This method worked very well as 3D geometry of the seat and occupant were created and analyzed without CAD tools, however, it was inefficient (time consuming) and did not necessarily preserve the integrity of the geometry.

The plan for Phase II was to adapt a Mechanical Computer Aided Design (MCAD) methodology for the geometry modeling and surface mesh creation.

2.1.1 Geometry Modeling Tools

One of the major tasks of this phase II program was to identify and select a CAD package for the geometry modeling and surface mesh definition of the ejection seat and occupant. Another task was to develop a procedure for geometry modeling and grid generation that preserves the integrity of the geometry and can be performed and updated effectively. Several efforts were spent under this task to identify and select a CAD tool for this purpose. At that time, CFDRC was in the process of planning the development of a new geometry modeling and grid generation package. However, due to the expected length of the development process (more than one year), it was decided to adopt a commercially available package for this effort. After reviewing several packages, ICEM-CFD was selected as the CAD tool for this initial effort. Section 2.1.3 below describes the geometry modeling procedure with ICEM.

During the development of CFDRC's new geometry modeling and grid generation package, ultimately named CFD-GEOM, attention was focused on the ejection seat and occupant geometry and its requirements. It was made sure during this development process that CFD-GEOM will be capable of easily, and in a more automated manner, handle the seat/occupant geometry and their interface with the aircraft. During the development process, the seat/occupant geometry was used as one of the main tests for the newly developed CFD-GEOM functions. An overview of CFD-GEOM is given below.

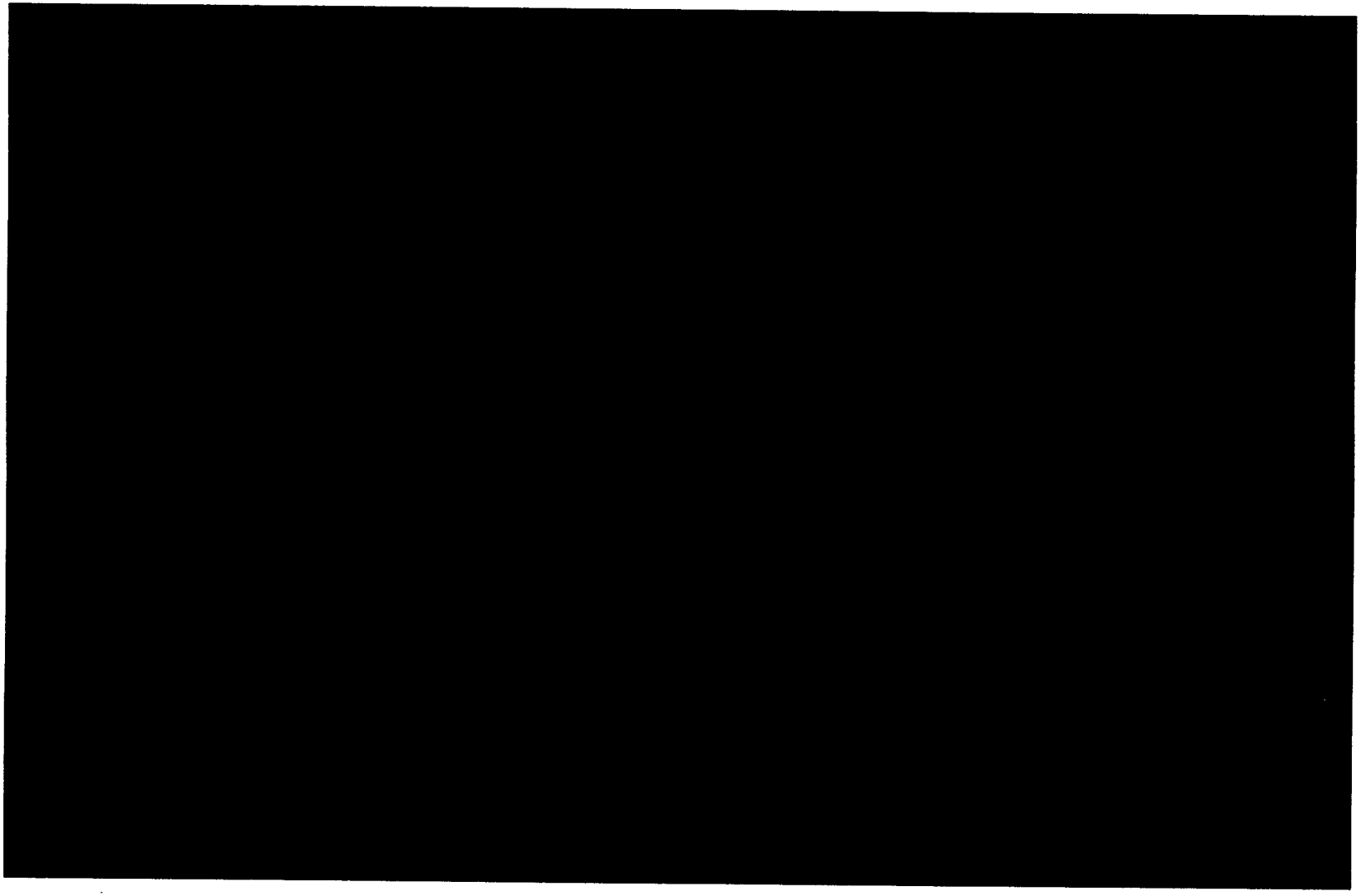

Figure 2-1. Surface Mesh of the Phase I NACES Seat Grid Model

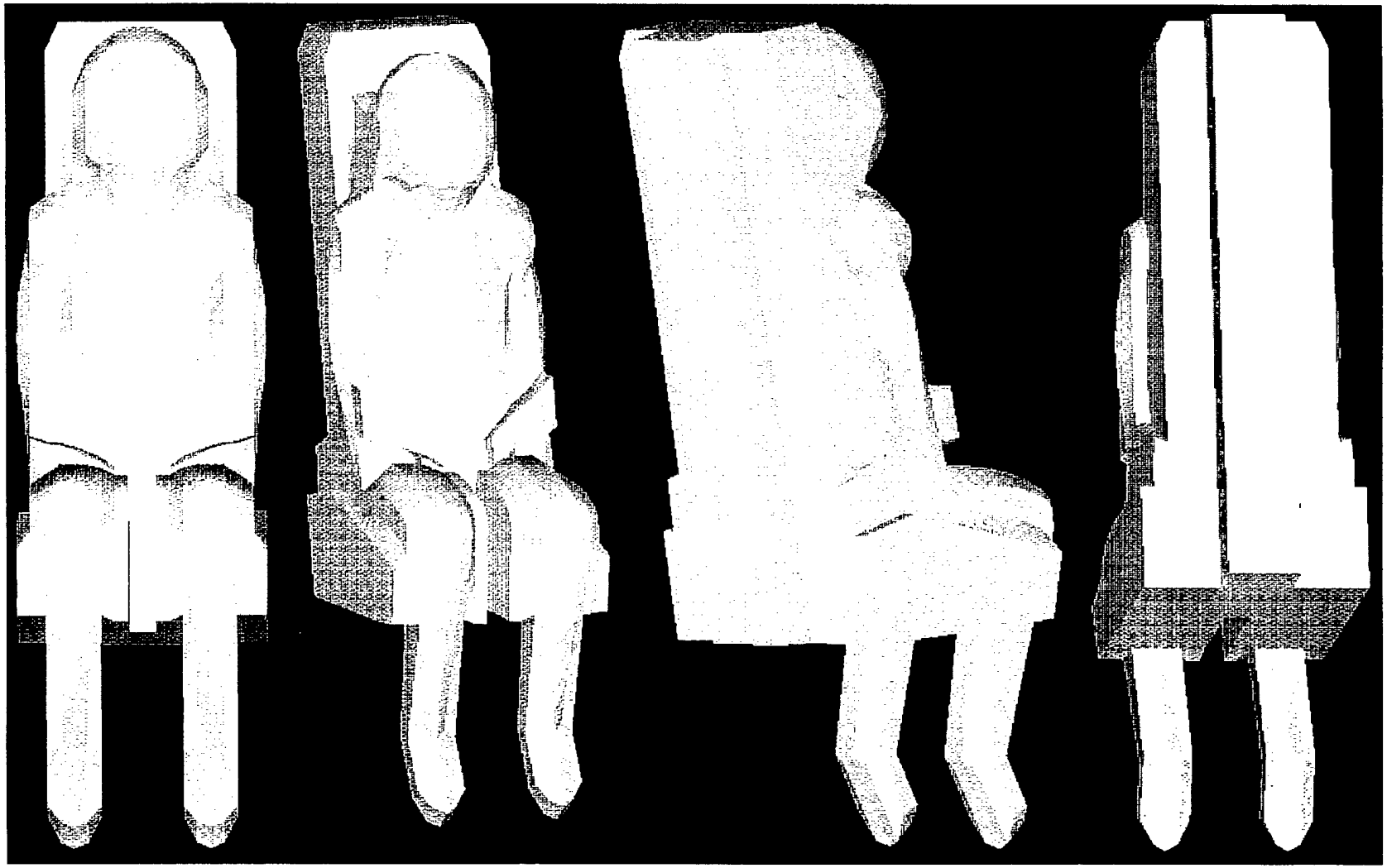

Figure 2-2. Shaded Surface of the Phase I NACES Seat Geometry and Grid Model

Therefore, in summary, the original geometry and surface mesh for NACES ejection seat and occupant were created with ICEM-CFD. After the first internal release of CFD-GEOM, the ICEM-CFD model was ported into CFD-GEOM through the IGES format utility of both codes. Since that time, CFD-GEOM has been used for geometry modeling and surface mesh generation efforts under this contract and will be delivered to the Navy with this report.

2.1.2 Overview of CFD-GEOM

As mentioned above, the escape system applications (seat/occupant, aircraft, aircraft cockpit, canopy, escape capsule, etc) in general and the seat/occupant in specific, played a major role in the development of CFD-GEOM (from the capabilities and specification requirements standpoint). CFD-GEOM has all the capabilities inherent in ICEM-CFD and used for ejection seat modeling. However, the big advantage with CFD-GEOM, is the ease-of-use, speed and efficiency especially for the surface grid generation process. CFD-GEOM development continued through the last 3 years (1993-1996) and is now a commercially available code. CFD-GEOM is marketed as a stand-alone product and also as part of a complete CFD solutions package with CFD-ACE and CFD-VIEW.

The salient features and capabilities of CFD-GEOM include:

- intuitive graphical user interface;
- complete integration between geometry and grid generation modules, therefore facilitating automatic and instantaneous updating of all relevant data structures;
- extensive geometry and grid editing capabilities with instantaneous updating of entire model;
- virtual parts libraries for geometry and grid models;
- complete integration with CFDRC's software including the assigning of boundary conditions; and
- support interfacing with other CAD system through the IGES data format.

Geometric modeling capabilities of CFD-GEOM, as of the writing of this report, include:

- full implementation of three-dimensional geometries including points, lines, arcs, circles, point interpolating curves and splines and surfaces;
- wire frame and surface modeling supported using transfinite interpolants;
- grid generation may be performed directly on NURBS surfaces;
- splitting geometry capabilities at any arbitrary point;
- extruding a geometry along a vector;
- performing a curve-curve and surface-surface intersection; and
- translating, rotating and scaling geometries.

CFD-GEOM supports both structured and unstructured grid generation. Structured grid generation is based on the transfinite interpolation (TFI) methodology. The model supports uniform, exponential and hyperbolic tangent grid point distribution along edges. The grid generation on NURBS curves is done directly on the piecewise linear discretization of the NURBS curve and can be performed to any arbitrary user-specified

precision. grid generation on NURBS surfaces is completed by projecting an approximate TFI grid directly onto the NURBS mathematical representation of the surface.

CFD-GEOM supports a bottom-up approach in labeling geometry elements as edges, faces and blocks. In the structured grid generation, the edge is the basic element for both surface and volume grid generation. An edge can be comprised of one or many lines and curves. Four user specified edges make a face and six user specified faces make a block (or one volume). The face grid is created from the edge grids using TFI. The volume grid is created from edges and faces also using TFI. Several blocks can composite into a single block

CFD-GEOM also support 2D and 3D unstructured grid generation. For more details on the capabilities of CFD-GEOM refer to the CFD-GEOM user manual which will be provided with this report. For complete reference, a brochure of CFD-GEOM is included in Appendix B.

2.1.3 Geometry Modeling Procedure for NACES

Both the NACES and ACES-II seats and occupant geometry and grid models were created under this project. The process used for the geometry modeling and grid generation procedure is similar. For the sake of brevity, only the NACES seat and occupant geometry will be discussed here. Complete description of this process was presented in the second and third quarterly progress reports (references).

The original geometry and grid model of the NACES seat were created with ICEM-CFD. ICEM has two main modules; ICEM-DDN, which is a geometry CAD module, and MULCAD, which is a CFD mesh generation module.

The overall process of creating the geometry model for NACES involved the following steps:

- creating a wire frame diagram of the seat and occupant which conform to a structured single domain;
- subdividing the wire frame diagram of the seat and occupant into logical domain units to fix the surface mesh;
- creating the outer portion of the fluid domain which encloses a rectangle in space comprising the many smaller domains that define the seat surface and fluid domain;
- setting the boundary conditions to block flow on the domains that are inside the seat and occupant;
- setting the boundary conditions on the outer surfaces describing the flow field; and
- combining all of the smaller domains into one large domain keeping intact the boundary conditions previously set.

The major areas of work in the above six steps are the first 3. The majority of work in

creating a grid is to adequately create a wire frame diagram that has the following properties:

a. conforms to the actual seat and occupant geometry;
b. has a structure grid topology; and
c. has limited grid skewness.

The availability of the CAD file provided by NAWC-A/D, allowed a very accurate wire frame representation of the seat and occupant to be created. Many of the original lines were used to represent the seat alone while a complete creation of the wire frame diagram was necessary for the occupant since he was represented by surfaces in the original CAD file. In creating the wire frame of the occupant minor modifications to the original surface were made to exclude small gaps and sharp edges and to allow for a suitable grid with minimum skewness. A suitable blending between the occupant and seat was also created to prevent grid skewness. Figure 2-3 shows the original CAD representation provided by the Navy while Figure 2-4 shows the wireframe diagram created by the CAD model for CFD simulations.

Shaded and surface mesh representations of the new seat and occupant (only half of the seat and occupant are shown since the seat is symmetric) are given from several angles using CFDRC's package CFD-VIEW in Figure 2.5 and 2.6 The shaded surface of the mesh used in Phase I was shown in Figure 2-1. Several differences between the new and old meshes are immediately visible. Among the major differences are the treatment of the arm and shoulder and the treatment of the seat behind the occupant. The new surface mesh obtained directly from the CAD file better represents the actual seat and occupant geometry as shown in the figures.

One of the other major advantages to using the CAD package is the grid points may be easily added in any direction to refine the grid. The old surface generation method required a significant amount of new work to increase nodes on the seat and occupant surface along side surface planes. Since a grid sensitivity study is necessary for any CFD calculations generating grids quickly is very important.

2.2 Grid Generation

The grid generation procedure for the ejection seat and occupant consist of the following steps:

- create surface mesh for seat and occupant.
- define the computational domain and mesh the outside surfaces.
- create a 3D computational mesh that surrounds the seat and occupant geometry.

The volume grid that surrounds the occupant is created first using the CAD algebraic gridding capability. The grid is then smoothed and clustered using an elliptic grid generator, CFD-GRID, that was developed under this project.

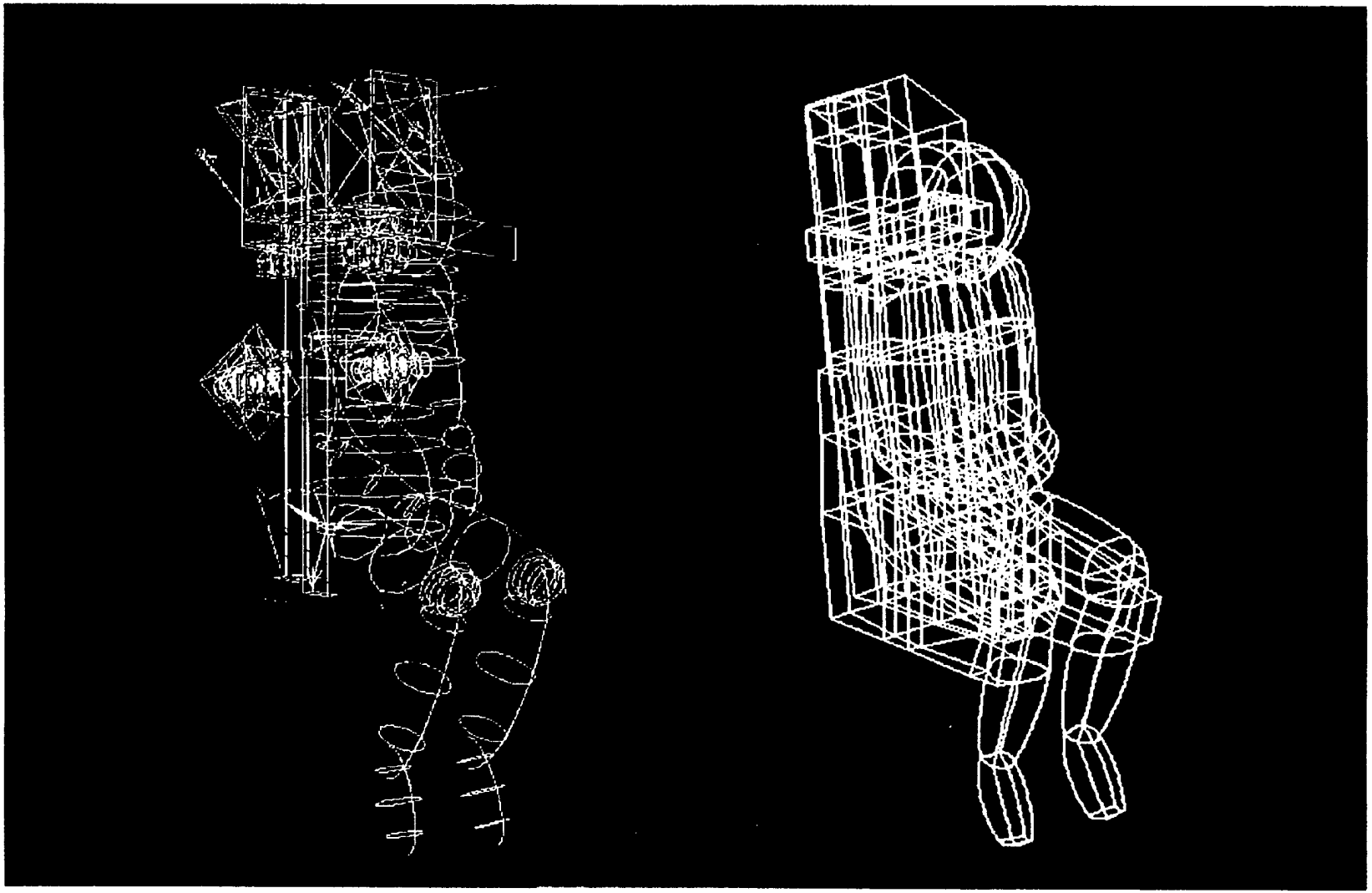

Figure 2-3. Original CAD Description of the NACES Seat

Figure 2-4. Wireframe Diagram of the CAD Model

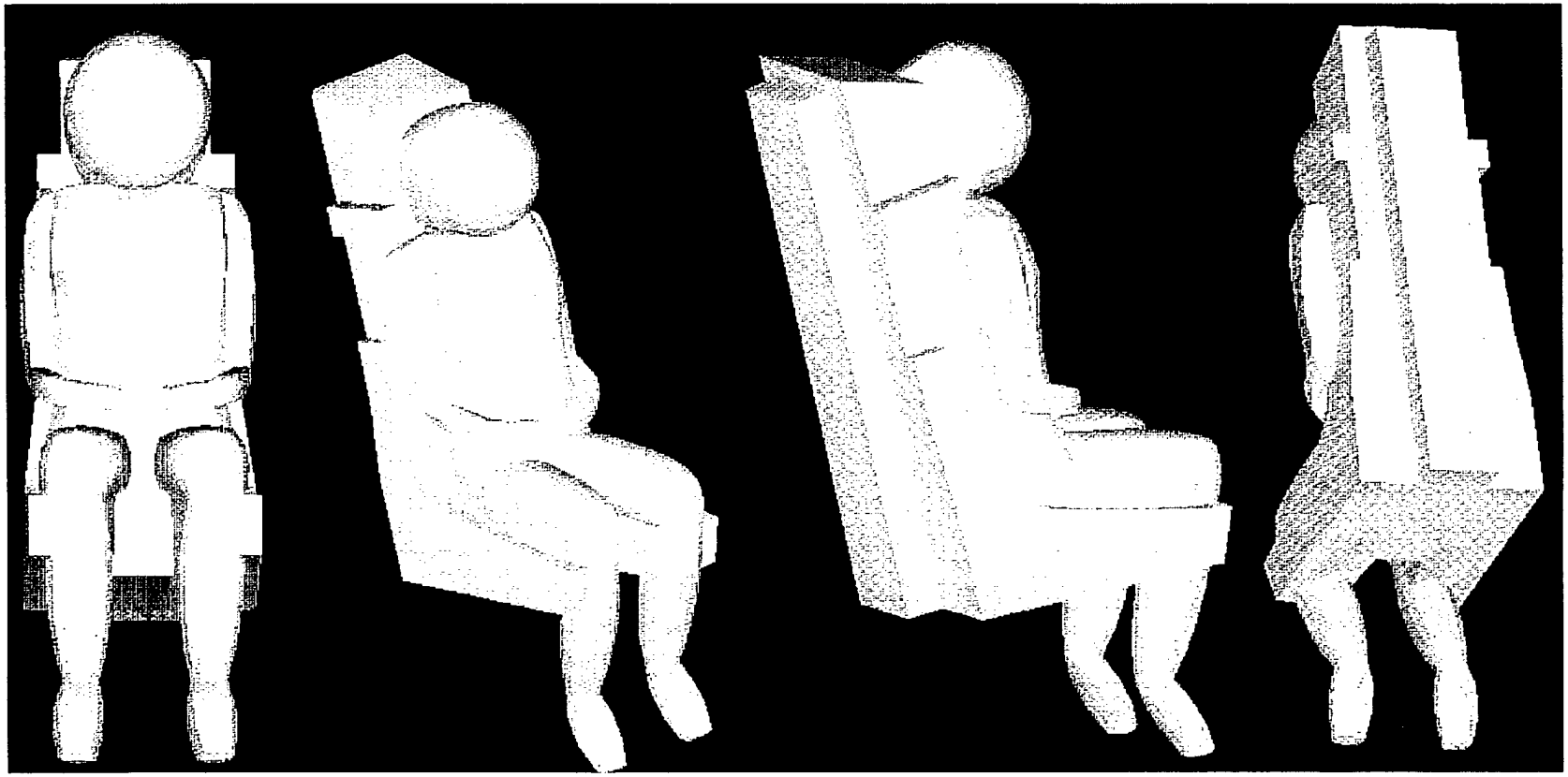

Figure 2-5. Shaded Surface Mesh of the CAD Generated NACES Seat

Figure 2-6. Surface Mesh of the CAD Generated NACES Seat

2.2.1 Grid Generation Procedure

The steps involved in the algebraic grid generation process for the ejection seat and occupant may be summarized as follow:

- obtain a surface mesh for the seat and occupant as described above in Section 2.1.3.
- create a box around the seat and occupant. This 3D box represent the extent of the computational domain.
- grid all the wireframes of the box using desirable grid distributions. Using the wire frame grid, mesh all the surfaces using transfinite interpolation methods.
- mesh the inside of the 3D computational domain (inside of the box), using transfinite interpolation techniques. The surface mesh of the box and seat/ occupant are used for interpolation. The box is subdivided into several domains that surround the seat and occupant. Each domain is filled separately using the surface of the box and seat/occupant.
- dump a PLOT3D formatted grid file that has the CAD created grid.
- read the PLOT3D formatted grid file into the elliptic grid generator and elliptically smooth the baseline (alfa=0, beta=0) orientation grid (by solving Poisson equations) and cluster the grid near the seat/occupant surfaces. The following user requirements are made in the elliptic grid generation process:

    - fix (do not solve for) cells representing the seat and occupant.
    - enforce orthogonality on all outside boundaries.
    - enforce orthogonality on all seat/occupant surfaces.
    - cluster the grid to the seat/occupant surface according to the specified control parameters.

- other seat/occupant orientation can be achieved using the orientation adjustment module described below.

An overview of the elliptic grid generator is given below.

2.2.2 Elliptic Grid Generation

A three-dimensional elliptic grid generation package, called CFD-GRID, was developed in Phase I of this project to smooth and control grid distribution around the complex seat and occupant geometry. In this package, the partial differential equations are solved for the coordinate directions (x,y and z) in Body-Fitted Coordinate (BFC) systems with distortion functions to control grid spacing, attraction and orthogonality. The enhancements made to the elliptic grid generator in Phase II include:

- orthogonal attraction on internal surfaces (seat/occupant surface).
- seat/occupant attitude control (adjust the baseline grid for any yaw and pitch orientation).

The orthogonal attraction functions were implemented, under Phase II, to smooth and attract the grid to the blocked surface (in this case the seat/occupant surfaces). The

internal grid orthogonal functions enforce grid lines normal to a line or surface with a distance (DS) away from that surface. The prescribed distance (DS) can be either specified by the user or can be set implicitly during the calculations. Figures 2-7 and 2-8 show several cross sections of the NACES seat where orthogonal attraction is evident on the seat/occupant surface. Note that for the previous mesh obtained without orthogonal attraction, several adjustments were made to the grid near the surface (chest and legs) to obtain a near orthogonal grid at the surface. However, using the new functions, orthogonality can be achieved automatically without user adjustments. Several modifications were also made to the code to automatically recognize blocked surfaces (a file available from a CFD-GEOM or CFD-ACE that includes blockage information). The elliptic computational grid, with clustering and orthogonality control, at the symmetry plane is shown in Figure 2-9.

The attitude control model algebraically adjusts the baseline elliptic grid for any pitch and yaw configurations. The advantage of this procedure is in its efficiency. While solving a typical seat/occupant grid may take an hour (or several minutes), this routine adjust the grid in few seconds. This procedure works as follow:

- fixing a box of computational cells around the seat and occupant.
- rotate all the grid nodes within the box by the desired alfa and beta angles,
- using a spring analogy method adjust all the grid nodes in the computational domain according the specified angles (the grid nodes closest to the box are rotated almost by the full angle, the rotation angle decreases as the distance gets farther from the box).

Figure 2-10 and 2-11 show the computational grid for several pitch and yaw orientations where the baseline grid was adjusted using the attitude control module.

Complete description of the methodology and the functionality of the grid generator is available in Phase I final report and in a technical paper entitled "A Partial Differential Equation Method for Three Dimensional Grid Generation" provided in Appendix A.

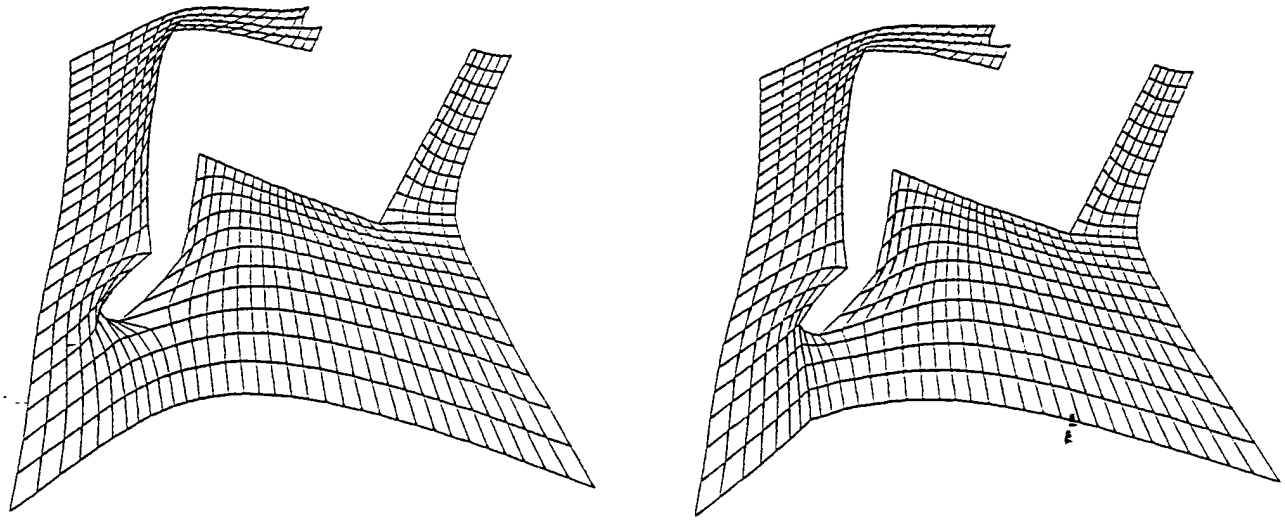

without internal orthogonality

with internal orthogonality

Figure 2-7. Grid Improvements Using Internal Orthogonality on Lower Portion of Seat/Occupant

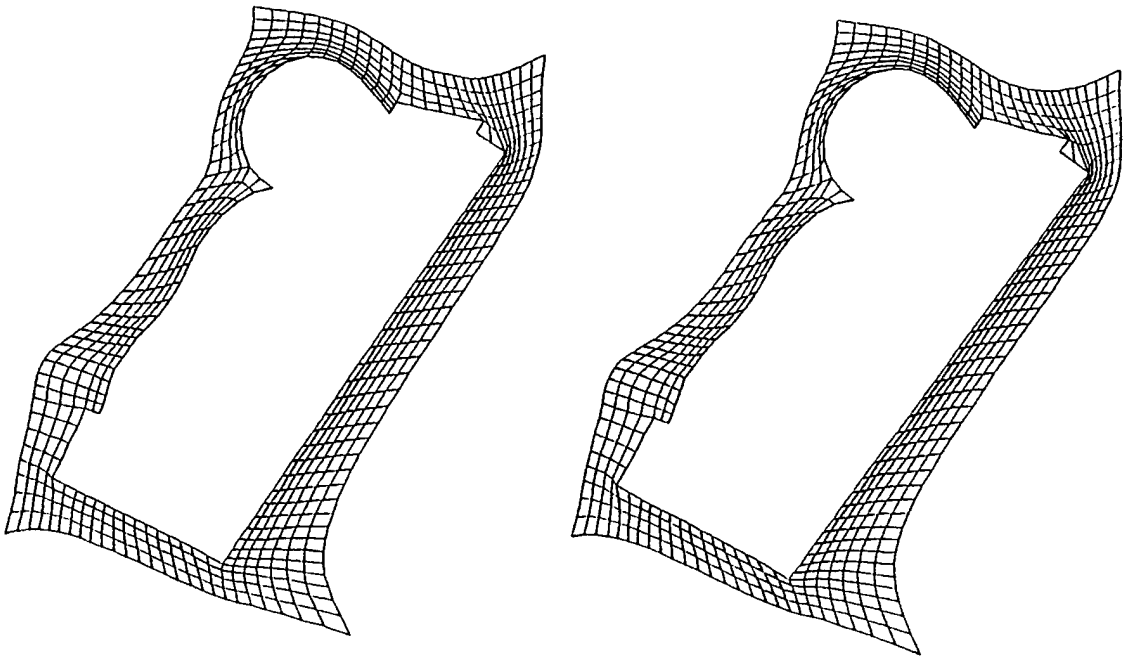

with orthogonality

without orthogonality

Figure 2-8. Grid Improvement Using Internal Orthogonality on Upper Portion of Seat/Occupant

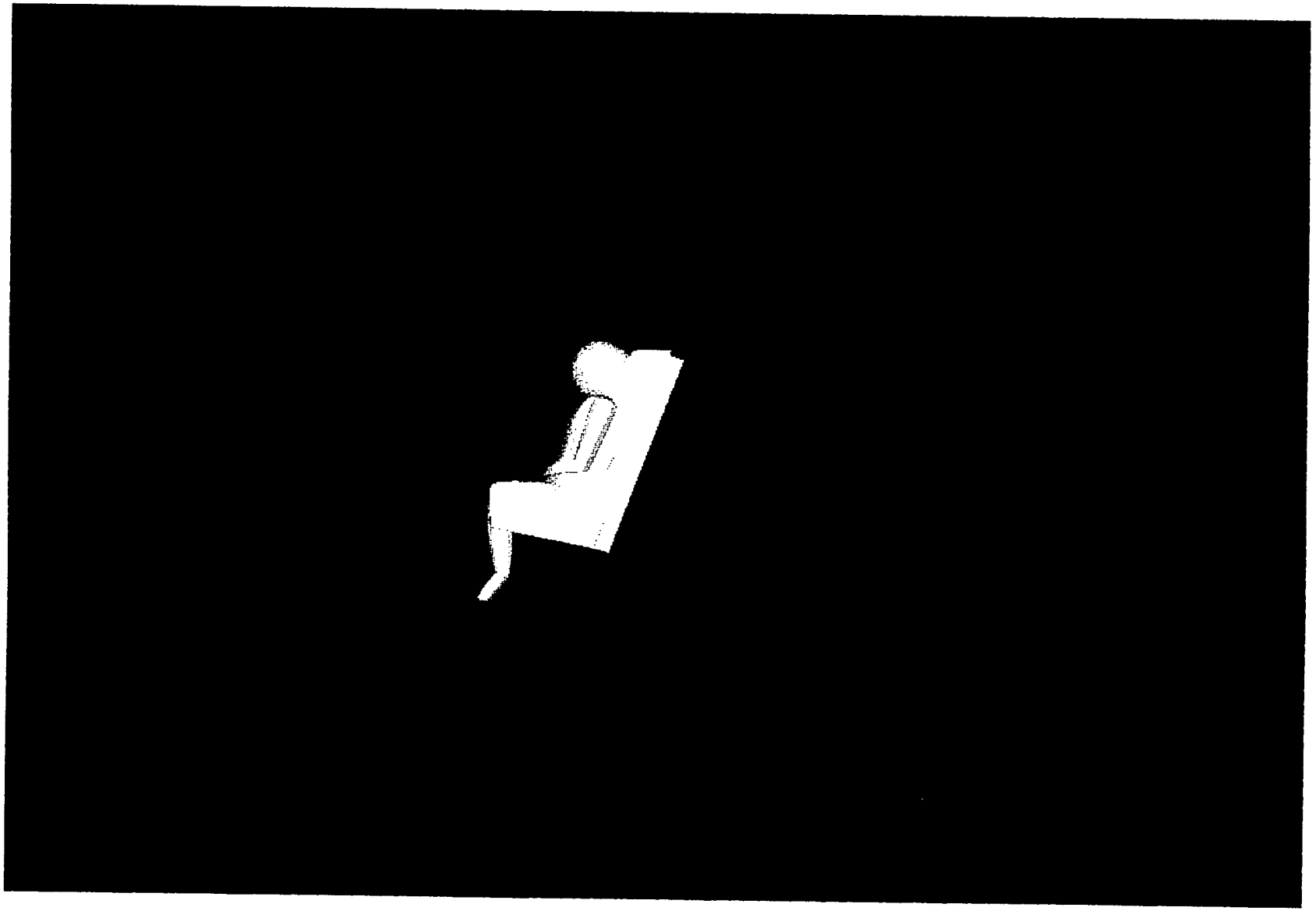

Figure 2-9. Computational Longitudinal Symmetry Plane from the Baseline Elliptic Grid

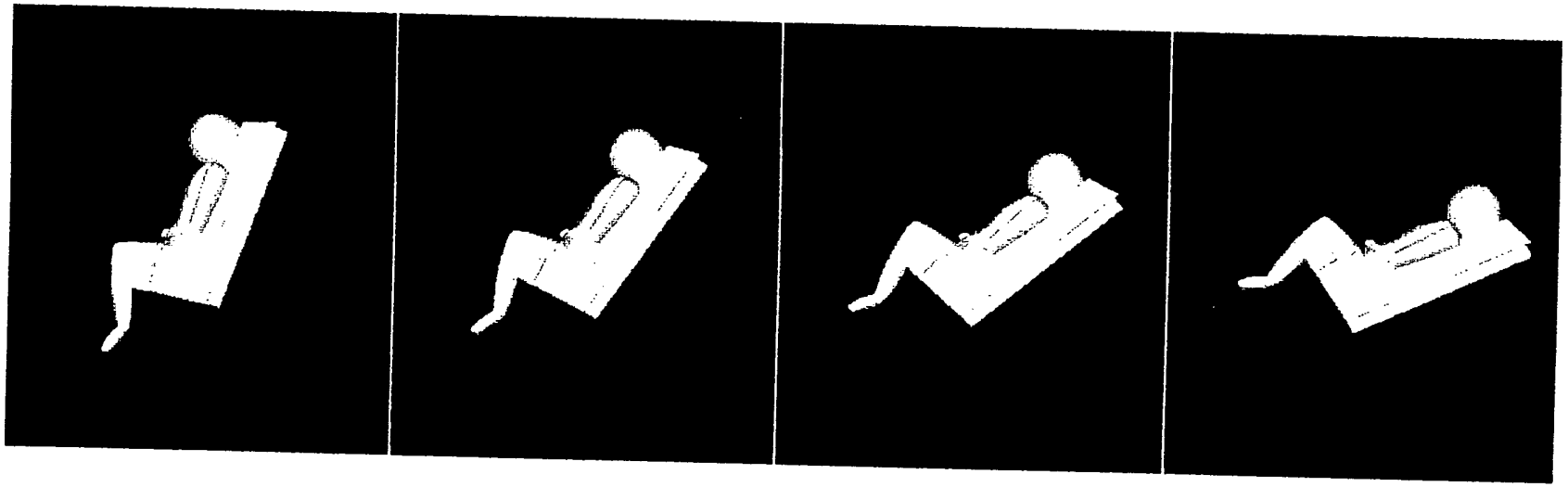

Figure 2-10. Elliptic Computational Mesh Adjusted for Different Pitch Orientations; α = 0, 15, 30 and 45 degrees

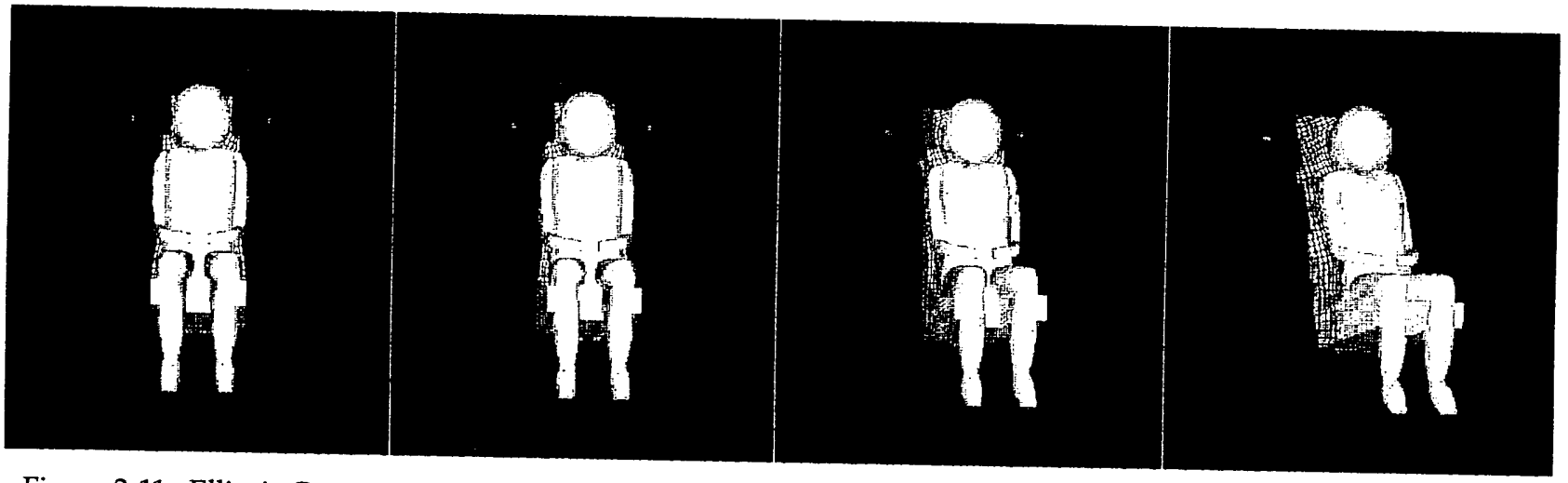

Figure 2-11. Elliptic Computational Mesh Adjusted for Different Yaw Orientations; β = 0, 5, 15, and 30 degrees

2.3 CFD-ACE Flow Solver Adaptations

In the Phase I project of this effort, RFELEQS-3D was the selected code for the seat/occupant flow simulations. REFLEQS-3D utilized a pressure-based approach for solving the full Navier-Stokes equations in curvilinear coordinate systems using co-located grid arrangement. The REFLEQS-3D code was a research code developed at CFDRC partially by SBIR funds. At the beginning of the Phase II project REFLEQS-3D was going through an extensive effort to commercialize the code. The name of the new commercial code is CFD-ACE. CFD-ACE uses basically the same methodologies as the REFLEQS-3D code. However, CFD-ACE has been made a more user friendly code by developing a Graphic User Interface (GUI), and more robust after going through an extensive testing and validation effort. **CFD-ACE** has been used for all the seat/occupant simulations conducted under this project.

As in the case of CFD-GEOM development, CFD-ACE development was greatly influenced by the ejection seat applications. Several efforts that took place under this project were directly related to the code enhancement and development efforts. Specifically, the following efforts were performed under this project:

- turbulence modeling assessment for blunt bodies applications;
- differencing schemes assessment and adaptation for accurate drag and lift prediction and shock capturing;
- force and moment integrator module development.

An overview of the CFD-ACE code is given below, followed by a description of the adaptations made for ejection seat applications.

2.3.1 CFD-ACE Overview

CFD-ACE is a commercial CFD software that has been developed by CFDRC. CFD-ACE was partially developed by SBIR funds (including this contract). The development of CFD-ACE has been greatly influenced by its application to escape systems analysis. The basic capabilities of the code have been validated against several benchmark problems [10]. The code features that are relevant to seat/occupant analysis have been validated under this contract as described in section 3 of this report. The CFD-ACE code has been extensively used and validated for ejection seat applications [9-12, 14-16].

The salient features, relevant to this work, of CFD-ACE include:

- fully conservative finite volume solution of the full Navier-Stokes equations [17];
- multi-block structured grid with many-to-one interface capability for local grid refinement;
- steady and unsteady solutions;
- inviscid, laminar and turbulent flow solutions;
- compressible and incompressible flows;
- extensive combustion/chemical reaction models using multi-step, finite rate chemistry with stiff kinetics;

- several turbulence models including k-epsilon, Baldwin-Lomax and RNG models;
- several differencing schemes including second order upwind, Osher-Chakravarthy and central differencing;
- variable properties and JANAAF standard thermodynamics tables;
- advanced X/Motif GUI interface;
- documentation including theory, user and validation manuals.

CFD-ACE has several other capabilities that are not related to this project. For complete reference, check the CFD-ACE documentation manuals delivered with this report and CFD-ACE brochure included in Appendix B.

2.3.2 Numerical Schemes Assessment for Blunt Body Flows

In the Phase I project, all calculations were made with a first order upwind differencing scheme. The first order scheme is known to be very dissipative and does not produce crisp shocks. First order upwind also have the tendency to under-predict drag. Since the flow regimes encountered in ejection seat applications, involve transonic and low supersonic regimes with expected bow and reflected shocks, it was determined in Phase I that a more advanced higher order scheme will be needed for ejection seat application. As mentioned above, the higher order scheme is also expected to produce better force and moment coefficients.

As part of this effort, higher order differencing schemes were incorporated into CFD-ACE and tested for this application. The high order schemes include Central (was already available in CFD-ACE but not tested for blunt body applications), second-order upwind and Osher-Chakravarthy schemes. These three schemes were implemented and tested on ejection seat flows for various flow regimes. The intent here was to choose the most accurate and efficient scheme for a specified flow regime. Efficiency plays a major role in this assessment due to the fact that higher order schemes tend to be very numerically unstable, especially when recirculation zones and wakes are encountered (as is the case with ejection seat flows). Several numerical experiments were conducted after these schemes were implemented on simple flow problems as well as ejection seat problems. Some details about these experiments are presented in Section 3.

The numerical experiments to assess differencing schemes for ejection seat applications resulted in the following conclusions:

- first-order upwind scheme results in about 10 percent discrepancy in the aerodynamic coefficient predictions as compared to higher order schemes (which predict better comparisons to wind tunnel test data [14].
- Osher-Chakravarthy scheme is most stable numerically for supersonic flows. Second-order upwind and Central schemes result in very oscillatory convergence characteristics in this flow regime.
- Second-order upwind scheme is the most numerically stable for subsonic and transonic flows. Central scheme is again unstable and results in very slow convergence (it is typical of Central scheme to be unstable for recirculating flows).

- for simpler shape geometries, such as a cylinder, central scheme produced good results and possessed good convergence characteristics.

Based on the above conclusions, is was determined, for best accuracy and efficiency, to use the **Osher-Chakravarthy scheme for supersonic flows** and the **second-order upwind scheme for subsonic and transonic flows,** for ejection seat and occupant applications.

Figure 2-12 shows the Mach number contours in front of the ejection seat and occupant at free stream Mach number of 2.0 using both the first-order upwind scheme and the Osher-Chakravarthy scheme. The shock wave produced by the Osher scheme is much crisper. The better resolution of this shock, coupled with the fact that Osher is much less dissipative (compared to first-order upwind), is expected to result in much better prediction of force and moment coefficients. Figure 2-13 shows the Mach number contours in the computational plane of the Pitot tubes for both schemes. Notice that at the symmetry boundary conditions (at the top and bottom) a weak reflected shock is produced with the Osher scheme. This shows the better accuracy of Osher, since theoretically a reflected shock is supposed to be produced at a symmetry boundary. A grid sensitivity study showed however that this reflected shock does not affect the force and moment predictions (the boundary was placed far enough to minimize this effect).

The recommendations made above were used in a parallel study for the NACES seat [14]. This study repeatedly showed the better predictions of the Osher and second-order upwind schemes in the regimes cited above. The numerical schemes recommendations were also extensively used for a validation study under this project. The findings of this study are extensively documented in the fifth quarterly progress report [8] and a technical paper entitled "Validation of CFD Methodology for Ejection Seat Application". For complete reference a copy this paper is included in Appendix A of this report.

2.3.3 Turbulence Modeling Assessment for Blunt Body Flows

Turbulence modeling is critical for high Reynolds number flows with separation, recirculation zones and wakes. This area of fluid dynamics research, however, has not yet matured. These type of flows still present tremendous challenges to the engineering community. The only and most accurate way to predict turbulence for these type of flows is to use Large Eddy Simulations (LES) methodology. This methodology, however, is very expensive and is not affordable for this type of analysis. LES requires prohibitively large number of grid points for the seat and occupant that may not be affordable from the perspective of this effort. The objective of this effort is to find the most feasible and efficient methodology to reasonably accurately (within 10-15 percent) predict ejection seat and occupant aerodynamic characteristics. Due to the large geometry uncertainties (ejection seat geometry modifications for reasonable CFD modeling and occupant size, shape and clothing uncertainties) and flow condition uncertainties (aircraft and rocket plume effects), it becomes economically unjustified to use such large grids to yield few percentage points of accuracy (typically 1-5 percent).

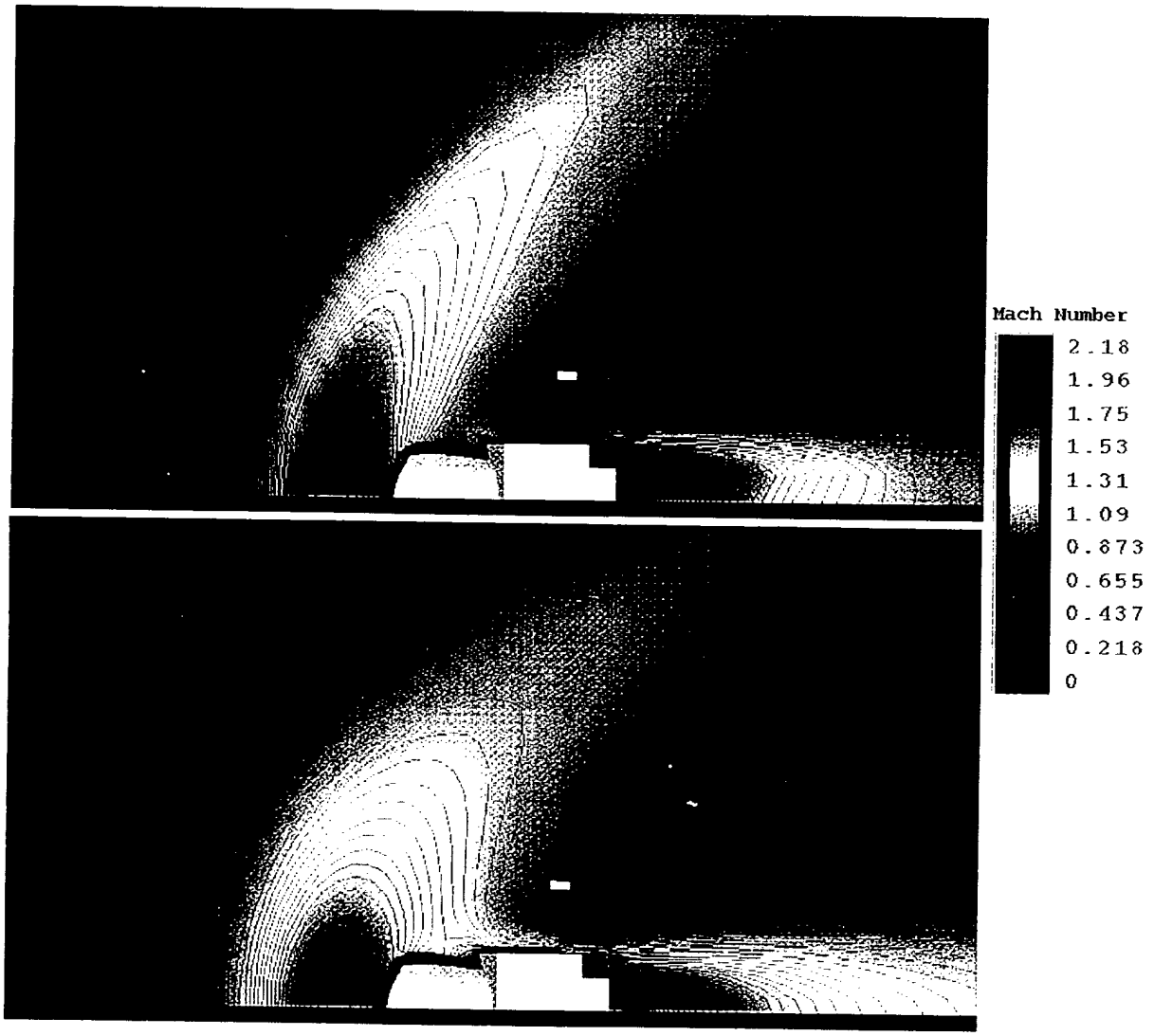

Figure 2-12. Close-Up View of the Frontal Mach Contours. Top: Osher-Chakravarthy Scheme, Bottom: Upwind Scheme

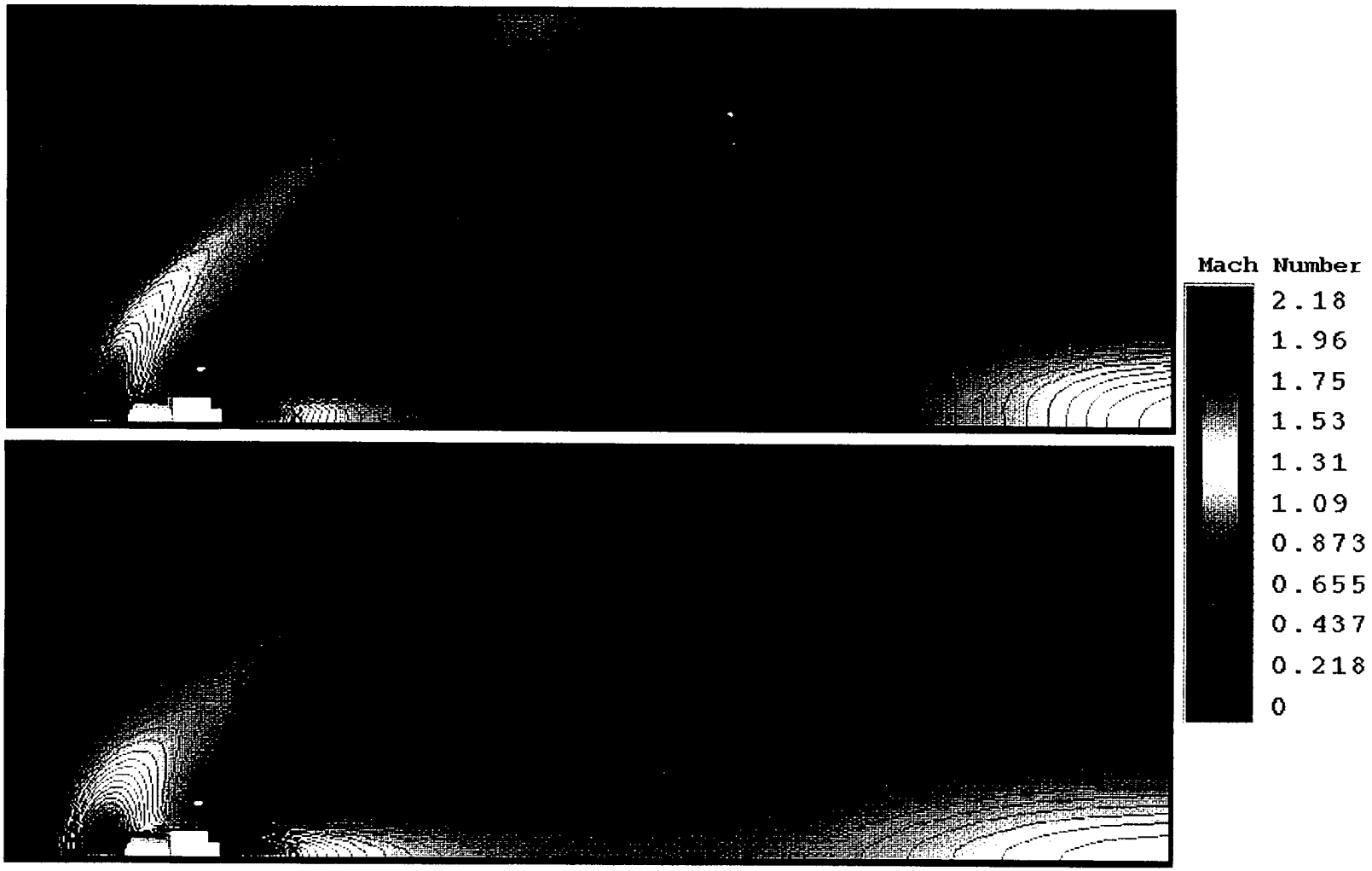

Figure 2-13. Mach Contours for the Entire Computational Domain Behind the Seat. Top: Osher-Chakravarthy Scheme, Bottom: Upwind Scheme

In Phase I of this project, the k-epsilon turbulence model was used for all flow simulations with the REFLEQS-3D code. The k-epsilon model has traditionally been the most widely used for recirculation and wake type flows and has produced the most accurate results [18]. Due to the uncertainties discussed above, a further assessment of turbulence modeling for blunt bodies in general and ejection seat flow in particular was conducted under this Phase II project. This study focused mainly on the use of k-epsilon turbulence model and some of its derivatives (such as RNG model) in conjunction with various differencing schemes. Also a sensitivity study was conducted on the formulation of k-epsilon, by changing certain coefficients (mainly CD), and assessing the effects on the results.

Several calculations and numerical experiments with the k-epsilon model and various differencing schemes gave more insight into the ejection seat and occupant flows and blunt body flows in general. Flows over an ejection seat and occupant possess most of the characteristics discussed above (separation, recirculation, wakes). The Reynolds number is usually very high (> 1.e6), and vast separation and large recirculation zones take place. For the ejection seat problem, however, separation is usually not due to boundary layer growth or effects, it is mainly due to the geometry shape. Separation is caused by the sharp edges and the irregular geometry of the seat and occupant. Therefore this minimizes the importance of turbulence modeling from the boundary layer resolution perspective. However turbulence modeling is still very important to resolve the shape of the wake and the extent of separation. Without proper turbulence modeling, the pressure gradients predictions around the wake may not be accurate. This results in a wrong wake shape, with erroneous wake pressures which in turn affects the prediction of force and moment coefficients for the seat and occupant.

A detailed study of flow over spheres and cylinders was conducted to assess turbulence modeling effects (results are presented in Section 3). These geometries were chosen for economic reasons. This was done with the understanding, as stated above, that large difference in turbulence behavior exist between these flows and ejection seat flows. These differences are mainly related to the separation phenomena. These calculations, however, were chosen to assess the effect of turbulence modeling on the base pressure predictions. The conclusions made from this study were as follow:

- the choice of turbulence model greatly influences the separation point on the cylinder and sphere resulting in large influence on drag predictions.
- the wake base pressure shows very minimal changes as the turbulence model properties change.
- higher speed flows (supersonic) are much less sensitive to turbulence modeling.
- changing the CD coefficient in the k-epsilon model from 0.5 to 0.9 resulted in much better comparison of surface pressures for the cylinder with test data.
- k-ε model predicted better surface pressures at the surface of the cylinder as the grid was refined.

The most important conclusion from the above study was that turbulence modeling was not as important, as originally thought, for ejection seat and occupant calculations. The

difference in force and moment coefficient predictions were minimal when comparing laminar and turbulent results.

A detailed description of this effort will be presented in Section 3 and was also presented in the fifth quarterly progress report and in a AIAA technical paper (AIAA-94-0751) entitled "Validation of CFD Methodology for Ejection Seat Application". This paper is included in Appendix A.

2.3.4 Grid Adaptation for Moving Seat Analysis

Another CFD-ACE adaptation effort that took place under this project was to incorporate a model for grid adaptation to conduct ejection seat and occupant unsteady simulations for a pitching seat (i.e. rotating with respect to SRP). The objective of this effort was to assess transient effects on the prediction of seat aerodynamic characteristics. The results of this study are presented in the next section and were published in a AIAA technical paper (AIAA-95-1837). This paper is included in Appendix A.

The grid adaptation model was extracted from the elliptic grid generator and implemented into CFD-ACE. This model rotates the seat based on user-specified pitch and yaw angle specifications. The attitude control module of the grid generator was adapted so that the pitch angle gets automatically calculated from the time step and angle increments specified by the user. At each time step, the pitch angle gets incremented and the grid gets adjusted accordingly by the attitude control module. This model was used for both 2D and 3D ejection seat analysis (see Section 4 for more details)

2.3.5 Force and Moment Integration Module

A module that calculates the forces and moments with respect to seat SRP was developed in Phase I of this project and incorporated into the REFLEQS-3D code. The same module was carried over to the CFD-ACE code with its capabilities extended. Some of the additions, performed under Phase II, included:

- generalization of the coefficients calculations in all directions and in Standard Body Axis system as well as global axis systems;
- calculation and print out of the force in all 3 directions each iteration (for steady state), and each time step (for unsteady), to monitor solution convergence and stability; and
- adding extra routines to the model to print out forces and pressures on selected portions of the seat (chest and head centerline, seat back centerline, etc) and computational grid (average inlet conditions).

For completeness, this module will be discussed in its entirety, including the Phase I development, in this report.

In this module, the force and moment coefficients are calculated for the seat and occupant each iteration. The force on the seat is caused by the surface normal stresses (i.e. pressure forces), and the surface tangential stresses (i.e. friction force). The pressures

forces are expected to the dominant forces due to the blunt shape of the geometry. The force in the global three directions (x,y and z) is calculated as follows:

$$F_i = \int_1^n \left[\left(P - P_\infty\right) - \tau_s\right] dA \tag{1}$$

where i denotes the direction (x,y, or z) and n denotes the number of cells on the surfaces being modeled. P_∞ is the free stream static pressure and τ_s is the shear stress contributing the skin friction. In the BFC coordinate configurations, the above equation yields the force normal to the cell surface being considered. To get the net force in the x, y, and z direction, Equation (1) is multiplied by the unit vectors (e_1, e_2, e_3). Therefore, Equation (1) becomes:

$$F_x = \int_1^n \left[\left(P - P_\infty\right) - \tau_s\right] dA \cdot e_1 \tag{2a}$$

$$F_y = \int_1^n \left[\left(P - P_\infty\right) - \tau_s\right] dA \cdot e_2 \tag{2b}$$

$$F_a = \int_1^n \left[\left(P - P_\infty\right) - \tau_s\right] dA \cdot e_3 \tag{2c}$$

τ_s is obtained from standard wall functions which assume that the nearwall boundary layer consists of laminar sublayer and a logarithmic layer.

$$u^+ = \begin{cases} y^+ & \text{if } y^+ < 11.5 \\ \frac{1}{\kappa}\ln\left(Ey^+\right) & \text{if } y^+ > 11.5 \end{cases} \tag{3}$$

where

$$y^+ = \frac{y}{\nu}\sqrt{\frac{\tau_w}{\rho}} \quad \text{and} \quad u^+ = \frac{u}{\sqrt{\frac{\tau_w}{\rho}}} \tag{4}$$

κ, the von Karman constant (κ = 0.143), E is a constant equal to 9.0, y is the normal distance from the surface, ρ is the local density, and u is the component of velocity tangential to the surface. Knowing u and y at the first node from the wall, τ_s is obtained iteratively from (3) to (4). The above procedure for computing the force function (2) is performed for each grid cell adjacent to the seat and occupant body.

The seat and occupant "surface adjacent" grid cells are identified by indices transferred to the code via input from the pre-processor. After the forces are calculated, the moments can be calculated as follows:

$$M_z = \int_1^n F_x \cdot dy + F_y \cdot dx \tag{5a}$$

$$M_x = \int_1^n F_y \cdot dz + F_z \cdot dy \tag{5b}$$

$$M_y = \int_1^n F_z \cdot dx + F_x \cdot dz \tag{5c}$$

where dx, dy and dz are the distances to the moment reference. The above three equations are evaluated for each cell at the surface of the seat and occupant. The forces and moments coefficients are then calculated as follows.

$$CF_i = \frac{F_i}{Q \cdot S} \tag{6a}$$

$$CM_i = \frac{M_i}{Q \cdot S \cdot D} \tag{6b}$$

where i denotes the direction (x,y,z), Q is the free stream dynamic pressure calculated as:

$$Q = \frac{1}{2}\rho_\infty V_\infty^2 \tag{7}$$

where

ρ_∞ = free stream density
V_∞ = free stream velocity

S and D are the projected frontal area of the seat/occupant and the hydraulic diameter. Q and S can be specified by the user via the pre-processor. The post-processor can also calculate the projected frontal area, for geometry validation, as follows:

$$A_f = \int_1^n A_i e_n \tag{8}$$

where n denotes the number of modeled cells, A is the normal area of the cell force and e_n is the unit vector normal to the front of the ejection seat positioned at zero angle of attack.

The ejection seat post-processor also dumps PLOT3D files such as the indices of the S/O surfaces so that the modeled surface can be plotted (as shown in the figures in Section 3). After the force and moment coefficients are calculated in the global (fixed) axis system, they are translated to the Standardized Body Axis System (shown in Figure 2-14) using the following transformation matrices:

$$\begin{bmatrix} C_A \\ C_N \\ -C_Y \end{bmatrix} = \begin{bmatrix} \cos\phi\cos\psi & \cos\phi\sin\psi & -\sin\theta \\ -\sin\psi\cos\phi + \sin\theta\cos\psi\sin\phi & \cos\psi\cos\phi + \sin\theta\sin\psi\sin\phi & \cos\theta\sin\phi \\ \sin\psi\sin\phi + \sin\theta\cos\psi\cos\phi & -\cos\psi\sin\phi + \sin\theta\sin\psi\cos\phi & \cos\theta\cos\phi \end{bmatrix} = \begin{bmatrix} C_{Xcfd} \\ C_{Ycfd} \\ C_{Zcfd} \end{bmatrix}$$

where, in the seat body axis system, $C_X = -C_A$ and $C_Z = -C_N$. Note that θ, ψ and ϕ are the pitch, yaw and roll angles, respectively.

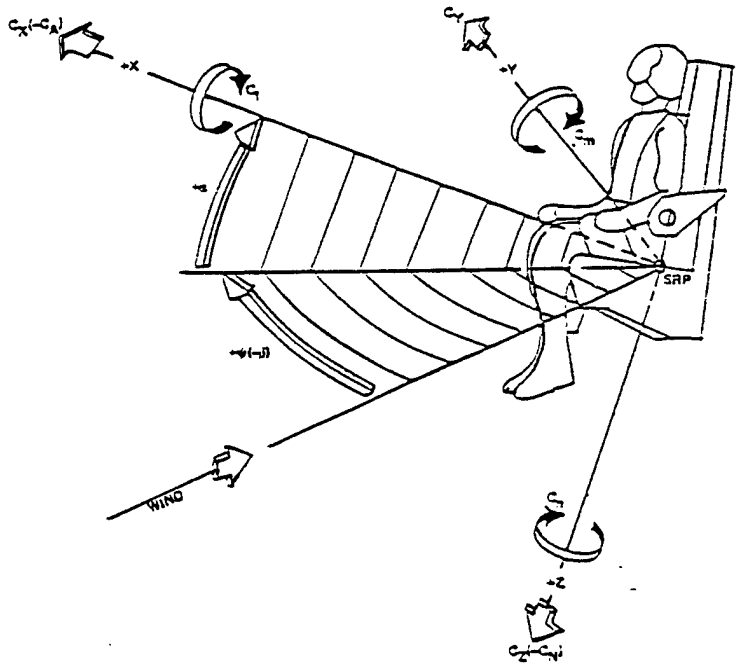

Figure 2-14. Definition of Standardized Body Axis System

2.4 Flow Visualization

CFD-VIEW was exclusively used in this project for in-depth flow analysis and visualization of the seat and occupant results. As in the case of CFD-GEOM, the development of CFD-VIEW, which coincided for the most part with the duration of this project, was affected to a large degree by the requirements of the ejection seat and occupant problem. The salient features of CFD-VIEW include:

- interactive 3D graphics, animation and flow visualization;
- easy and intuitive object-oriented interface;
- fast manipulation of large data sets;
- structured/unstructured/hybrid capability;
- visualization of 3D flow fields through transparent and iso-surfaces;
- CFD function calculator with extensive array of precalculated functions'
- flow ribbons and particle traces;
- interactive point and line data probes;
- interactive animation; and
- seemless integration with CFDRC's flow solvers.

For complete reference, a brochure of CFD-VIEW is included in Appendix B.

3. CFD TOOLS ASSESSMENT AND VALIDATION FOR SEAT/OCCUPANT USING SIMPLE GEOMETRIES

Several efforts took place under this project to demonstrate and validate the methodologies discussed in Section 2 for ejection seat and occupant analysis. Prior to the escape system demonstration and validation tasks, several studies were conducted to assess the tools using simple geometries. These studies were overlapped with the numerical assessment and turbulence modeling efforts described in Section 2.

Two types of validation efforts took place under this project:

1. to validate the basic prediction capabilities of the computational tools on simple blunt body geometries; and

2. to validate the tools against ejection escape system test data.

The computational tools numerical assessment and validation calculations for simple geometries are discussed in this section while the discussions of escape system demonstration and validation calculations are presented in Section 4.

The focus of this work was to assess and enhance the CFD Code physical and numerical modeling capabilities for predicting the correct flow fields for ejection seat applications. This validation process was performed in conjunction with the numerical and turbulence modeling assessment task. Simple benchmark problems were selected to evaluate and validate the various physical and numerical models for prediction of correct ejection seat flow parameters such as shock location and surface and wake pressures. To make the validation process more systematic, efforts were focused on evaluating the influence of various numerical parameters and the effect they have on the flow solutions. The objective of the parametric studies was to address the following questions:

- How do the results depend on the grid clustering and fineness?
- How do the results vary for different differencing schemes?
- What effect does the turbulence model have on the base pressure behind the ejection seat?

These questions must be answered and their effects quantified for the ejection seat simulations to be meaningful. Since the ejection seat is a complicated 3-D geometry it is not practical or possible to perform parametric studies on workstation class machines to answer the questions above. Thus, simpler geometries were chosen that feature similar characteristics to the ejection seat. The geometries chosen include:

a. 2-D cylinder;
b. 2-D half cylinder (cylinder with the rear cut away); and
c. 3-D sphere.

The purpose of the 2-D simulations was mainly one of cost. A large number of relevant simulations could be completed and specific trends relating to the questions above could be answered. The full cylinder flow study was selected to determine the effect of grid clustering, differencing schemes and turbulence models on the separation point and the resulting base pressure to quantify these effects on the drag produced. The half cylinder flow problem has been selected to determine the effect of grid clustering, differencing schemes and turbulence models on the base pressure, and hence drag, for a body with a geometric discontinuity which automatically determines separation. The sphere was selected to verify that the trends and the magnitudes observed in 2-D are also true in 3-D.

This work was fully documented and presented at the 32nd AIAA Aerospace Sciences meeting in Reno (Jan. 1994, AIAA-94-0751). The paper title is "Validation of CFD Methodology for Ejection Seat Applications,". This technical paper is included in Appendix A. A more detailed description of the cylinder results was also presented in the fifth quarterly progress report [8].

The discussion here will give a summary of this work including the conclusions made from these studies.

3.1 Flow Over a Cylinder

The purpose of simulating flow over a cylinder was to determine if the CFD code could predict the quantitative features of a separating flow field. The cylinder flow is a particularly difficult test case since the separation point and base pressure must be accurately predicted to predict an accurate value of drag. In this sense this is a more difficult test case than the ejection seat since the separated flow region for the ejection seat is caused by a geometric discontinuity. The 2-D cylinder simulations have been completed for Mach Numbers of 0.177, 0.74 and 2.0 for a Reynolds Number based on the cylinder diameter of 8.27×10^6. The Mach 0.177 case was chosen due to the existence of experimental surface pressure data while the Mach 0.74 and 2.0 cases are speed ranges of interest for present and future ejection seat simulations.

Problem Statement Only half of the cylinder geometry is analyzed due to the symmetry of the problem. A full cylinder case was selected to verify that the resulting pressure field was symmetric. Figure 3-1 sketches the computational domain and the boundary conditions used in the present simulation. The outer boundary was purposely extended far from the inner cylinder (R_{outer}=55.0, R_{inner}=0.9538) to negate any outer boundary condition effects. The parameter b is the angle around the cylinder from the stagnation point and ranges from 0 to 180. This parameter is used to describe the surface pressure field.

One must note that the real flow over a cylinder at this Reynolds number is an unsteady turbulent flow resulting in oscillating vortices being shed in the wake. These simulations do not attempt to capture these unsteady effects, but rather to obtain time averaged solution resulting in a time averaged pressure and drag.

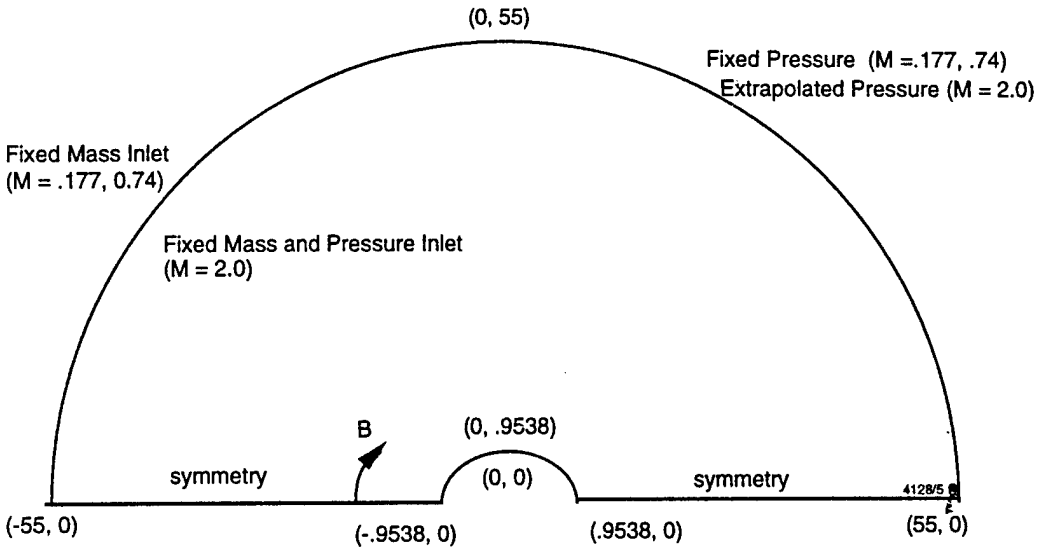

Figure 3-1. Sketch of O-Grid and Boundary Conditions

<u>Variable Parameters</u> The parameters varied within this cylinder study include the grid fineness in both the streamwise and radial direction, the type of differencing scheme used for the velocities and pressure, and the turbulence model used. Six different grids, four differencing schemes and three variations of the k-ε turbulence model were used during this study. In addition a couple of cases without turbulence modeling (i.e. laminar flow) were run to show the differences between variable viscosity turbulent and constant viscosity solutions. The 6 grids include:

a. 59 (streamwise) x 88 (radial) nodes, $D=2.621\times10^{-3}$ (new.PUG)
b. 59 x 88, $D=2.621\times10^{-4}$, (new_f.PUG)
c. 59 x 88, $D=2.621\times10^{-5}$. (new_f2.PUG)
d. 149 x 88, $D=2.621\times10^{-5}$, (new_f3.PUG)
e. 199 x 132, $D=2.621\times10^{-5}$, (new_f8.PUG)
f. 199 x 132, $D=2.621\times10^{-6}$, (new_f10.PUG)

where D is the perpendicular distance of the first radial cell from the cylinder surface divided by the cylinder diameter. Note that not all of these grids were used at each flow speed. Expressions in parenthesis will be used on the plots to denote each grid type. Figure 3-2 shows a picture of each of the grid density.

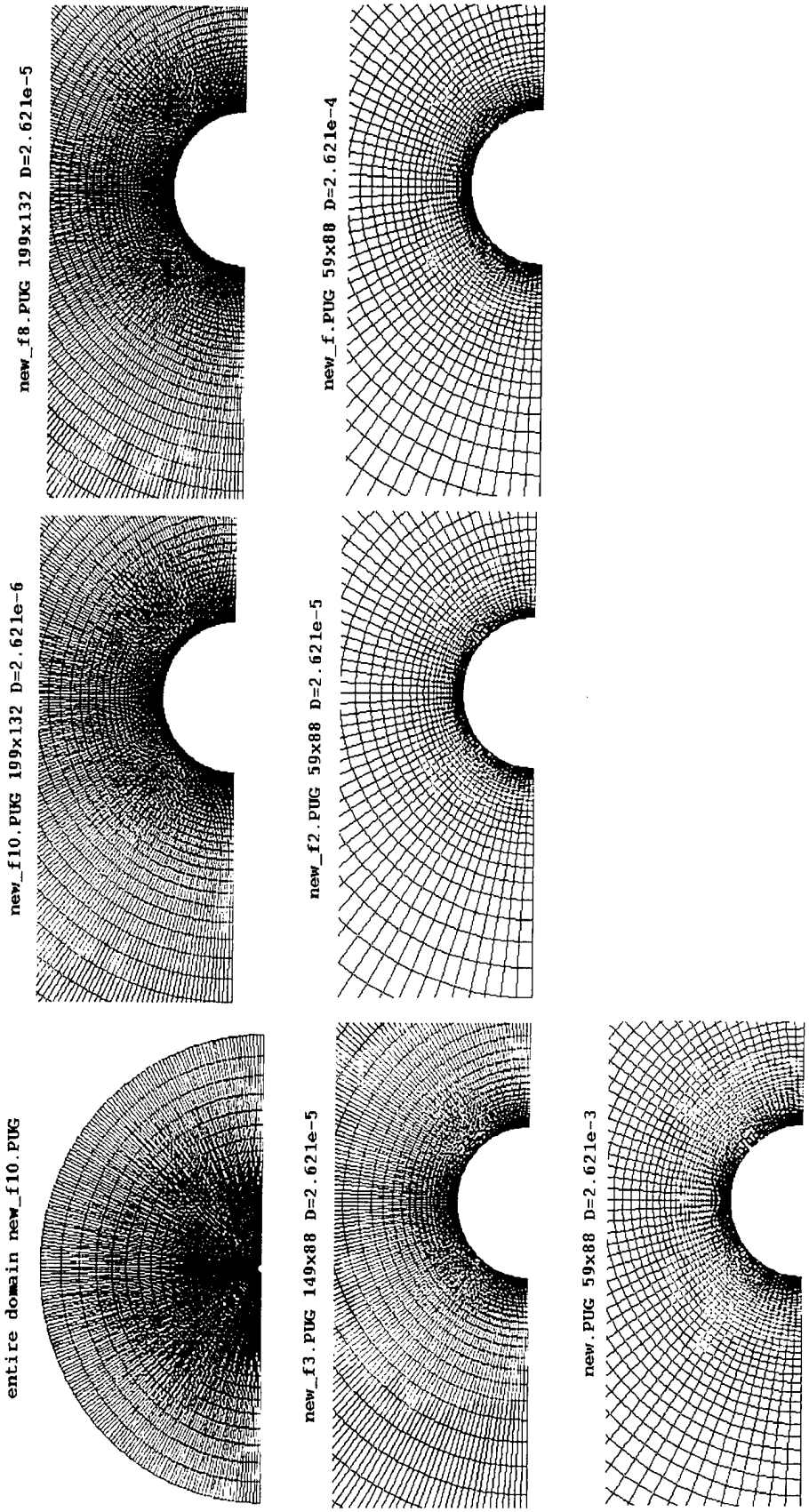

Figure 3-2. The Six Grids Used during the 2-D Cylinder Parametric Studies. Note that each grid has same outer domain Router = 55, Reyl = 0.9538

Four differencing schemes were used during these simulations. For each flow speed and grid, the first order upwind, second order upwind and central differencing options were used. Osher differencing was used in selected cases.

Three forms of the k-ε turbulence were used in these simulations. The base formulation was the standard k-ε model of Launder and Spaulding [19], the first variation is the Launder and Spaulding model with the value of CD=.05 (nt=CD(k^2/e) and normally CD=0.09), and the third form is the Low Reynolds number model of Chien [20]. The boundary conditions for the Launder and Spaulding model use wall functions, if y+<11.5 the shear stress is computed using a linear velocity profile (laminar wall) while if y+>11.5 the shear stress is computed using the log law of the wall. For the Low Reynolds number model the shear stress is computed by always assuming a linear velocity profile, hence to be accurate several cells must be within the laminar sub-layer.

For the M=0.177, Re=8.27x10^6 case two sets of experimental data measuring the surface pressures are applicable for comparison, data of Jones [21] and Roshko [22]. Jones data is available for above conditions while Roshko's data is for M~0.25, Re=8.4x10^6. These data sets are presented in the following plots. Note that one of Roshko's data points (at b=80) is a bad data point without physical significance.

Figure 3-3 shows the general qualitative flowfield patterns for each Mach number. In the M=0.177 case the flow is entirely subsonic and eventually separates at the rear of the cylinder. The M=0.74 flow shows that as the flow accelerates an essentially normal shock forms and the flow separates. For M=2.0 flow a bow shock is located in front of the cylinder and the flow separates near the rear of the cylinder. In each case the drag is largely determined by where the separation point is located and also by the resulting base pressure in the separated region. Both the separation location and resulting base pressure is influenced by the turbulence models, differencing schemes and grid resolution. Parametric studies quantifying these effects are described below.

3.2 M=0.177 Results

The ejection seat simulations conducted to date and planned for the future are in the Mach Number range of 0.3 to 2.0. However, due to the existing experimental data for M=0.177, this test case was chosen as a validation case. In addition these results will be valuable in assessing the CFD methodology for low subsonic test cases if so desired in the future.

For each of the grids (except new_f3.PUG) the first order upwind, second order upwind and central differencing schemes were run with the standard Launder and Spaulding model (CD=.09). The Osher scheme was also run for new_f10.PUG while a laminar case was run for the new_f2.PUG grid. The values of the maximum y+ at M=0.177 for the first cell from the wall is given in Table 3-1. The resulting surface pressures along with the experimental results for each of the grids is shown in Figure 3-4a-d.

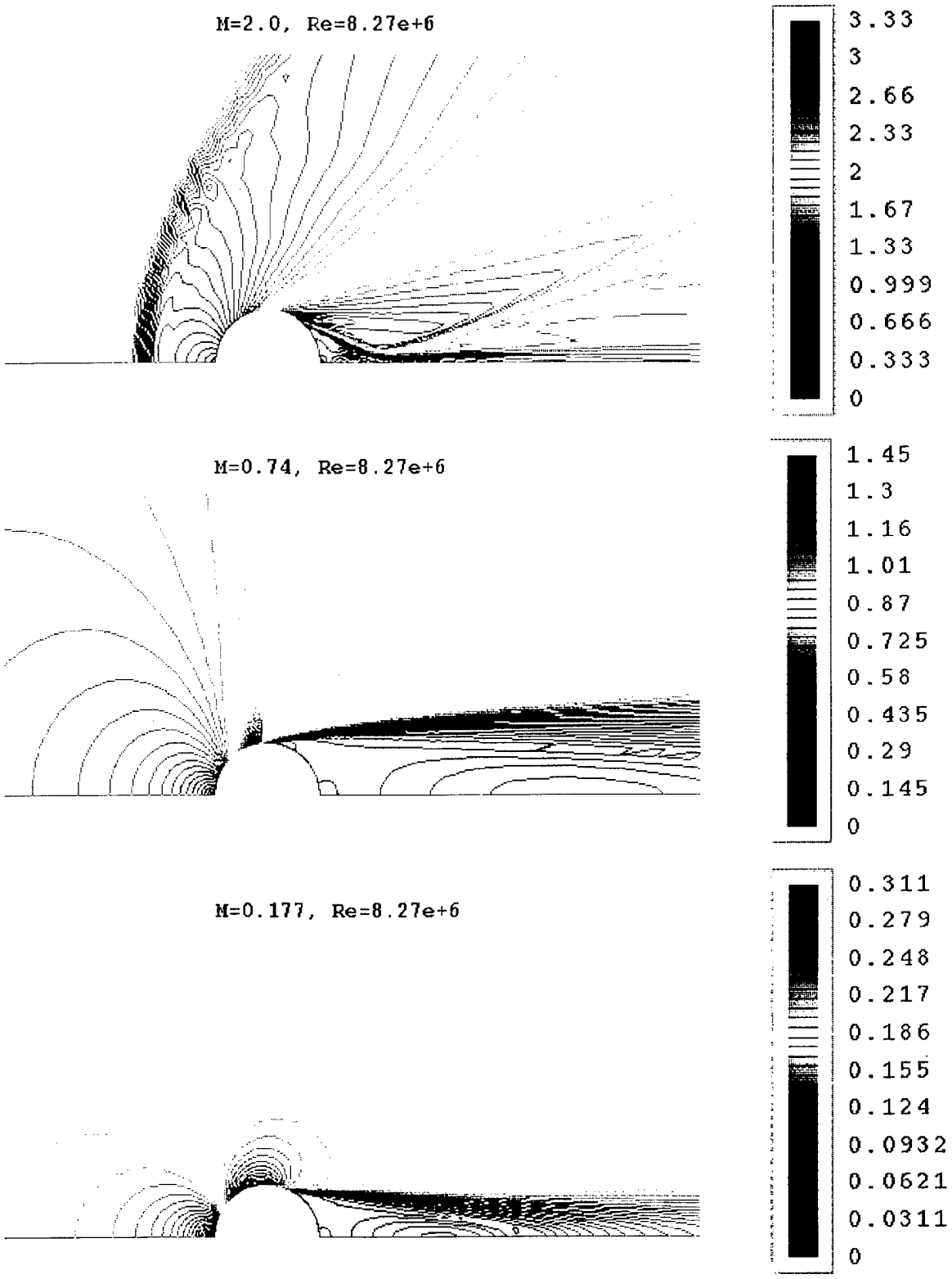

Figure 3-3. Mach Contours for Subsonic, Transonic, and Supersonic Flow Past a Cylinder

Table 3-1. Values of y+ for Each Grid a M = 0.177

Grid	D	y^+
new.PUG	2.621×10^{-4}	$y^+ < 600$
new_f.PUG	2.621×10^{-4}	$y^+ < 56$
new_f2.PUG	2.621×10^{-5}	$y^+ < 6$
new_f8.PUG	2.621×10^{-5}	$y^+ < 6$
new_f10.PUG	2.621×10^{-6}	$y^+ < 0.7$

4128/512

A noticeable characteristic of Figures 3-4a-d is the discrepancy between the Upwind (first order upwind) and the SOU (second order upwind) and central results. The SOU and Central results are very similar for each grid while the Upwind results always predict later separation. This observation is easily explainable by the fact that the Upwind scheme has a greater component of numerical viscosity which delays separation. Also note for the new_f10.PUG grid the Osher scheme is very similar to the SOU and central results. Notice however that regardless of the differencing scheme used the resulting computational prediction of base pressure is nearly the same. Thus, the numerical viscosity plays a very limited role in the final calculation of base pressure. For the laminar case run in Figure 3-4c separation occurs much earlier than the turbulence cases and the base pressure in the separated region is not constant. Since the case run is physically a turbulent flow, these differences are expected and are shown only for comparative purposes.

Another noticeable characteristic of Figures 3-4a-d is the difference between the experimental and computational results. None of the grids or differencing schemes using the standard Launder and Spaulding model adequately compares to the experimental results. Note also that there is some discrepancy between the experimental results. Both sets of experimental data predict similar pressures in the front of the cylinder and only begin to substantially differ near separation. The point of separation can be deduced from these plots by locating the beginning point of constant base pressure. In each of the experimental results this occurs near b=105. However, the resulting constant base pressure is different which results in substantially different drag values. Jones states that the drag differences are probably due to the different values of cylinder roughness (Roshko's cylinder has a roughness factor, the roughness height to diameter, six times larger than Jones). The roughness factor does not seem to affect the separation location but rather the base pressure in the separation region. Since the turbulence model does not have any "roughness" model the pressure discrepancy in the base pressure may be explainable by similar reasoning. The rougher the surface the lower the base pressure will become. Thus, the computational results with assumed smooth surfaces have higher base pressures than Jones' results which have higher base pressures than Roshko's. The lower base pressure results in substantially greater drag.

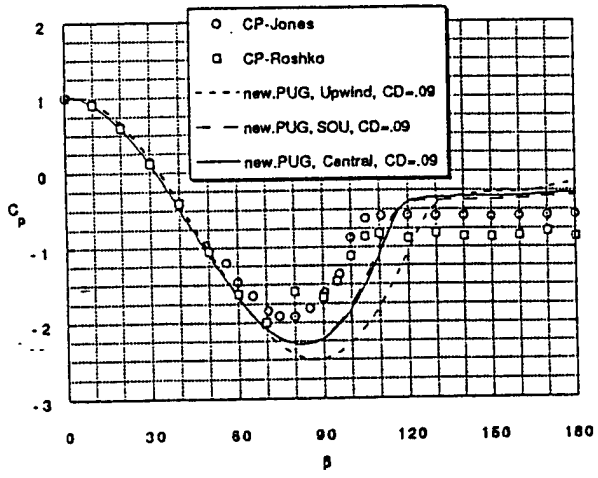

a.

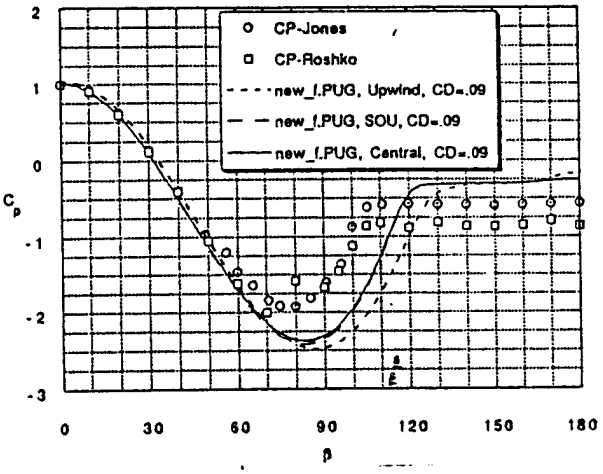

b.

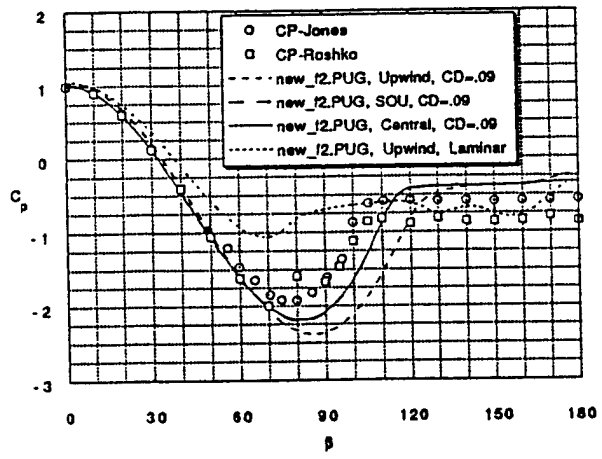

c.

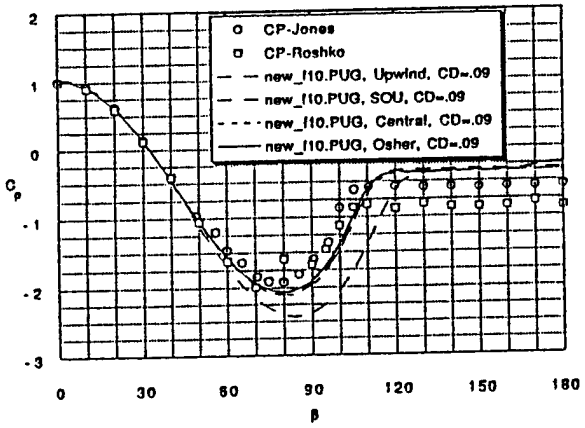

d.

Figure 3-4. Surface Pressure Comparison for Different Grids and Differencing Schemes Using the Standard Launder and Spaulding Turbulence Model for M = 0.177, Re = 8.27×10^6 Flow Over a Cylinder

The discrepancy between the computational and experimental separation point is not explainable by the above reasoning. Cylinder flow at Re=8.27×10^6 is turbulent flow regardless of the cylinder roughness, hence the separation point should be similar for cylinders of varying roughness. This is evident in the experimental results, however, the computational results always predict separation aft of the experimental separation regardless of the grid refinement. Clearly the SOU, Central and Osher schemes are closer to the separation prediction than the Upwind scheme and this is due to the greater numerical viscosity in the upwind scheme. The separation location is vitally dependent on the viscosity near the wall. For example a laminar flow case predicts separation much earlier than a turbulent case (and hence results in much greater drag) due to the lower viscosity. The total viscosity near the wall is the summation of the laminar, turbulent and numerical viscosities. The second order schemes reduce numerical viscosity. Assuming for the moment that a higher order scheme (third order accurate) will not substantially further reduce the viscosity, the extra viscosity must be coming in the turbulence model.

A simple way to reduce the turbulent viscosity is to reduce the parameter CD since turbulent viscosity is directly proportional to CD. The typical value for CD is a constant of 0.09, however, this constant is based on jet or mixing layer flow in 2-D. For axisymmetric jets Launder and Spalding use a variable CD and for the Low Reynolds number model they describe in Reference 19 based on Jones and Launder [23,24] a variable CD, based on the turbulent Reynolds number is used. The equation used is

$$C_D = C_{D\infty} \; \mathrm{Exp}[\, -2.5/\,(1+R_t/50)\,]$$

$$C_{D\infty} = .09, \quad R_t = k^2/(\nu\varepsilon)$$

The range of CD is from a minimum of .0074 at $Re_t=0$ to .09 at $Re_t=\infty$. Very near the wall in the laminar sub-layer the turbulent Reynolds number is small thus CD should be less than 0.09. A constant value of 0.05 (corresponding to a typical turbulent Reynolds number near the wall of 160) is used to determine what effect this parameter has on separation.

Figure 3-5a-c show the effect of CD on the surface pressure curve for new_f8.PUG for the Upwind, SOU and Central schemes. In each case the CD=.05 case shows earlier separation than the CD=.09 case. However, the resulting constant base pressure value is the same regardless of CD. This shows the effect of the viscosity on separation and the lack of effect on the base pressure in the separation region.

The Low Reynolds Number model of Chien [25] is applied to this problem using the Central and Osher schemes on the new_f10.PUG grid. Note however that Chien also uses a constant CD=.09. Since the value of y+<1 for all cells, the Low Reynolds number model should be theoretically more valid than the standard since it is a high Reynolds number model. However, the Low Reynolds number model compared poorer to experiment than the standard. Since this model is harder to converge and it is not

applicable for coarser grids near the wall it is not usable for the ejection seat application and hence no further results will be presented on the cylinder test case using this model.

Figures 3-6a-c show results for different grids using Upwind, SOU, and Central differencing using CD=0.05. Note in each case that the new.PUG and new_f.PUG cases are somewhat different than the latter three grids. Both new.PUG and new_f.PUG have y+ values greater than 11.5 and hence use the logarithmic wall functions while new_f2.PUG, new_f8.PUG, and new_f10.PUG all have y+<11.5 resulting in the linear wall function. Note that new_f10.PUG has y+<0.7 while new_f2.PUG and new_f8.PUG have y+<6. The differences between new_f8.PUG and new_f10.PUG are small showing that only a few points are necessary in the laminar sub-layer to obtain an adequate pressure prediction. The poor predictions of new.PUG and new_f.PUG show that even with wall functions the pressure prediction is inadequate. The differences between new_f2.PUG and new_f8.PUG show the difference in surface pressure prediction for a refined grid. These differences are small for the Central case and slightly more pronounced for the SOU and Upwind case. This indicates that upwind differencing schemes are more sensitive to the streamwise point distribution which may be due to the Upwind biasing nature of the schemes.

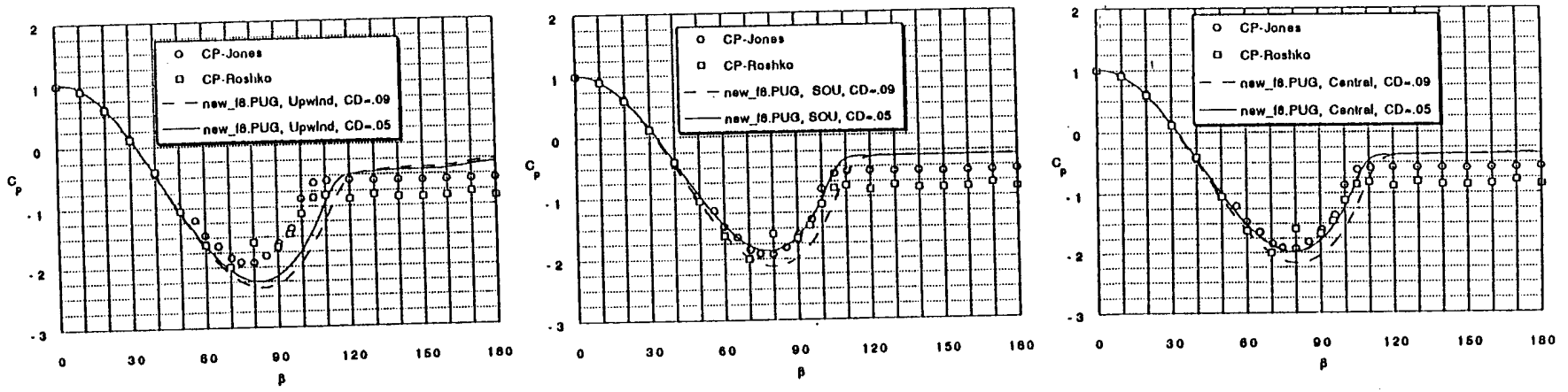

Figure 3-5. Comparison of Surface Pressures Using the Standard k-ε Model with CD = .09 and Modified k-ε Model with CD = .05 for Various Grids and Differencing Schemes for M = 0.177, Re = 8.27 x 10^6 Flow Over a Cylinder

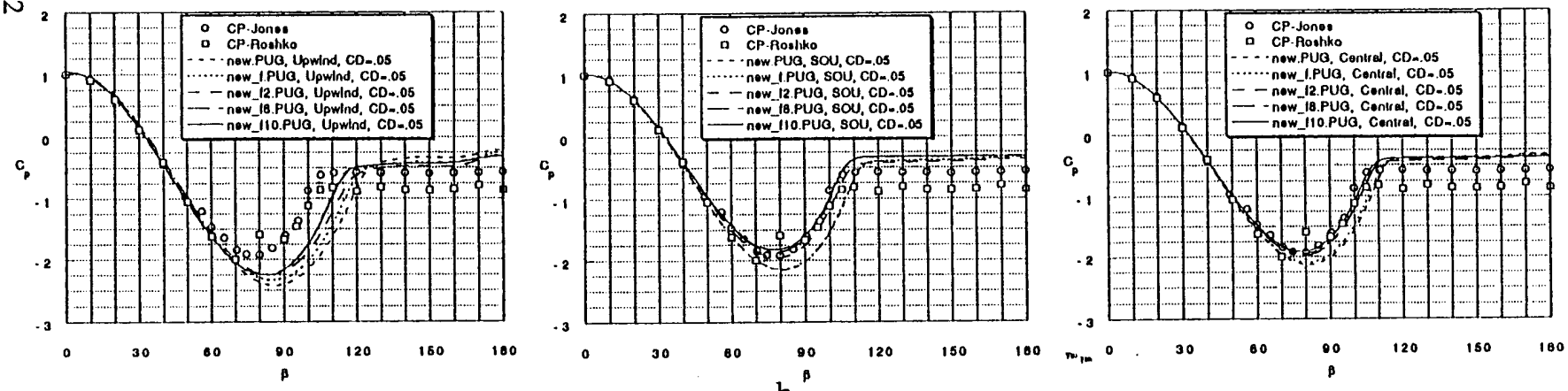

Figure 3-6. Comparison of Surface Pressures for Varying Grids and Differencing Schemes Using the Modified k-ε Model (CD = .05) for M = 0.177, Re = 8.27 x 10^6 Flow Over a Cylinder

The values of pressure drag, skin friction drag and total drag are tabulated for each of the cases run in Table 3-2. Note that the computed drag values range between 0.236 to 0.479 while the two experimental values of drag are 0.532 and 0.709. Thus, drag was always underpredicted and this was due to the higher base pressure values obtained in the separation region. The Upwind scheme predicted drag closer to experimental however, this is due to the shift in the Cp curve around separation which is due to the erroneous separation prediction as seen in the pressure plots. Ironically the most inaccurate scheme gives the drag value closest to experiment even though the major aspects of the flowfield are inaccurate.

Table 3-2. Drag Coefficient Tabulations for M = 0.177

Grid	Differencing Scheme	Turb.Par. C_D	Pressure Drag C_{D_p}	Skin Friction Drag C_{D_f}	Total Drag C_{D_T}
new.PUG	upwind	.09	.373	2e-4	.373
new.PUG	sou	.09	.274	1.0e-4	.274
new.PUG	central	.09	.255	1.7e-4	.255
new,PUG	upwind	.05	.391	1.7e-4	.391
new.PUG	sou	.05	.296	1.5e-4	.296
new.PUG	central	.05	.281	1.4e-4	.281
new_f.PUG	upwind	.09	.391	1.33e-3	.392
new_f.PUG	sou	.09	.225	1.28e-3	.226
new_f.PUG	central	.09	.235	1.28e-3	.236
new_f.PUG	upwind	.05	.432	1.16e-3	.433
new_f.PUG	sou	.05	.289	1.09e-3	.290
new_f.PUG	central	.05	.295	1.09e-3	.296
new_f2.PUG	upwind	.09	.434	5.9e-2	.440
new_f2.PUG	sou	.09	.282	5.5e-2	.288
new_f2.PUG	central	.09	.296	5.6e-2	.301
new_f2.PUG	upwind	.05	.475	4.8e-2	.479
new_f2.PUG	sou	.05	.339	4.4e-2	.343
new_f2.PUG	central	.05	.346	4.4e-2	.351
new_f8.PUG	upwind	.09	.318	5.9e-2	.324
new_f8.PUG	sou	.09	.250	5.5e-2	.255
new_f8.PUG	central	.09	.268	5.6e-2	.273
new_f8.PUG	upwind	.05	.346	5.6e-2	.351
new_f8.PUG	sou	.05	.280	4.5e-2	.285
new_f8.PUG	central	.05	.293	4.7e-2	.297
new_f10.PUG	upwind	.09	.306	1.2e-2	.318
new_f10.PUG	sou	.09	.247	1.04e-2	.257
new_f10.PUG	central	.09	.286	1.03e-2	.296
new_f10.PUG	osher	.09	.275	1.01e-2	.285
new_f10.PUG	upwind	.05	.352	8.9e-3	.362
new_f10.PUG	sou	.05	.282	7.65e-3	.290
new_f10.PUG	central	.05	.319	7.84e-3	.326
new_f10.PUG	sou	low	.242	7.29e-3	.249

4128/5 13

Experimental Jones $C_{D_p} = .532$ Experimental Roshko $C_{D_T} = .709$

In terms of percentages the various effects of grid resolution, turbulence model and differencing scheme had a rather large effect on the predicted drag and these differences were due entirely to separation point prediction and base drag prediction. In addition the comparison to experiment was rather poor due to the roughness effects mentioned earlier. Fortunately at higher Mach Numbers, where the ejection seat simulations are being completed, these percentage differences are not as large.

3.3 M=0.74 Results

This speed has been widely used for ejection seat flow simulations both in the wind tunnel and using CFD methods and hence is chosen as a test case for the cylinder.

For the M=0.74 flow condition the Upwind, SOU and Central differencing schemes were used on new_f.PUG, new_f2.PUG and new_f10.PUG. In addition the Osher differencing scheme was used on the new_f10.PUG and a laminar case was run for the new_f2.PUG grid. Note that the maximum value of y+ for each of the three grids was 2500, 26, and 0.7.

Figures 3-7a-c show the various differencing schemes on the three grids using CD=.09. Note once again the large difference between the Upwind cases and the SOU and Central cases. The SOU, Central and Osher cases are similar although slight differences exist in the base pressure region for new_f10.PUG and new.PUG. Ironically for the new_f2.PUG case SOU and Central are almost identical. Note that for the various grids the base pressure for the Central case is almost identical while the SOU and Upwind cases varies slightly for each grid. The laminar case run shows similar differences to the turbulent results as shown in the M=0.177 case.

Figures 3-8a-c show the effect of using a constant CD=.05. Separation occurred earlier for each differencing scheme using CD =.05 just as for the M=0.177 case however, the base pressure in the separation region also changed which was not the case at M=0.177. What is especially noticeable in the SOU and Central case is the "shifting" of the CP plot based on separation location. As witnessed in Figure 3-2 the location of the normal shock and the separation location are related i.e. the shock/boundary layer interaction causes separation. This interaction causes the difference in base pressure. Figures 3-7a-c also correlate the shock location to the final base pressure values.

Figures 3-9a-c show the effect of the grid refinement using Central, Upwind, and SOU differencing with CD=.05. Note that as the grid is refined separation occurs earlier, however, the differences are slightly less for the Central case than the Upwind and SOU cases. In addition the Central case predicts essentially the same base pressure regardless of grid used while the SOU and Upwind cases show slightly more differences.

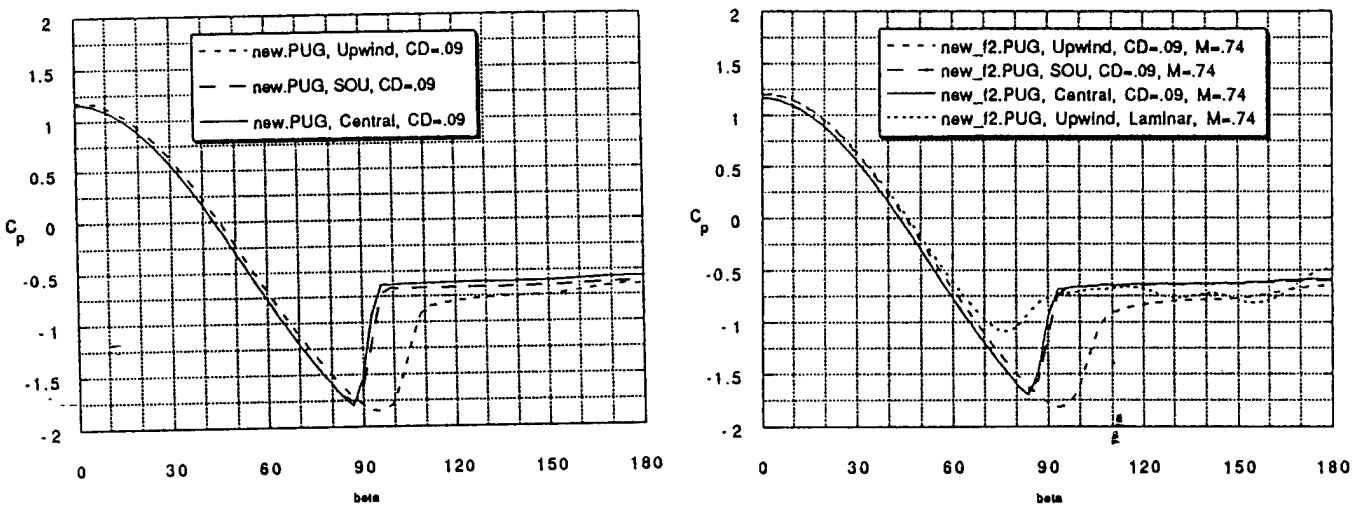

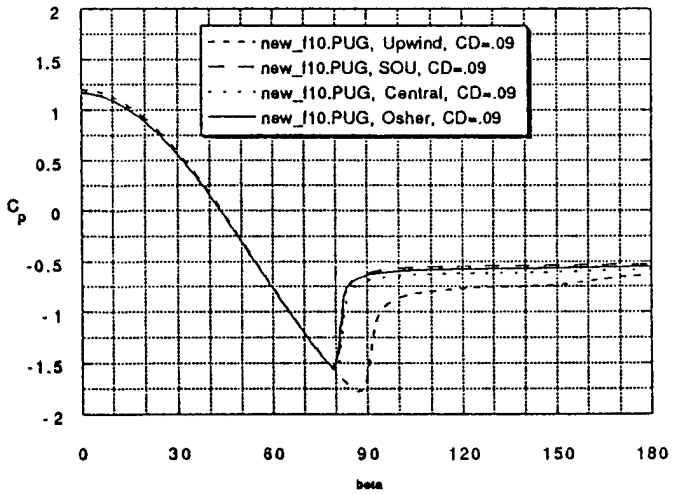

c.

Figure 3-7. Surface Pressure Comparison for Different Grids and Differencing Schemes Using the Standard Launder and Spaulding Turbulence Model for M = 0.74, Re = 8.27 x 10^6 Flow Over a Cylinder

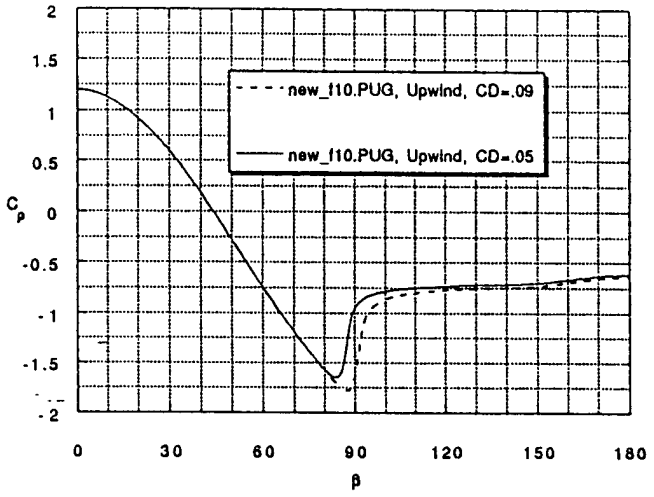

a.

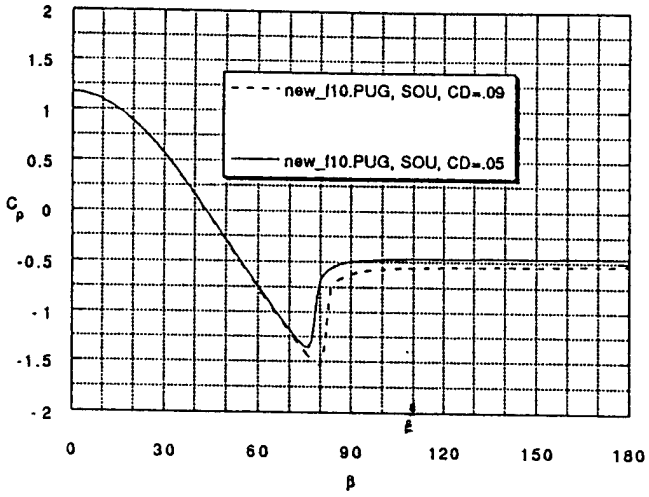

b.

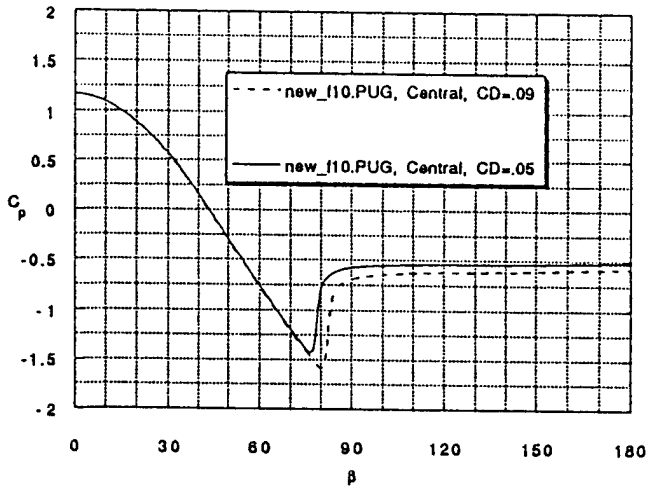

c.

Figure 3-8. Comparison of Surface Pressures Using the Standard k-ε Model with CD = .09 and Modified k-ε Model with CD = .05 for Various Grids and Differencing Schemes for M = 0.74, Re = 8.2×10^6 Flow Over a Cylinder

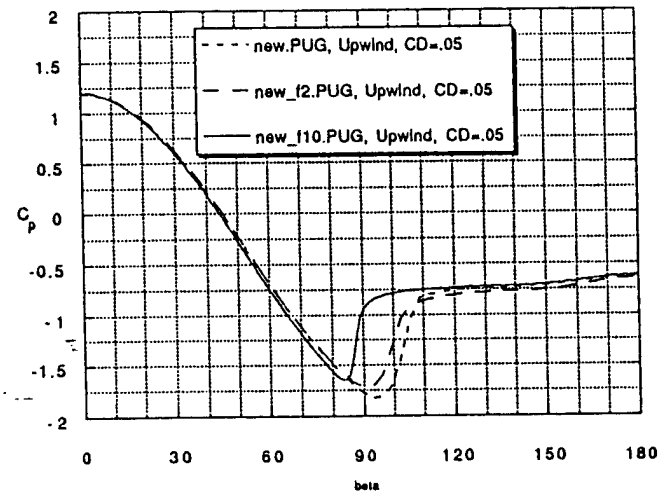

a.

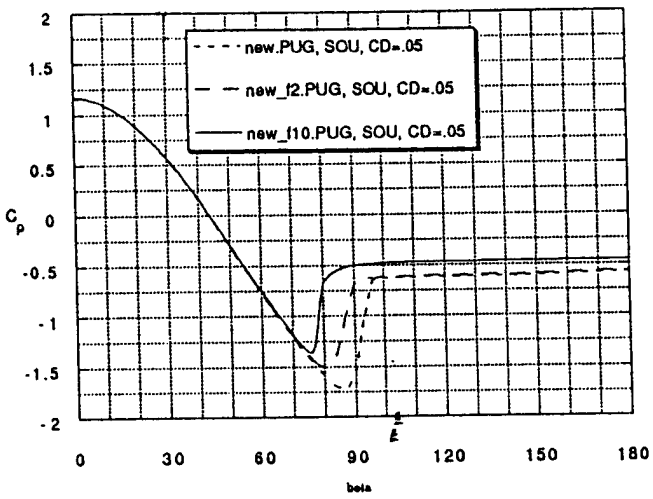

b.

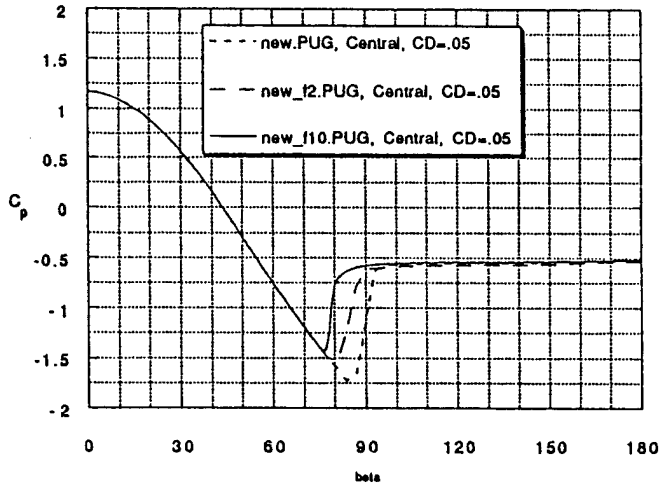

c.

Figure 3-9. Comparison of Surface Pressures for Varying Grids and Differencing Schemes Using the Modified k-ε Model (CD = .05) for M = 0.74, Re = 8.27 x 10^6 Flow Over a Cylinder

Tabulated drags for each of the cases run at M=0.74 are given in Table 3-3. Note that values of drag range from 0.812 to 1.168 for all of the cases run. Discounting the Upwind cases the range is from 0.812 to 0.964 which is a 15% difference from high to low. Discounting both SOU and Upwind cases the range is from 0.862 to 0.932 which is a 7.5% difference. For a given CD value and differencing scheme the discrepancy is even less (central 0.916 to 0.932 1.7%). For this case Central differencing gives the most consistent values of drag for different grids which shows it is less grid dependent than SOU and Upwind. This is very important for the ejection seat which has y+ on the order of 3000 much like the new.PUG grid.

Table 3-3. Drag Coefficient Tabulations for M = 0.74

Grid	Differencing Scheme	Turb. Par. C_D	Pressure Drag C_{D_p}	Skin Friction Drag C_{D_f}	Total Drag C_{D_T}
new.PUG	upwind	.09	1.139	1.31e-4	1.14
new.PUG	sou	.09	.964	1.02e-4	.964
new.PUG	central	.09	.916	1.06e-4	.916
new,PUG	upwind	.05	1.110	1.28e-4	1.110
new.PUG	sou	.05	.918	106e-4	.918
new.PUG	central	.05	.862	1.00e-4	.862
new_f2.PUG	upwind	.09	1.168	5.57e-3	1.174
new_f2.PUG	sou	.09	.947	4.65e-3	.952
new_f2.PUG	central	.09	.932	4.52e-3	.937
new_f2.PUG	upwind	.05	1.14	4.66e-3	1.15
new_f2.PUG	sou	.05	.913	3.89e-3	.917
new_f2.PUG	central	.05	.889	3.75e-3	.893
new_f10.PUG	upwind	.09	1.07	1.42e-2	1.084
new_f10.PUG	sou	.09	.870	1.25e-2	.883
new_f10.PUG	central	.09	.936	1.23e-2	.944
new_f10.PUG	osher	.09	.895	1.24e-2	.907
new_f10.PUG	upwind	.05	1.038	1.03e-3	1.048
new_f10.PUG	sou	.05	.812	9.70e-3	.822
new_f10.PUG	central	.05	.880	9.56e-3	.889

4128/5 t4

Since no experimental results exist for this case it is difficult to quantify the accuracy of the computation. The good point observed from these cases is that the difference in drag obtained for different grids, turbulence models and differencing schemes is quantitatively less than the M=0.177.

3.5 M=2.0 Results

For the M=2.0 flow condition the Upwind, SOU and Central schemes were run on the new.PUG, new_f2.PUG, and new_f3.PUG grids using CD=.05 and .09. The new.PUG grid had y+<4400 while new_f2.PUG and new_f3.PUG had y+<50. A grid with very small y+ values did not converge.

Figures 3-10a-c show the Upwind, SOU, and Central differencing schemes for the three grids using CD=.09. In addition the Osher differencing scheme was completed on new_f3.PUG and a laminar case was run for the new_f2.PUG grid. The differences between the surface pressure plot for the various differencing schemes was much less noticeable than the previous two flow conditions, especially on new.PUG and new_f2.PUG. For the new_f3.PUG case, which has grid refinement in the streamwise direction, the SOU case predicts earlier separation than the Central and Osher cases. Previously the SOU and Central cases were very similar. However, for this particular case this is not true. Since Osher is very similar to Central this is the more reliable simulation. In addition the laminar case predicts earlier separation, however, the base pressure region is much more constant than the M=0.177 and 0.74 cases. The laminar results are in general very similar to the turbulent results which is a radical departure from the M=0.177 and M=0.74 cases.

Several calculations were performed to assess the effect of changing CD on this problem. The differences were found to be minimal. Hence the turbulence model seems to have much less of an effect on the separation point as compared to the M=0.177 and M=0.74 case.

Figures 3-11a-c show the differences between the grids for the Upwind, SOU and Central differencing using CD=.05. For the Central and Upwind cases there are some slight differences in separation point, however this doesn't greatly affect the surface pressures and hence the drag. For the SOU case the new_f3.PUG case predicts much earlier separation. As mentioned above this is as yet unexplained.

Drag values for each of the cases run at M=2.0 is given in Table 3-4. The range of drag values is much less than either the M=0.177 or M=0.74 cases due to the relative similarity of the surface pressure curves. The range of drag values is from 1.348 to 1.433 resulting in a 6% discrepancy. Thus, the drag prediction of the M=2.0 flow case is very insensitive to grid refinement, differencing scheme or turbulence model.

Table 3-4. Drag Coefficient Tabulations for M = 2.0

Grid	Differencing Scheme	Turb. Par. C_D	Pressure Drag C_{D_p}	Skin Friction Drag C_{D_f}	Total Drag C_{D_T}
new.PUG	upwind	.09	1.403	1.25e-4	1.403
new.PUG	sou	.09	1.433	1.30e-4	1.433
new.PUG	central	.09	1.395	1.23e-4	1.395
new,PUG	upwind	.05	1.402	1.24e-4	1.402
new.PUG	sou	.05	1.432	1.30e-4	1.432
new.PUG	central	.05	1.387	1.22e-4	1.387
new_f2.PUG	upwind	.09	1.395	6.2e-3	1.401
new_f2.PUG	sou	.09	1.425	6.41e-3	1.432
new_f2.PUG	central	.09	1.397	6.33e-3	1.403
new_f2.PUG	upwind	.05	1.393	5.66e-3	1.399
new_f2.PUG	sou	.05	1.426	5.95e-3	1.432
new_f2.PUG	central	.05	1.391	6.00e-3	1.398
new_f3.PUG	upwind	.09	1.397	6.22e-3	1.403
new_f3.PUG	sou	.09	1.365	5.58e-3	1.371
new_f3.PUG	central	.09	1.417	6.08e-3	1.423
new_f3.PUG	osher	.09	1.403	6.11e-3	1.408
new_f3.PUG	upwind	.05	1.392	5.60e-3	1.399
new_f3.PUG	sou	.05	1.348	4.96e-3	1.353
new_f3.PUG	central	.05	1.412	5.66e-3	1.418

4128/5 t5

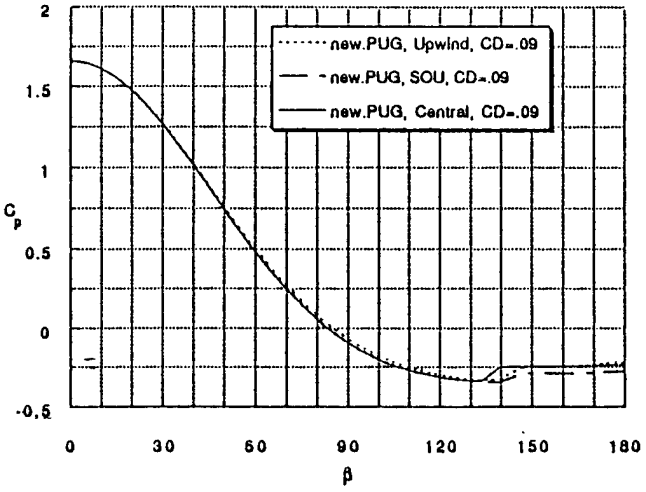

a.

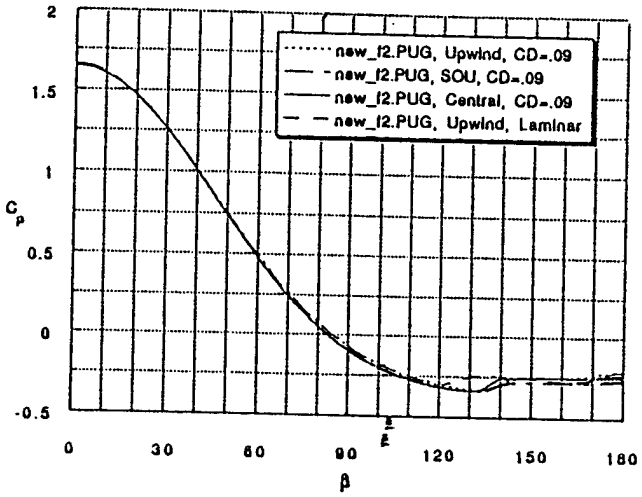

b.

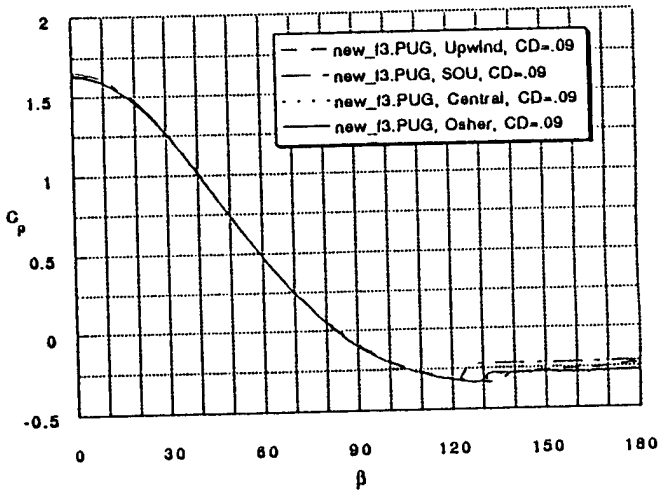

c.

Figure 3-10. Surface Pressure Comparison for Different Grids and Differencing Schemes Using the Standard Launder and Spaulding Turbulence Model for M = 2.0, Re = 8.27×10^6 Flow Over a Cylinder

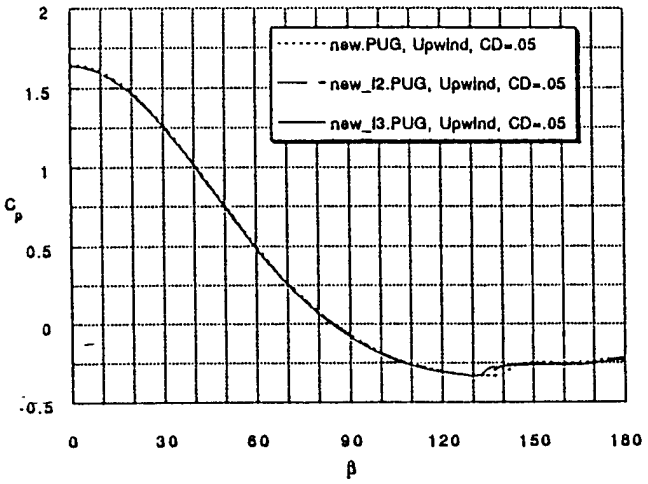

a.

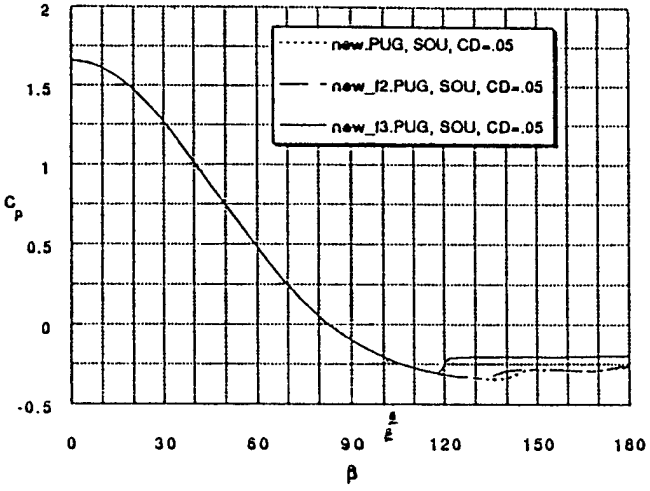

b.

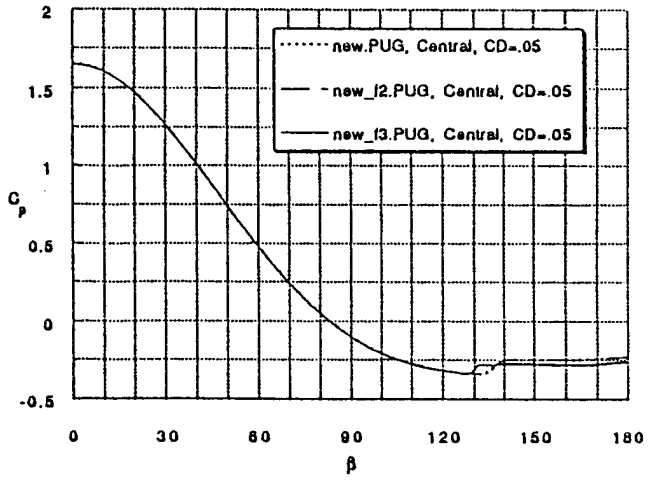

c.

Figure 3-11. Comparisons of Surface Pressures for Varying Grids and Differencing Schemes Using the Modified k-ε Model (CD = .05) for M = 2.0, Re = 8.27 x 10^6 Flow Over a Cylinder

3.2 Flow Over a Half Cylinder

In each of the cylinder cases, the proper location of the separation point was a determining factor in predicted drag, however, the separation point did not greatly effect the final base pressure value in the separated region. Since most of the separation in the ejection seat problem is due to separation from a sharp corner, a study of a half cylinder geometry was undertaken. Note that the definition for β is identical to the cylinder from 0 to 90 degrees, however, from 90 to 180 β is defined as:

$$\beta_i = 90° \left(\frac{r_i}{r_{max}} \right) + 90°$$

where r_{max} is the maximum cylinder radius and r_i is the distance from the r_{max} point at the i grid location. These variables are depicted in Figure 3-12a. Table 3-5 gives the grid parameters for the half cylinder cases with a sample grid, Grid_f6 in Figure 3-12b. Note that D_2 equals 2.099 cylinder diameters and the outer boundary was 55 times the cylinder diameter. In both cases, grid cells were clustered near the sharp corner of the half cylinder.

Table 3-5. Grid Parameters for the Half Cylinder Cases

Name	Size	D1
GRID_f6	88×131	2.621×10^{-5}
GRID_f8	198×131	2.621×10^{-5}

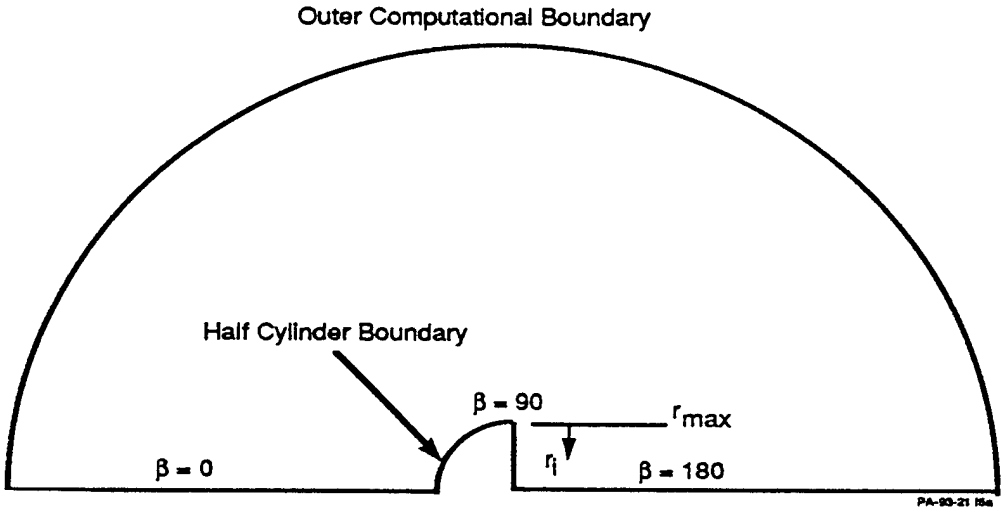

Figure 3-12a. Definition of the Angle β for the Half Cylinder Cases

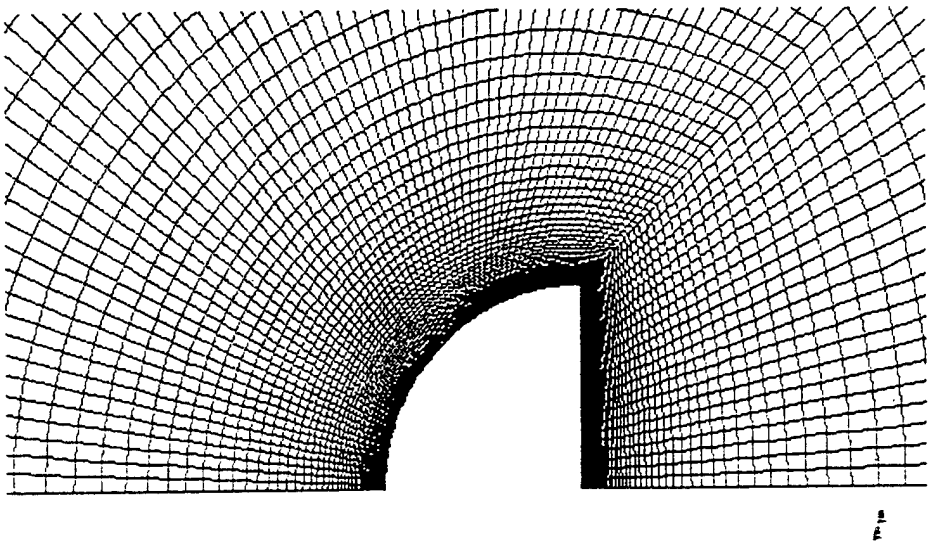

Figure 3-12b. Sample Half Cylinder Coarse Grid

Figures 3-13 through 3-15 show results for M=0.177, M=0.74 and M=2.0 for two different grids and varying differencing schemes using the standard k-ε turbulence model. For the subsonic case, the coarser grid (Figure 3-13a) shows strong oscillations in surface pressure at the corner (β=90) even though the results are well converged. The finer grid (Figure 3-13b) shows reduced oscillations; however, they are still present. In each case, Central differencing produces the smallest oscillations. As in the previous cylinder cases, the SOU and Central results are quite similar showing almost identical values of base pressure in the separated flow region. Even though separation is forced at 90 degrees the predicted base pressure value using the Upwind scheme is significantly less than the Central and SOU scheme predictions. A laminar (no turbulence model used) solution was also obtained for the coarser grid. Separation for the laminar case occurred before the sharp corner. A constant value of base pressure was not obtained in the separated region for the laminar case. The effect of modifying the k-ε turbulence model by reducing $C\mu$ was minimal in terms of base pressure prediction for the half cylinder.

Figure 3-14 shows transonic surface pressures for the half cylinder. As was the case in the full cylinder, the shock location and hence separation occurred before β=90 degrees. Thus, these results are quite similar to the full cylinder results. Lowering the value of $C\mu$ had similar effects as in the full cylinder cases.

Figure 3-15 shows supersonic surface pressures for the half cylinder. At this Mach number separation is again forced at 90 degrees. Note that as was the case in the full cylinder, using various differencing schemes had very minor effects on predicting the surface pressures. In addition the laminar results were almost identical to the turbulent results since separation location was not an issue.

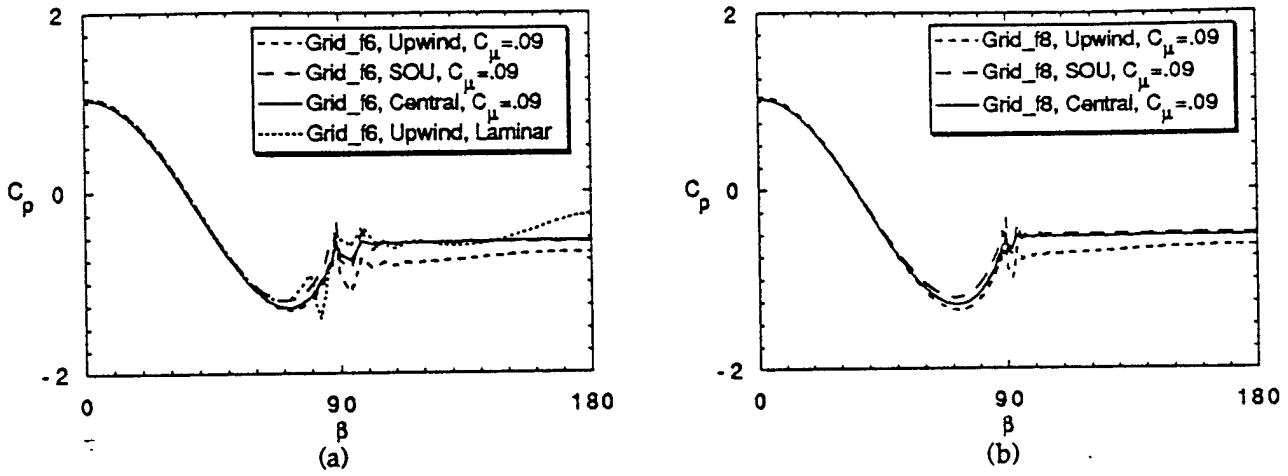

Figure 3-13. Half Cylinder Surface Pressures M = 0.177, Re = 8.27 x 10^6

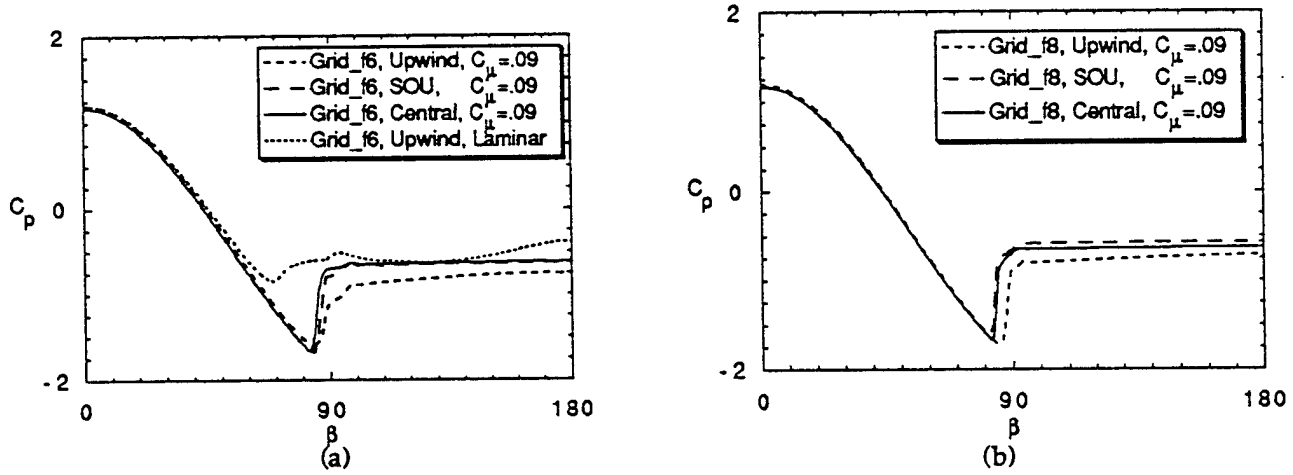

Figure 3-14. Half Cylinder Surface Pressures M = 0.74, Re = 8.27 x 10^6

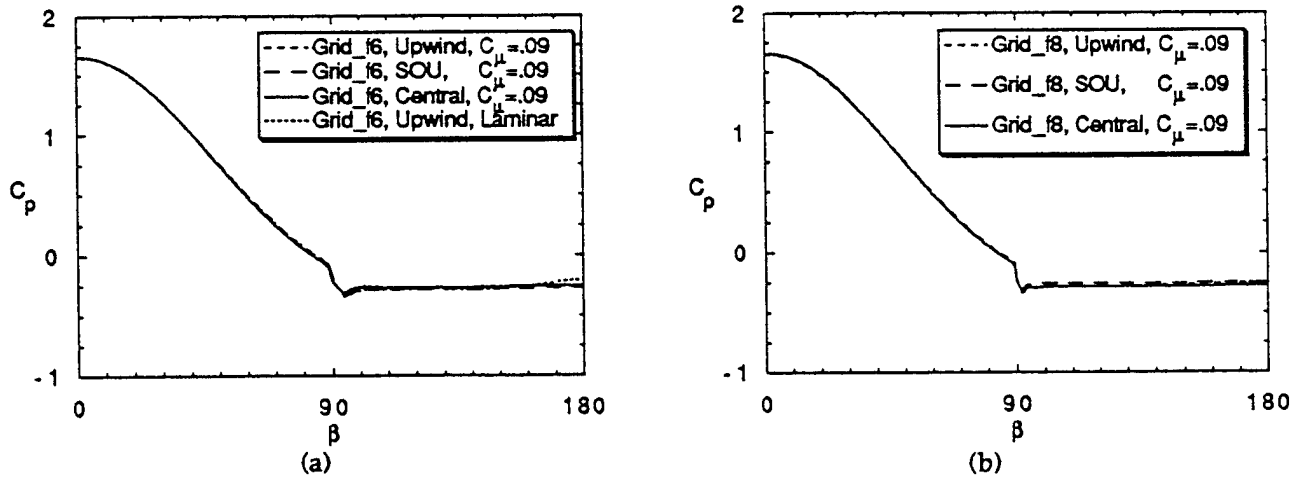

Figure 3-15. Half Cylinder Surface Pressures M = 2.0, Re= 8.27 x 10^6

Tables 3-6 through 3-8 show drag coefficients for each Mach number for various differencing schemes and grids. At M = 0.177, the finer grid always predicts lower drag due to a slightly larger base pressure beyond the cylinder. As witnessed by Figure 3-13, these differences are quite small; however, due to the larger surface area behind the half cylinder, they have a somewhat large impact on drag. At M = 0.74, a similar trend holds for the Upwind and SOU differencing results; however, the Central differencing results are much less grid sensitive. At M = 2.0, the differences in drag are very insensitive to changes in differencing scheme, grid, and turbulence model, as was the case in the full cylinder.

Table 3-6. Drag Coefficients for the Half Cylinder at M = 0.177, Re - 8.27×10^6

Case	C_D (upwind)	C_D (SOU)	C_D (central)	C_D (central $C\mu = 0.09$)
GRID_f6	.861	.678	.646	.604
GRID_F8	.761	.599	.602	.562

Table 3-7. Drag Coefficients for the Half Cylinder at M = 0.74, Re = 8.27×10^6

Case	C_D (upwind)	C_D (SOU)	C_D (central)	C_D (central $C\mu = 0.05$)
GRID_f6	1.192	.974	.962	.902
GRID_F8	1.104	.904	.965	.908

Table 3-8. Drag Coefficients for the Half Cylinder at M = 2.0, Re = 8.27×10^6

Case	C_D (upwind)	C_D (SOU)	C_D (central)	C_D (central $C\mu = 0.05$)
GRID_f6	1.408	1.418	1.399	1.387
GRID_F8	1.409	1.392	1.418	1.410

3.3 Flow Over a Sphere

All of the previous results and established trends have been for two dimensional simulations. Since the ejection seat is a three dimensional body, verification of these trends is necessary in 3-D. Thus, results for flow over a sphere at subsonic (M=0.1), transonic (M=0.955) and supersonic (M-2.0) Mach numbers were obtained. The subsonic Mach number value was changed for comparison to the experimental surface pressure and drag results of Achenbach [26] and the transonic Mach number was changed to compare to experimental results of Bailey, et al. [27,28] Experimental drag results for the supersonic case also exist in Bailey, et al. The Reynolds numbers based on sphere diameter for the subsonic, transonic, and supersonic cases were 5×10^6, 1×10^6, and 7×10^5, respectively. Table 3-9 shows the various grid sizes used for the sphere simulation. D_1 and D_2 are spacing parameters defined earlier for the cylinder. For the first four grids, the ratio of outer boundary to cylinder diameter is 10:1, while for grid sphere_f5, the ratio is 100:1. β is also defined the same as for the cylinder. For economic reasons, an axisymmetric version of the CFD-ACE code was used for these simulations.

Table3- 9. Grid Parameters for the Sphere Case

Name	Size	D1	D2
sphere	50×45	2.621×10^{-3}	.5242
sphere_f	50×45	2.621×10^{-4}	.5242
sphere_f2	50×45	2.621×10^{-5}	.5242
sphere_f4	150×90	2.621×10^{-5}	.5242
sphere_f5	150×90	2.621×10^{-5}	2.621

Figure 3-16 shows surface pressure results for the M=0.1 case for each grid using Central differencing and for each differencing scheme using the sphere_f4 grid. Note that the coarser grids (sphere, sphere_f) with values of y^+ of the first cell greater than 11.5 show similar results while the finer grids show earlier separation. This is the same trend noticed for the cylinder. However, the base pressure in the separated region is not constant as it was for the cylinder. The experimental results also do not show constant base pressure values, however, the variations are much less than in the computation. As in the cylinder case, the predicted base pressure values are always larger than those of the experiment. Also note that SOU and Central differencing results are quite similar while the Upwind differencing results show separation further downstream. However, none of the cases predicts separation as early as experiment. In an attempt to predict earlier separation and obtain better comparisons to experiment the value of $C\mu$ was lowered to 0.05 as in the cylinder simulations. Note in Figure 3-16b that indeed the separation was predicted earlier, however, the oscillations in base pressure were greater

for this case than the standard k-ε cases. In the cylinder cases, this detrimental effect in the fully separated region was not observed.

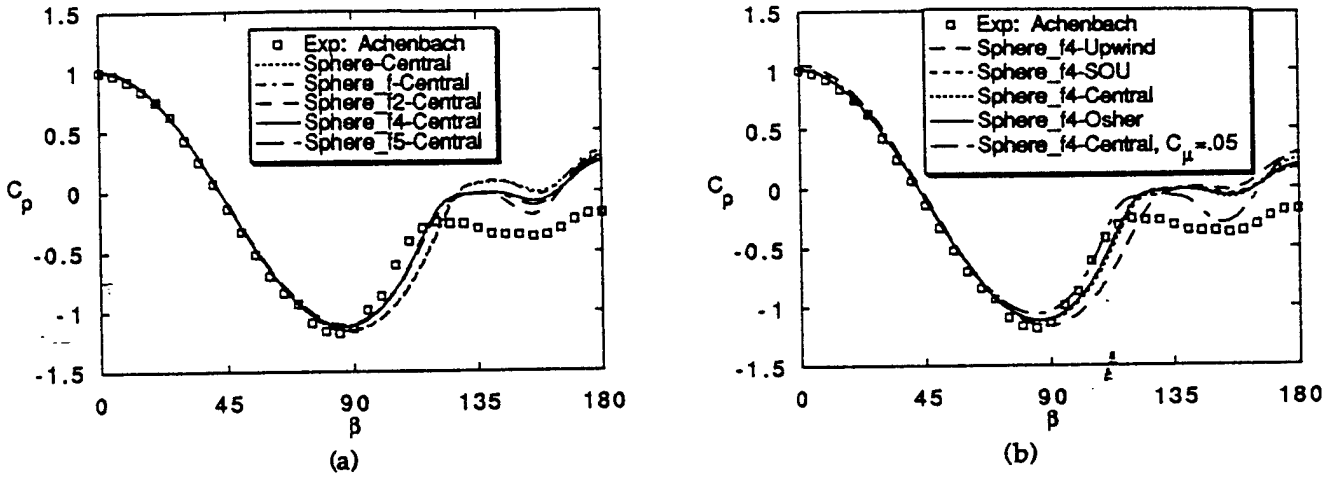

Figure 3-16. Sphere Surface Pressures at M = 0.1, Re = 5 x 10^6

Figure 3-17 shows transonic surface pressures for each grid using Central differencing and for each differencing scheme using the sphere_f4 grid. As was the case for the cylinder, the shock location determines separation. Figure 3-17a shows the sensitivity of shock location to streamwise grid refinement and the relative insensitivity to radial grid refinement. Figure 3-17b shows the sensitivity of shock location to differencing scheme. Note that the shock location for the sphere is more sensitive to differencing scheme than for the cylinder.

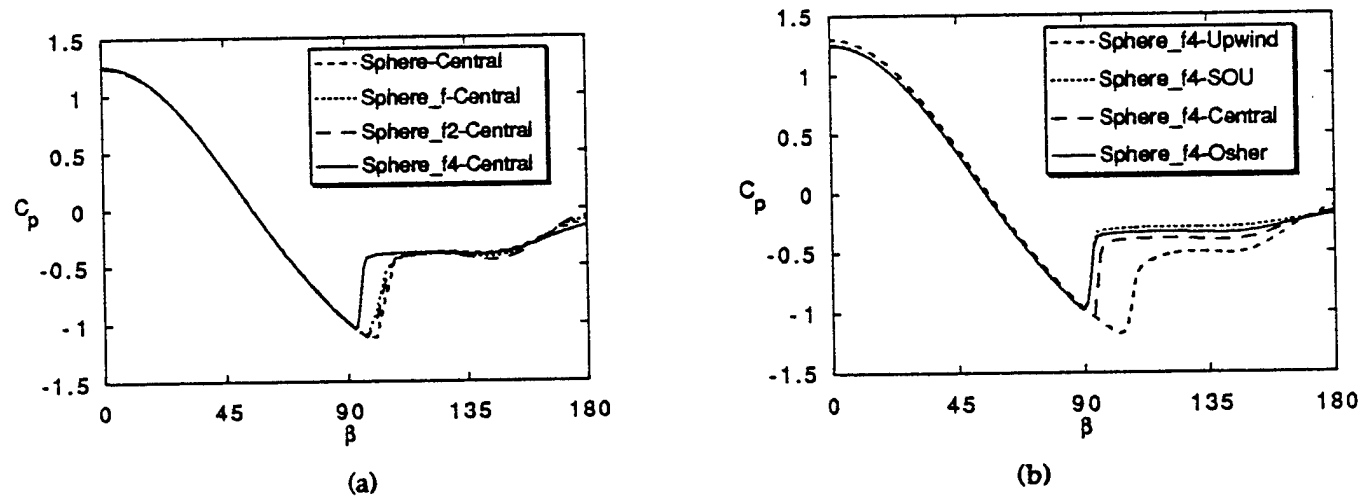

Figure 3-17. Sphere Surface Pressures at M = 0.955, Re = 1 x 10^6

Figure 3-18 shows supersonic surface pressures for each grid using Central differencing and for each differencing scheme using the sphere_f4 grid. As was the case for the cylinder, the differences between the various grids and differencing schemes were much smaller than the other Mach numbers.

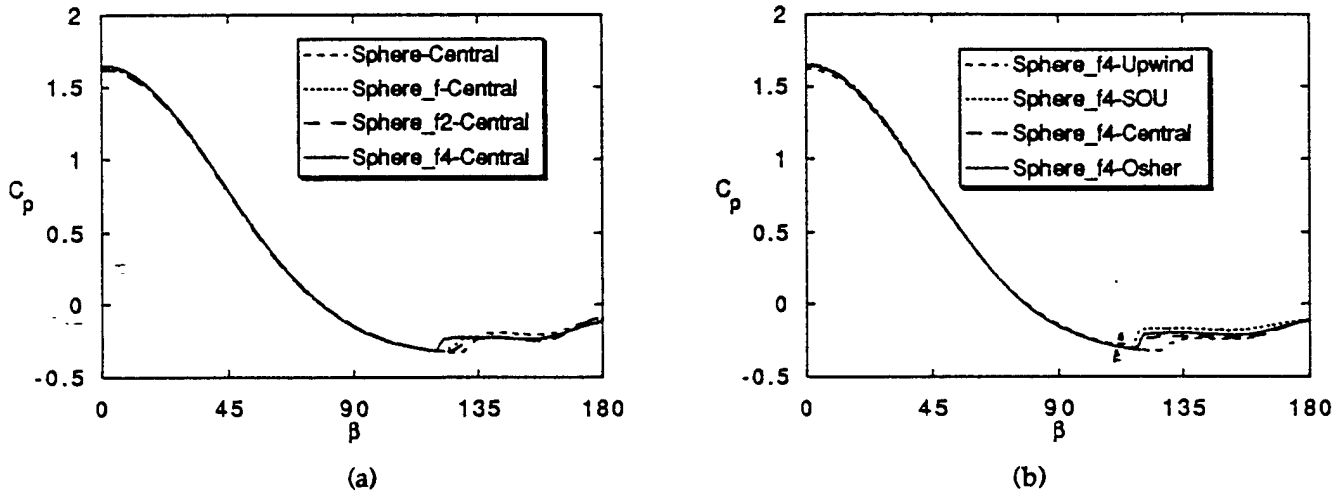

Figure 3-18. Sphere Surface Pressures at M = 2.0, Re = 7.0×10^5

Tables 3-10 through 3-12 show predicted drag values from the computations and the experiments reported by Achenbach and Bailey. For the subsonic case, note again that the Upwind results have better correlation to experiment even though the surface pressure comparisons are worse. On a percentage basis the differences between the computation and experiment for the sphere test cases are quite similar to the cylinder. The transonic comparison to experiment are better on a percentage basis than subsonic. Note that the upwind cases predict higher drag than experiment while the higher order schemes predict lower drag than experiment. The supersonic comparison to experiment is quite good for all test cases.

Table 3-10. Drag Coefficients for the Sphere at M = 0.1, Re = 5×10^6

Case	C_D (upwind)	C_D (SOU)	C_D (central)	C_D (Osher)
sphere	.220	.084	.089	.077
sphere_f	.239	.070	.091	.072
sphere_f2	.272	.096	.132	.108
sphere_f4	.153	.064	.086	.070
sphere_f5	.159	.061	.094	.074

Experiment (Achenbach): C_D = .242

Table 3-11. Drag Coefficients for the Sphere at M = 0.955, Re = 1×10^6

Case	C_D (upwind)	C_D (SOU)	C_D (central)	C_D (Osher)
sphere	.956	.725	.711	.690
sphere_f	.975	.671	.714	.668
sphere_f2	.995	.634	.727	.663
sphere_f4	.878	.586	.677	.620

Experiment (Bailey): C_D = .845

Table 3-12. Drag Coefficients for the Sphere at M = 2.0, Re = 7×10^5

Case	C_D (upwind)	C_D (SOU)	C_D (central)	C_D (Osher)
sphere	1.047	1.044	1.032	1.023
sphere_f	1.037	1.019	1.029	1.012
sphere_f2	1.029	.996	1.025	1.004
sphere_f4	1.036	.9867	1.027	1.004

Experiment (Bailey): C_D = 1.0

3.4 Conclusions from Assessment/Validation Study

Observations and conclusions from this numerical/physical modeling assessment and validation study on simpler geometries can be summarized as follow:

a. The supersonic test cases were much less dependent on turbulence modeling and differencing scheme for all cases. The comparison of predicted and experimental drag for the sphere shows all differencing schemes produce good drag prediction.

b. The subsonic cases were quite dependent on turbulence modeling and differencing scheme. For the cylinder and sphere, good pressure predictions were obtained before separation, however, near separation and in the separated region the pressures showed discrepancies with experiment. Due to extra numerical diffusion in the upwind scheme, separation was always predicted further downstream than the SOU, Central and Osher differencing schemes.

c. At transonic speeds, the shock location determines separation. Hence turbulence modeling and differencing scheme choice affect the results. However, the

resulting differences in drag coefficient are smaller in terms of percentages than the subsonic cases.

d. For the sharp corner separation of the half cylinder test case, the Upwind differencing scheme predicts lower base pressures than the higher order schemes, causing higher drag predictions.

4. CFD TOOLS VALIDATION AND DEMONSTRATION FOR ESCAPE SYSTEMS

The numerical schemes and physical modeling assessment calculations and validation efforts discussed in Section 3 established several guidelines for performing calculations of flows over blunt bodies. At the same time, these calculations validated the basic prediction capabilities of the computational tools. For more direct and relevant validation several efforts took place under this project to demonstrate and validate the tools directly on escape system configurations. The result of these efforts are presented in this section.

4.1 Ejection Seat and Occupant Validations

For more direct validation of the developed computational tools, two separate efforts were conducted. These include:

- NACES seat validations
- ACES-II seat validation

These two efforts are discussed separately below.

4.1.1 NACES Seat

For validating the developed computational tools against ejection seat and occupant configurations, several studies have been performed on the NACES seat. The NACES seat geometry and grid generation procedure was discussed in section 2. The geometry and grid model were used to develop an initial aerodynamic database for the NACES seat. Most of these calculations took place under a separate Navy contract (contract number N62269-92-C-0248) on the NACES seat. Besides developing an aerodynamic database for the NACES seat, work was performed under this contract on the stabilization fins and the Pitot tubes of the seat. The findings from this study are exclusively documented in a AIAA technical paper (AIAA-94-0395) entitled "Computational Aerodynamic Characteristics of the Navy Aircrew Common Ejection Seat" and in a project final report (CFDRC project report 4260/4). The technical paper is included in Appendix A for complete reference.

NACES calculations were performed for several free stream Mach numbers (M=0.75, 1.2, 1.5 and 2.0) and several seat/occupant pitch(alfa=-20, -10, 0, 15, 30, 45 and 60) and yaw (beta=0, 15, and 30) orientations.

Since wind tunnel test data were not available for the NACES seat at that time, direct comparisons could not be made. However, since ejection seats in general have similar aerodynamic characteristics, the NACES CFD predictions were compared to existing test data of 3 other seats including F-106, ACES-II and CREST seats. The comparisons showed excellent agreement in overall trends of the data. NACES aerodynamic coefficients were within 20 percent of most of the test data. Sample results are shown in Figures 4-1 and 4-2. These comparisons provided good levels of confidence in the

computational tools and their prediction accuracy.

4.1.2 ACES-II Seat

For more direct validation, calculations were performed under this contract on the ACES-II ejection seat and generic occupant. Wind tunnel test data was available for the ACES-II seat and were compared to the CFD predictions.

The geometry of the ACES-II seat was supplied by the Navy technical monitor via an IGES formatted file. This file was ported to the ICEM-CFD code where a CAD wireframe was created for CFD modeling purposes. Since the IGES file did not include an occupant, the NACES occupant was extracted and superimposed on the ACES-II seat. Some minor modifications were made to the occupant to look more like the ACES-II wind tunnel occupant based on visual examination of the ACES-II wind tunnel pictures and plots. These modifications include positioning of the arms and legs.

Figures 4-3 and 4-4 show the shaded surface and surface mesh of the modeled ACES-II seat and occupant along with those of the NACES seat for comparison purposes. Note that since the occupant is of arbitrary size and does not exactly represent the wind tunnel model, only qualitative and not exact comparisons will be made with wind tunnel test data. The ACES-II geometry model has been transformed to CFD-GEOM and the same geometry and grid can be produced currently with CFD-GEOM.

An elliptic computational grid for the installed orientation ($a = 17$, $ß = 0$) was obtained with the elliptic grid generator. A grid size comparable to the NACES grid size was used (78x83x33 for the symmetry calculations). Figure 4-5 shows the computational grid at the symmetry plane.

CFD simulations were performed for free stream Mach numbers of 0.6 and 1.4 at wind tunnel conditions for various pitch (α = -20, -10, 0, 15, 30, 45, and 60 degrees) and yaw (Beta=0, 10, 20, 30 and 40 degrees).

During the geometry and grid creation procedure, there were some uncertainties about the representation of the occupant size (especially the head area) and the ACES-II seat bucket frontal area. Therefore, a sensitivity study was performed on the seat bucket shape to observe the effects on the aerodynamic coefficient. Also, the CFD computed results were compared to wind tunnel test data of two different neck and head shapes (long neck and short neck) to assess and quantify the effects of the occupant head sizes with respect to CFD computations.

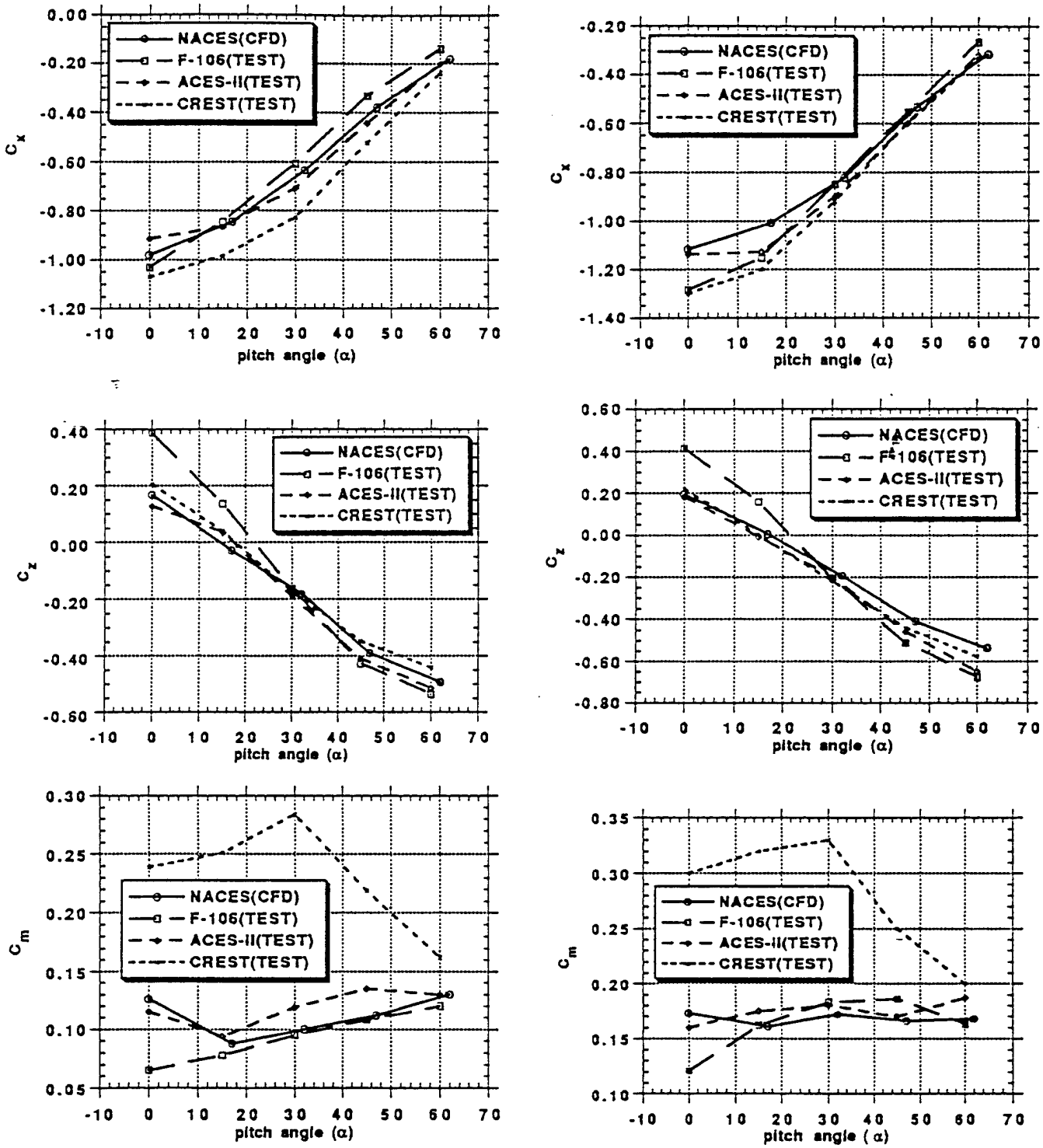

Figure 4-1. Predicted and Measured Aerodynamic Coefficients with Varying Yaw Angles for Various Seats

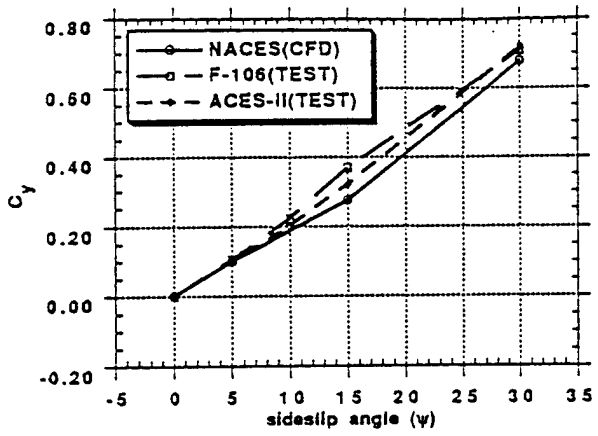

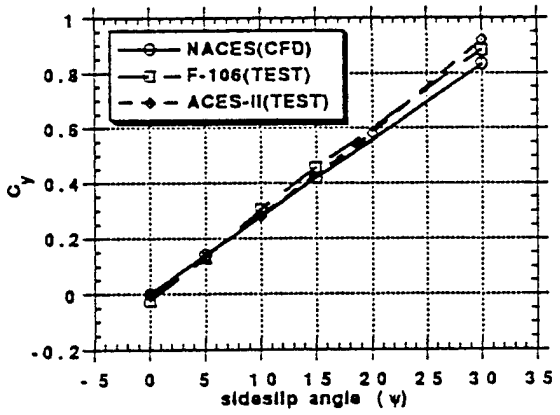

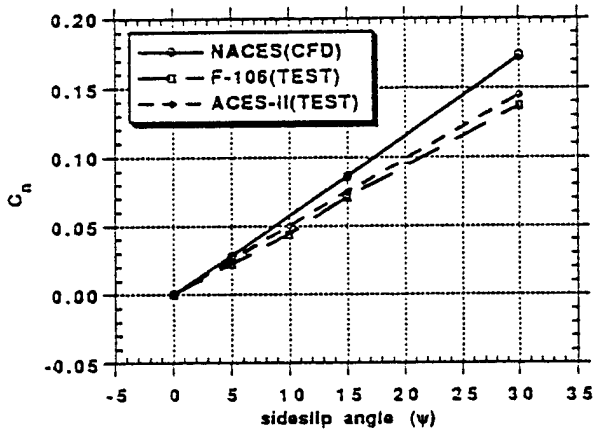

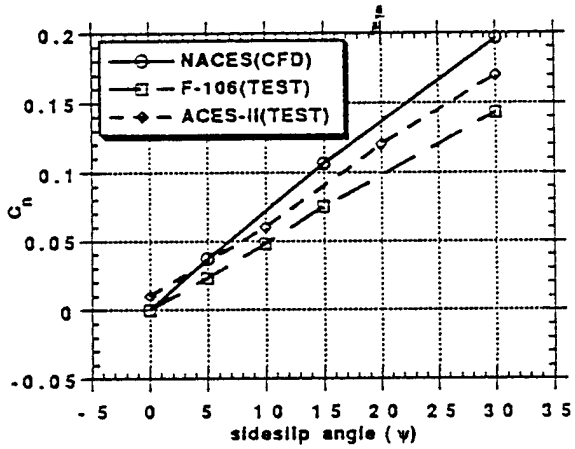

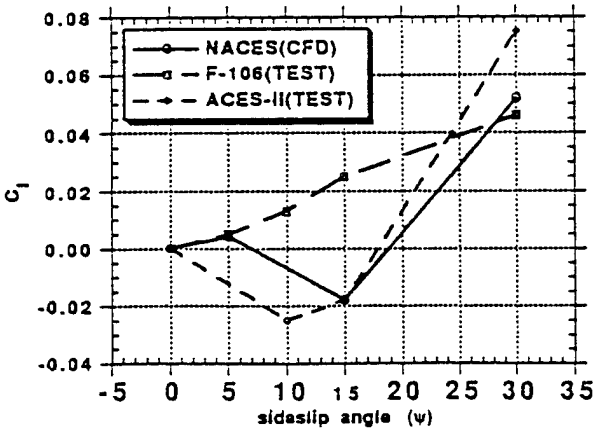

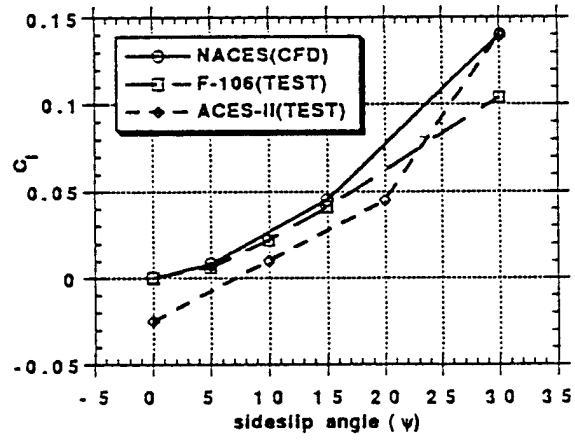

408 KEAS (M = 0.74)

700 KEAS (M = 1.18)

Figure 4-2. Predicted and Measured Longitudinal Aerodynamic Characteristics for Various Seats; M = 0.75

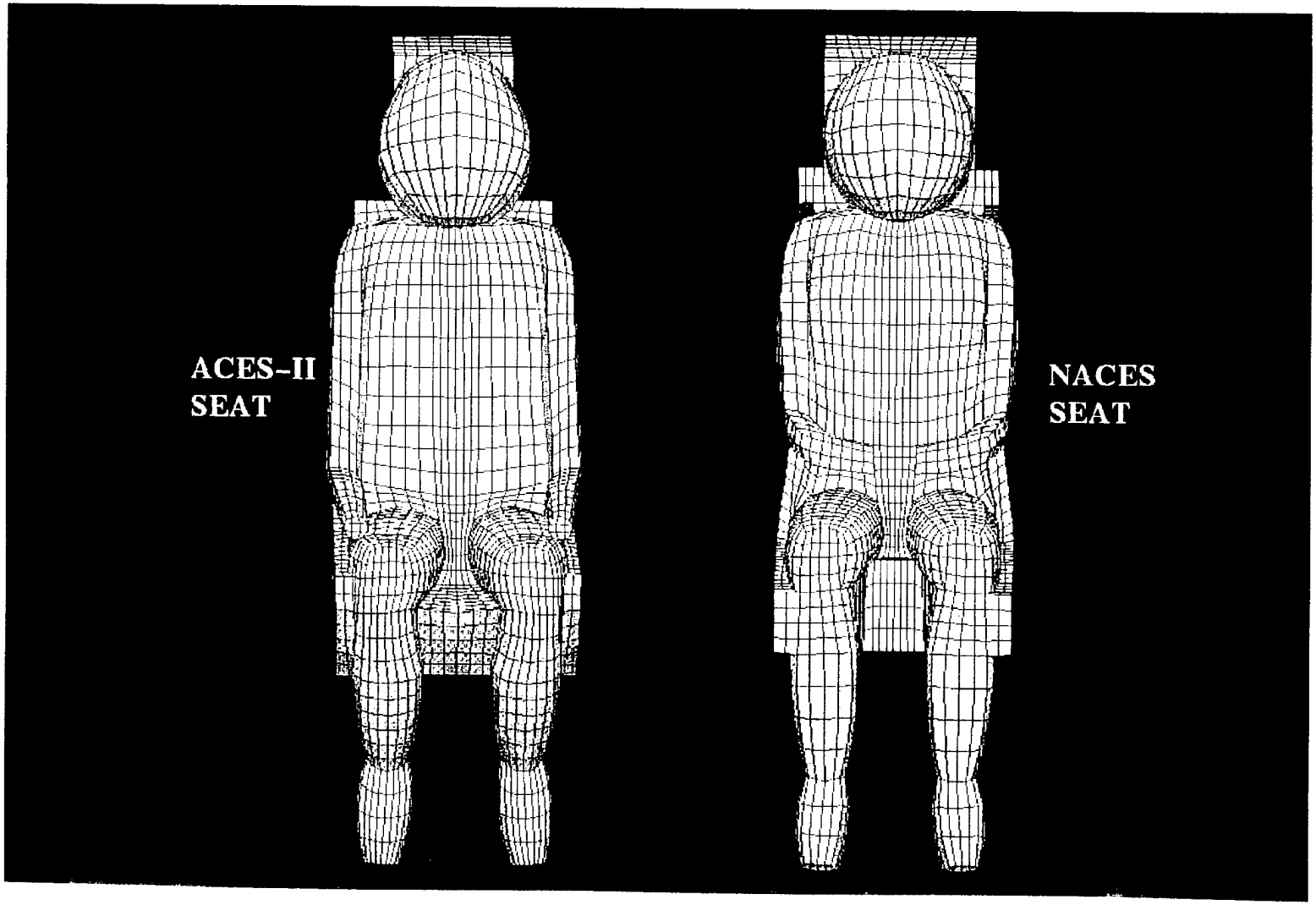

Figure 4-3. Shaded Surface and Surface Mesh of the ACES-II and NACES Seats with Occupant; Front View

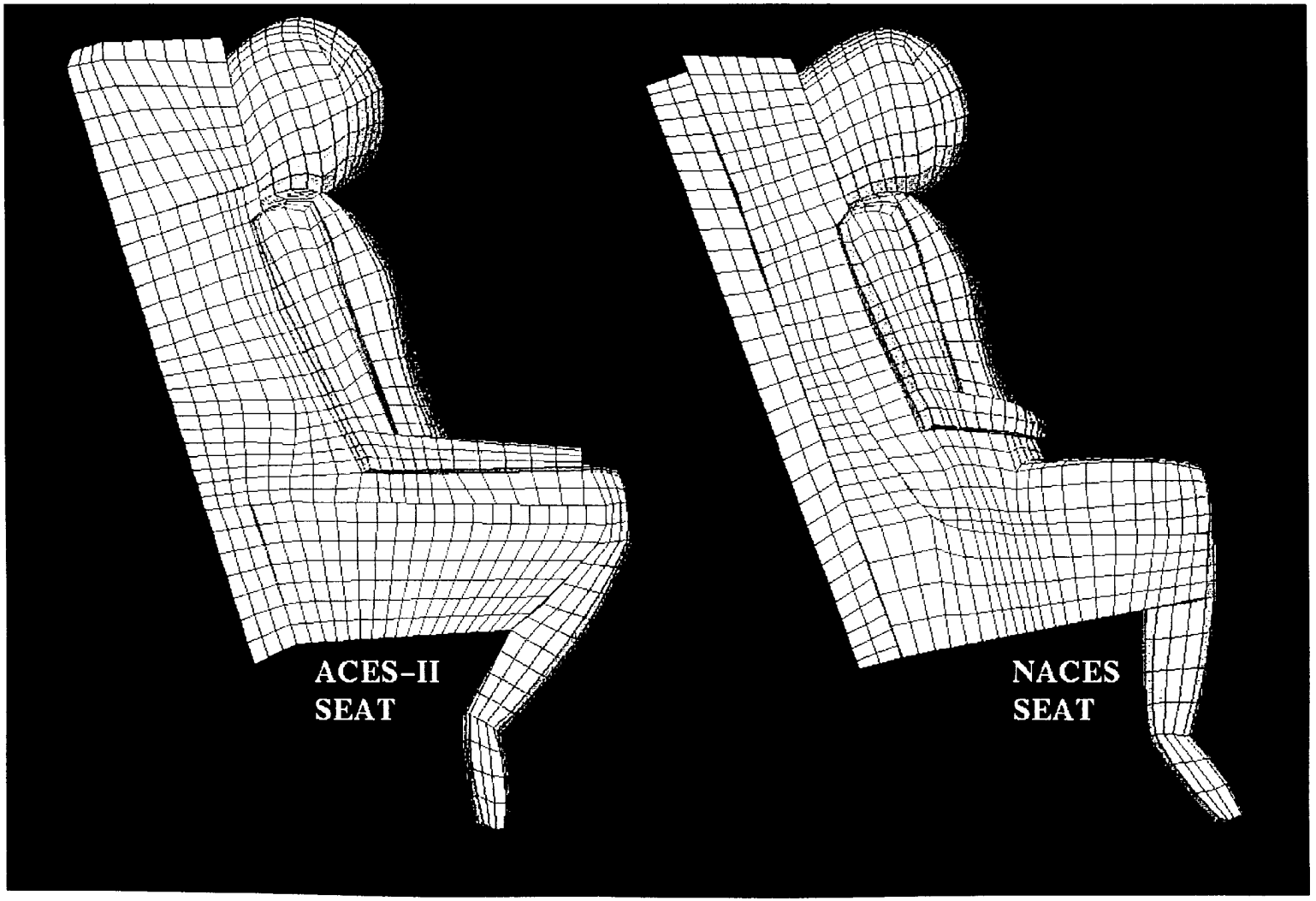

Figure 4-4. Shaded Surface and Surface Mesh for the ACES-II and NACES Seats with Occupant; Side View

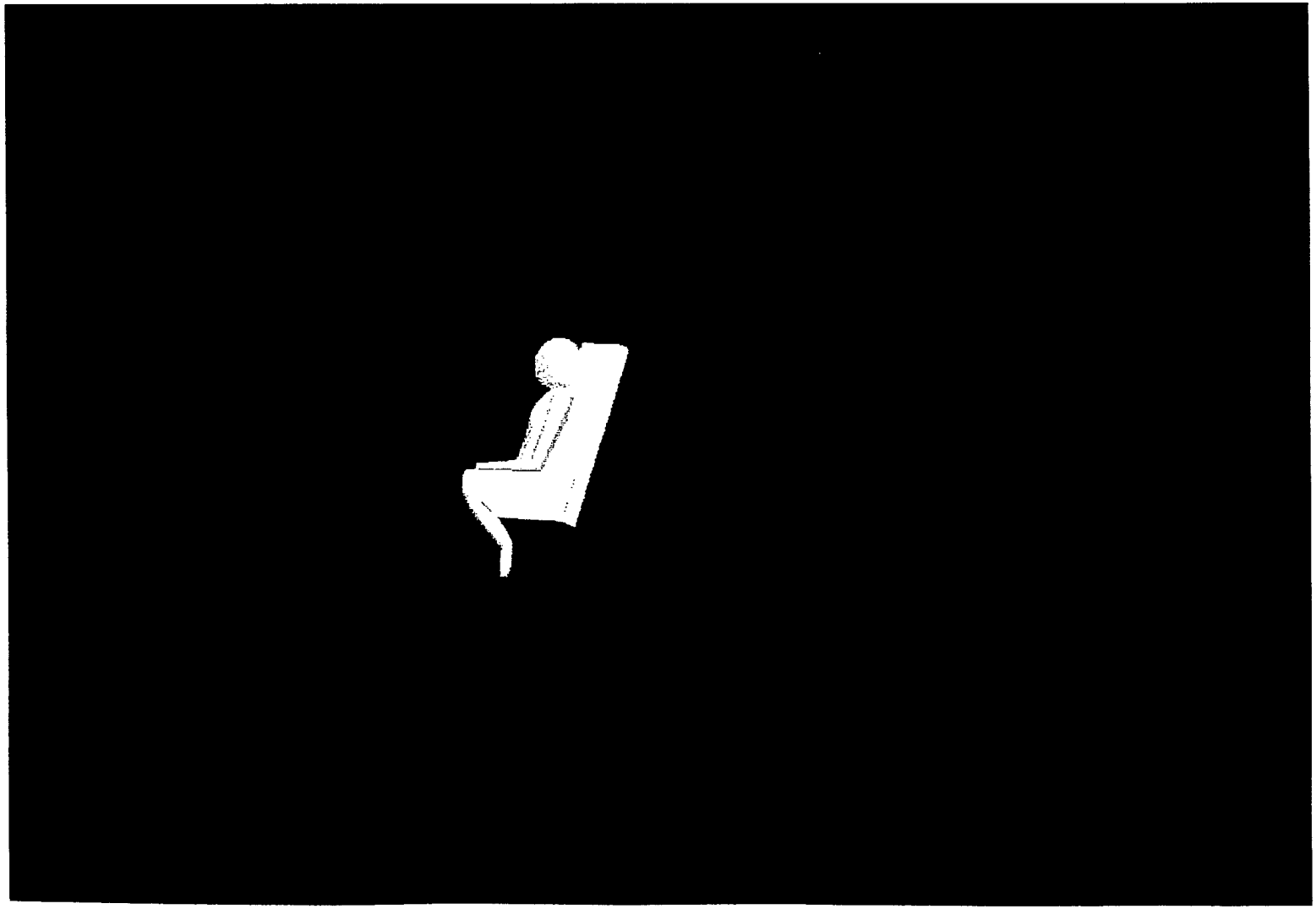

Figure 4-5. Computational Grid at the Symmetry Plane for the ACES-II Seat/Occupant

Figure 4-6 presents the predicted CFD force and moment coefficients as compared to the wind tunnel test data for both the short neck (SN) and long neck (LN) occupants at M = 0.6. Note that GRID4 for which the results are shown in Figure 4-6 was chosen out of four grids to be the most representative of the ACES-II geometry (more discussion about the various grids is presented later in this section). Overall, both the force coefficient Cx and Cz compared very well to the test data throughout the pitching envelope. The axial force coefficient compares better with the data of the long neck occupant, while the normal force coefficient seems to be insensitive to the head and neck sizes. The predicted moment coefficients shows much more discrepancy with the test data than the force coefficients. The trends compare well to test data up to the pitching angle of 30 degrees. At 45 and 60 degrees, the trend of the pitching moment changes drastically from that of the wind tunnel data. The reason for this discrepancy was puzzling. Since the force coefficients compared well it was conceived that the discrepancy could be due to the location of the SRP. However, a sensitivity study was conducted (by changing the location of the SRP) and the wind tunnel trends could not be repeated.

Figure 4-7 presents the results of the M = 1.4 simulations (note that the wind tunnel short neck results were not documented). Once again, the force coefficients compare very well to the test data for all pitch orientations. The trends of the pitching moment coefficient are very similar to that of the test data, however, the magnitude of the predicted pitching moment is much higher than that of the test data (20-30%).

The reason for this discrepancy in pitching moment predictions may be due to the following:

- location of Seat Reference Point;
- misrepresentation of the occupant size especially head and lower legs; and
- differences in projected frontal area (CFD computed frontal area is 6.7 compared to wind tunnel 7.5 ft2).

Figures 4-8 and 4-9 show the shaded surface and computational grid for the four modeled seat bucket frontal surfaces. Note that these changes were made to observe what effects such small changes would have on the seat aerodynamic performance. The first grid (GRID1) represents the largest seating area while the second grid (GRID2) represents the smallest seating area where the area between the legs was eliminated. Figure 4-10 shows the results of the four grids compared to wind tunnel test data of the long neck occupant. The following observations may be made about this figure:

a. The axial force coefficient seems to be a function of the inclination angle of the frontal seat bucket surface. The highest Cx is obtained at the zero inclination angle of GRID4 and GRID2 while the lowest Cx is obtained for the largest inclination angle of GRID1.

b. The normal force coefficient (Cz), at the lower pitching angles ($\alpha \leq 0$), seems to be a function of the size of the upper surface of the seat area as expected. The largest Cz is obtained for the largest area of GRID1 while the smallest Cz is obtained for the smallest area of GRID2 and GRID4.

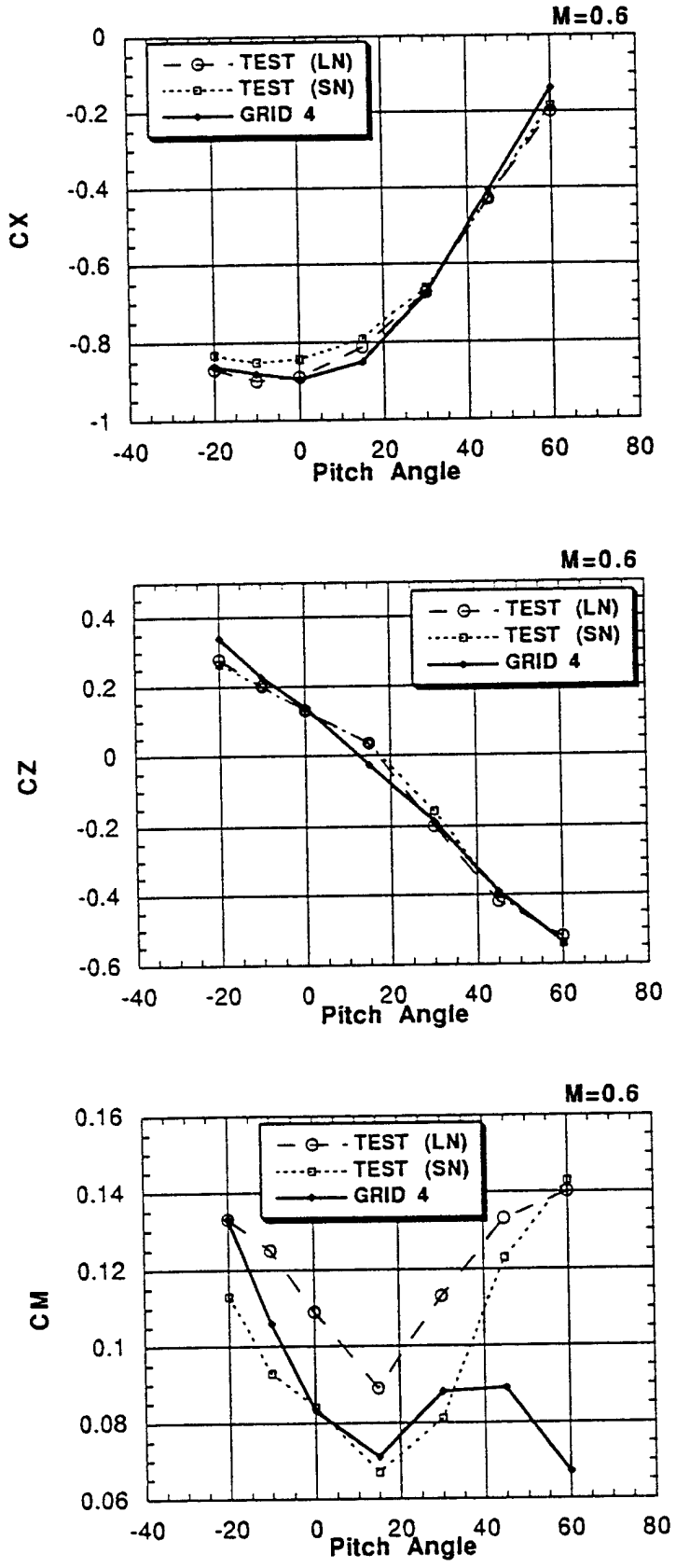

Figure 4-6. Predicted and Measured Force and Moment Coefficients for the ACES-II Seat vs. Pitching Angle; M = 0.6

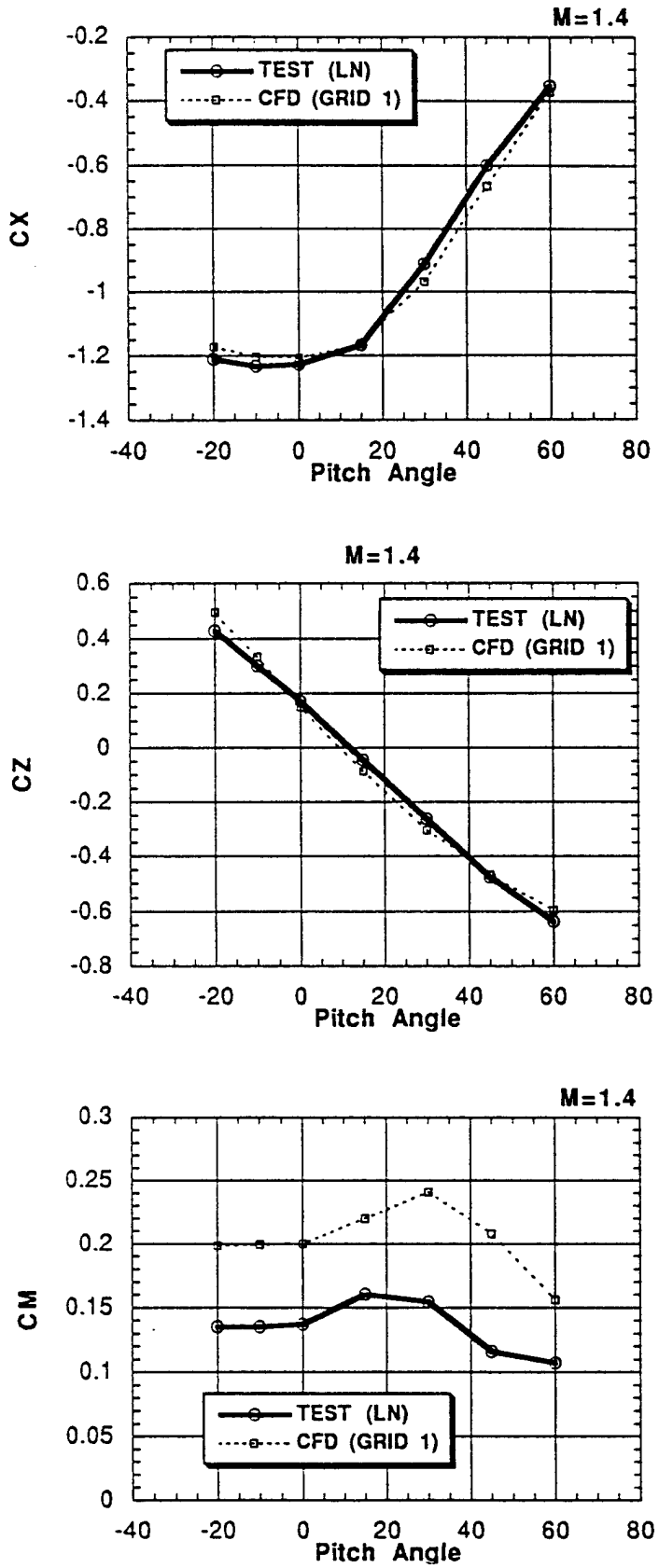

Figure 4-7. Predicted and Measured Force and Moment Coefficients for the ACES-II Seat vs. Pitching Angle; M = 1.4

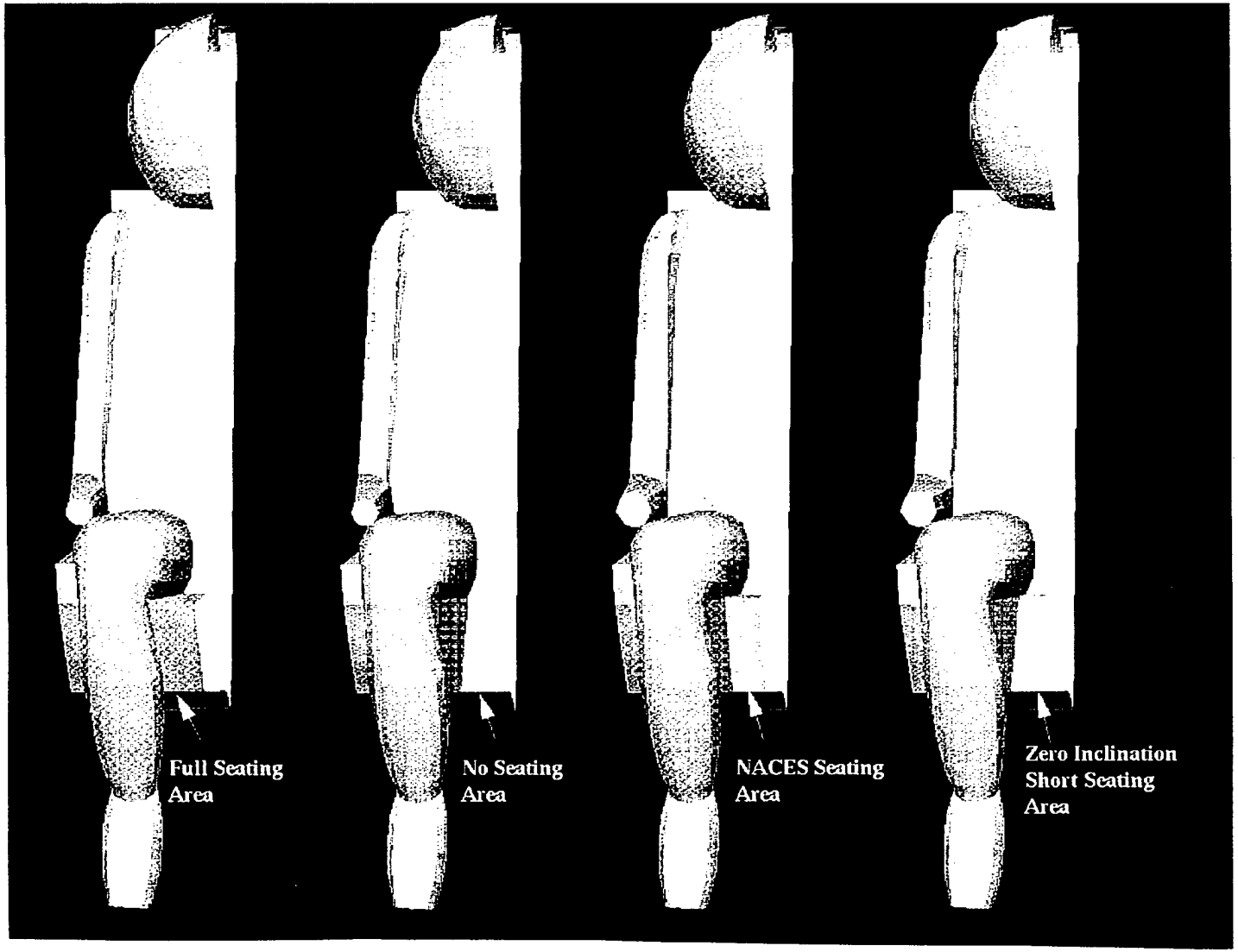

Figure 4-8. Shaded Surface of the ACES-II Seat with Four Different Modeled Seat Bucket Frontal Area

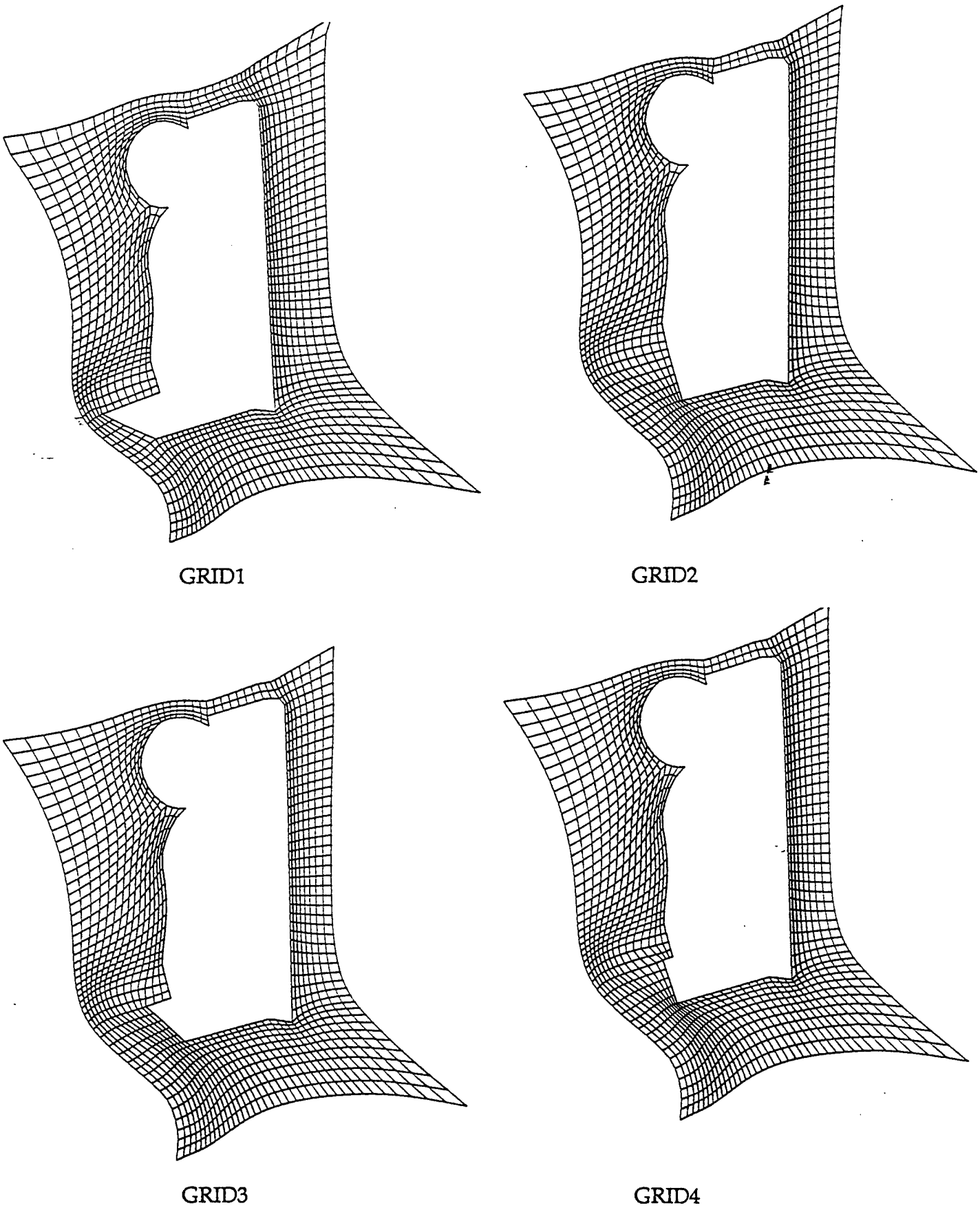

Figure 4-9. Computational Grid at the Symmetry Plane Showing Different Modeled Shapes of the ACES-II Seat Bucket

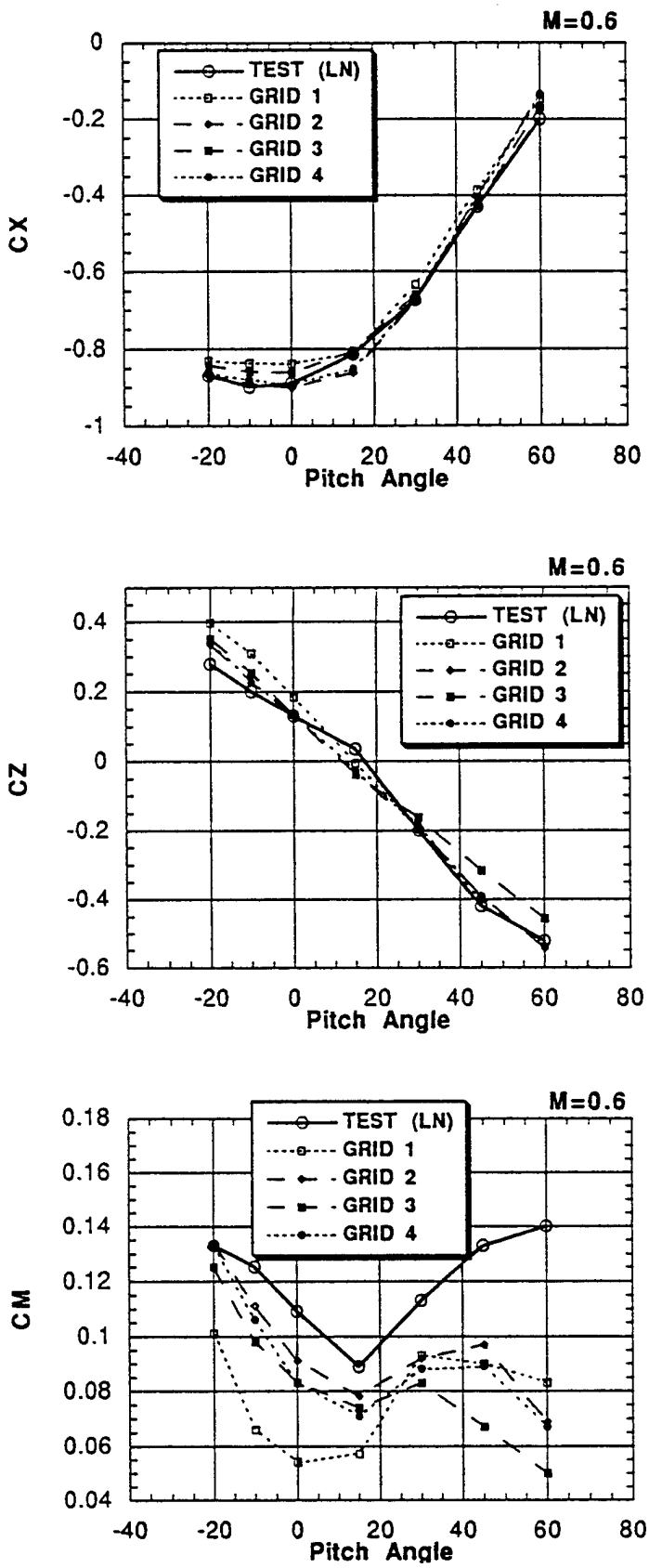

Figure 4-10. Predicted Force and Moment Coefficients for Several Seat Bucket Shapes vs. Pitching Angle; M = 0.6

c. The pitching moment coefficient sensitivity to the changes in the seat bucket frontal area is striking. Although the trends remain similar, the magnitude changes drastically from one shape to the other. The magnitude of the moment coefficient seems to be a function of the size of the upper seating area as expected. The larger the area the more the downward force which reduces the pitching moment.

The sensitivity of the pitching moment to such small changes in the geometry may explain some of the discrepancies between the overall predicted and measured pitching moment. However, the trends at the higher pitching angles are still puzzling and could not be explained.

To validate the tools for prediction of the lateral aerodynamic characteristics, several yaw orientations were simulated at free stream Mach number of 0.6. The grid adjustment model (discussed in section 2.4.3), was used to orient the baseline grid for the various yaw orientations considered for this effort. Figure 4-11 shows the grid in a computational plane above the legs of the occupant for the baseline orientation and selected other yaw orientations. Results were obtained for yaw orientations of 0, -10, -20, -30, and -40 degrees. Figure 4-12 shows the side force coefficient (Cy) along with the yawing (Cn) and rolling (Cl) moment coefficients from this study compared to wind tunnel test data [29] of the ACES-II seat. Cy and Cn compared fairly well to test data. The percentage of error ranges from less than 5 percent for yaw angles of -10 degrees to about 22 percent for yaw angles of -40 degrees. It is observed that as the yaw angle increases, the agreement gets worse. This could be due to a combination of two reasons. The first may be due to differences in the side geometry that play a bigger role as the yaw angle increases and the pressure on the side becomes larger, therefore affecting the force and moment coefficients. The second more probable reason may be due to numerical and turbulence modeling, for as the yaw increases, the wake and separation zone become larger therefore resulting in expected larger numerical errors due to turbulence modeling. The Cl moment coefficient compares much worse than the other two coefficients and as observed above, the agreement gets worse as the yaw angle increases.

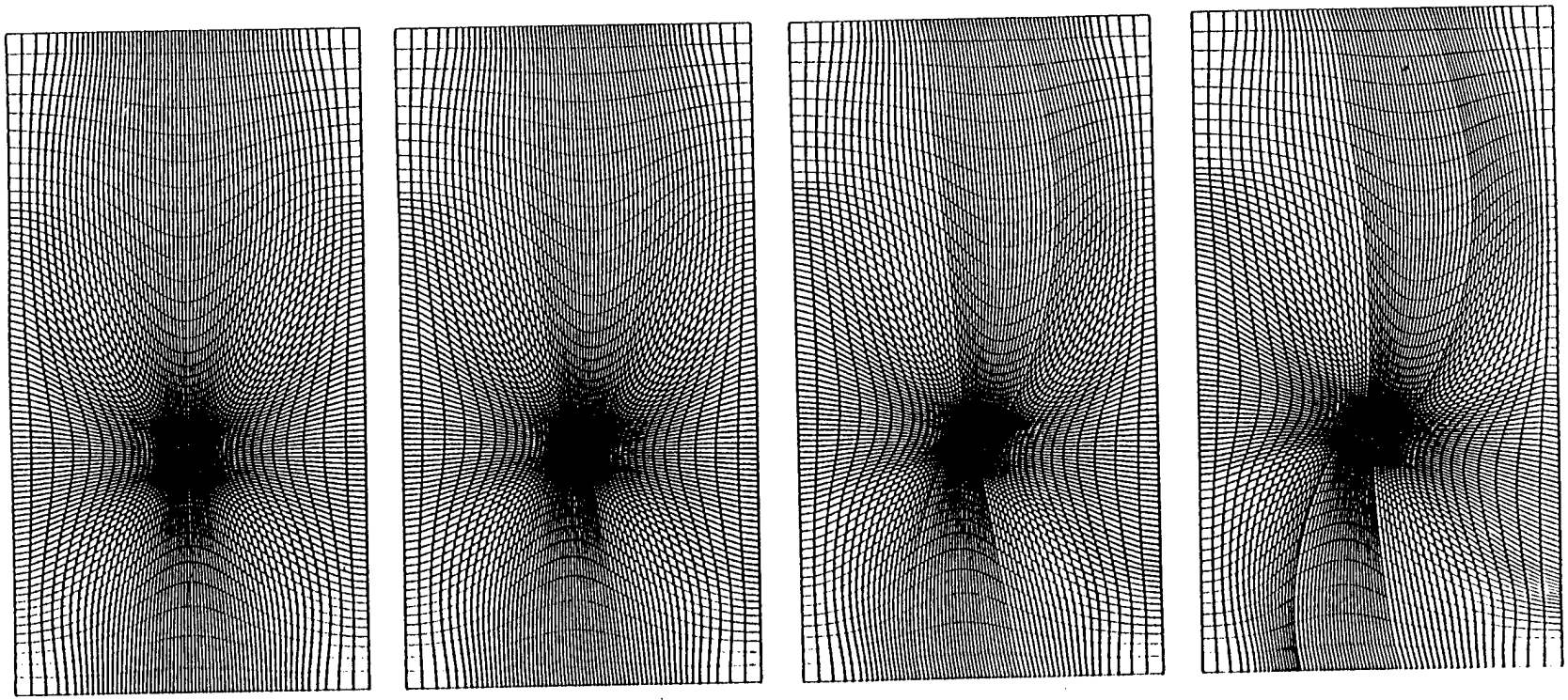

Figure 4-11. Computational Grid in the XZ Plane for Several Yaw Orientations

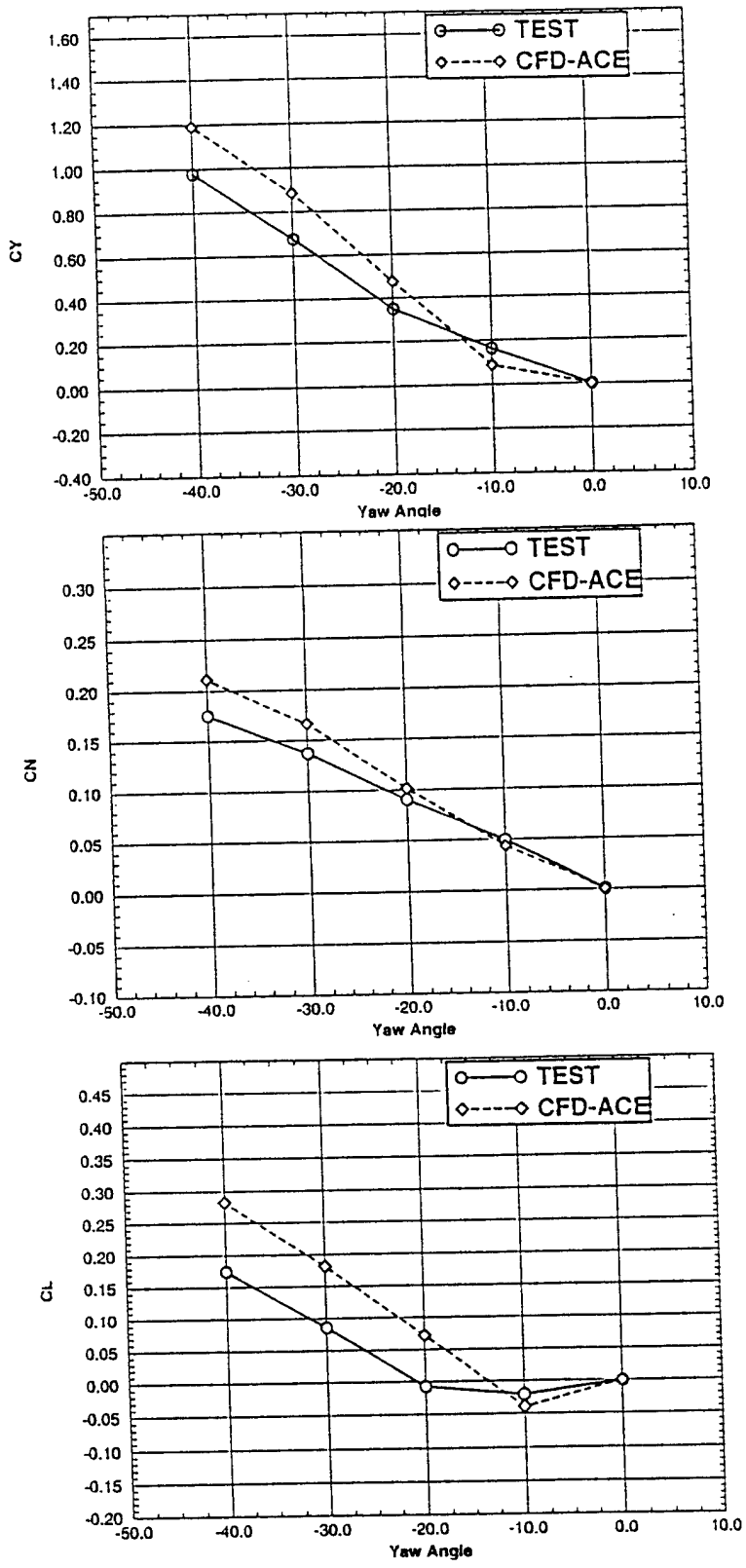

Figure 4-12. Predicted and Measured Force and Moment Coefficients for the ACES-II eat vs. Yaw Angles; M = 0.6

4.2 B-1A Escape Capsule Demonstration and Validation

The B-1A escape capsule, Figure 4-13, was developed in the early 1970's but was never selected for use in the final production B-1B aircraft. However, a significant amount of wind tunnel testing was conducted on small scale models including a 0.036 model [30] at several Mach numbers including 0.3, 0.95 and 2.2. The B-1A escape capsule geometry was chosen for further demonstration and validation of the developed/adapted computational tools for ejection seat and occupant analysis due to the availability of its wind tunnel data.

The B-1A escape capsule has a blunt body with a flat bottom and flat rear with vast separation and recirculation zones. It has already been analyzed using panel methods and using the Euler MERCURY code. It was concluded from the Euler analysis that a Navier-Stokes solution is required due to the dominance of the viscous effects [31]. The present simulations were conducted using the k-e turbulence model and several high order differencing schemes (consistent with the recommendations made in section 2.2). Due to questions regarding the upper surface of the escape capsule, two escape capsule models were analyzed. The results are compared to wind tunnel test data and Euler method results that were obtained using the MERCURY code.

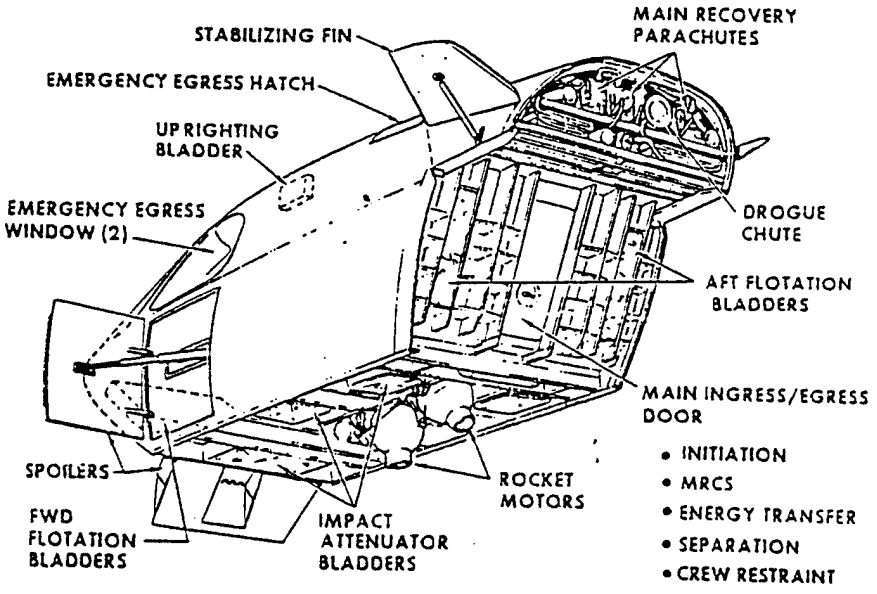

Figure 4-13. B-1A Escape Capsule

Geometry Modeling and Grid Generation Questions regarding the upper surface definition of the B-1A escape capsule required that two separate (but similar) capsule geometries be analyzed. The effects of the differing escape capsule models on the resulting surface pressure and aerodynamic force and moment coefficients are quite

interesting. These results are presented and discussed in later sections.

The first escape capsule model analyzed is the same representation used in previous Euler computations [31]. This representation was obtained in the form of IGES curves and a structured Plot-3D surface grid shown in Figure 4-14. Note that the IGES curves are selected lines in the Plot-3D grid. B-spline surfaces were obtained using the ICEM-CFD grid generation environment by interpolating between the IGES curves. With this surface, a computational surface grid of arbitrary resolution can be constructed. Comparisons between the modeled upper surface of the escape capsule with pictures from the experimental results raised questions about the integrity of the CFD surface model. This led to the use of an alternate upper surface representation obtained from a structured Plot-3D grid of the B-1A aircraft shown in Figure 4-15. The alternate representation was obtained by overlaying the aircraft Plot-3D grid with a Plot-3D grid of the first escape capsule model to locate the relevant portion of the aircraft geometry for the escape capsule as shown in Figure 4-16. CFD-GEOM was used to extract the aircraft geometry from the Plot-3D grid and merge it with the first escape capsule model. The difference between the two models is limited to the upper surface differences. Figure 4-17 shows representations of the first and second capsule models together. Note that the second capsule model is slightly below the first capsule model and the surface curvature is different, especially just aft of the nose. The Model 2 surface representation was used for all the results presented in the next section. Selected results from the Model 1 surface (the surface analyzed with the MERCURY code) are presented to illustrate the error introduced by the erroneous surface geometry.

The computational structured grid surrounding the capsule was created using the elliptic grid generator. Several grid sizes were used to determine the sensitivity of results to grid resolution and to obtain grid independent results. Figure 4-18 shows the selected computational grid at the symmetry plane in the immediate surroundings of the capsule using the Model 2 geometry.

Computational Results and Validations Computations were performed for free stream Mach numbers of 0.3, 0.95, and 2.2 at wind tunnel conditions. Several angles of attack were considered including α = -30, -15, 0, 15, and 30 degrees.

Results of M=0.3 calculations will be first presented and compared to wind tunnel test data and MERCURY code results. They will be followed by results from M=0.95 and M=2.2 calculations which will also be compared to wind tunnel test data. Note that MERCURY code results were only available at M=0.3.

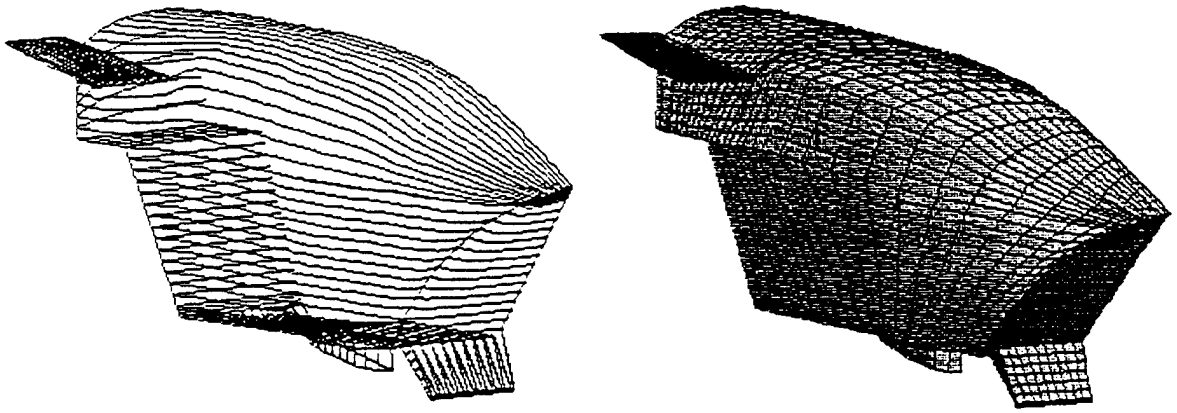

Figure 4-14. B1-A Escape Capsule, Model 1; Left: IGES Curves; Right: PLOT3D

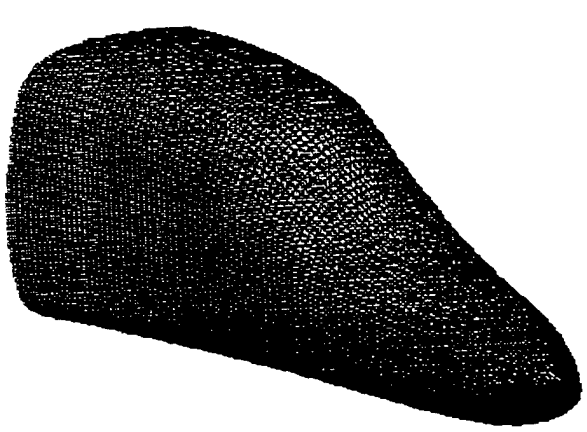

Figure 4-15. External Surface Representation of B1-A Aircraft Nose

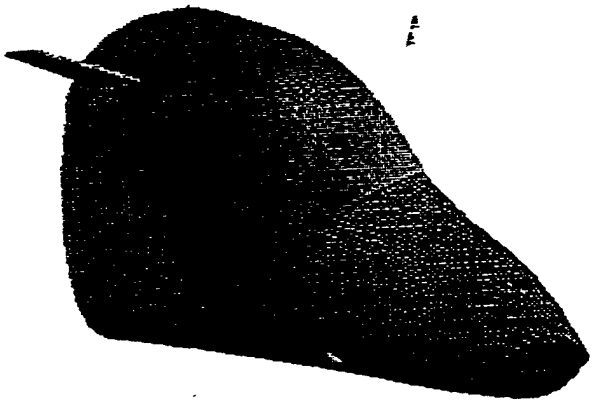

Figure 4-16. Overlay of B1-A Aircraft with Model 1 Escape Capsule

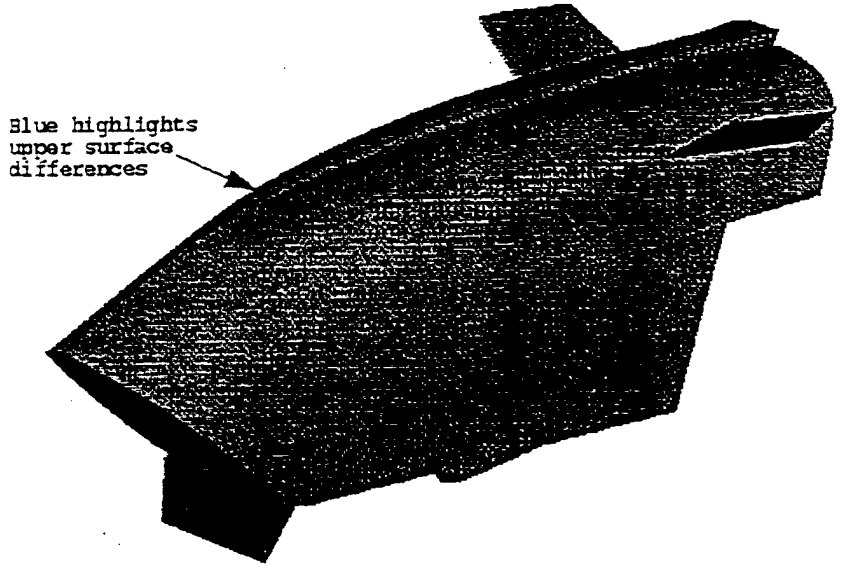

Figure 4-17. Comparison between the Two Surface Models of the Escape Capsule. Left: Model 1, Right: Model 2 (from aircraft surface)

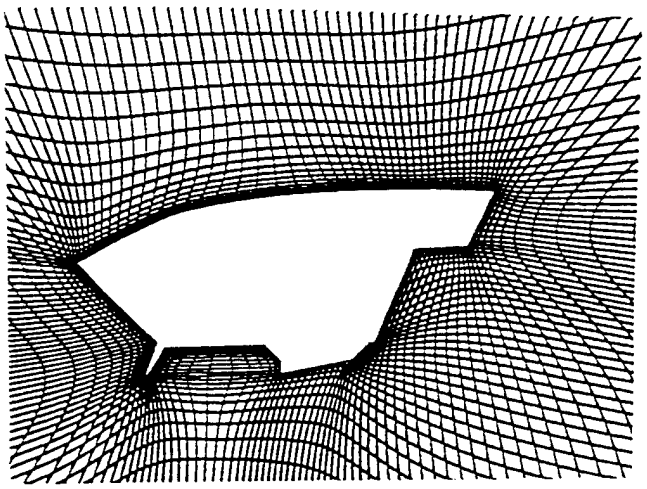

Figure 4-18. Computational Grid at the Centerline of the Capsule

Figure 4-19 presents the force and moment coefficients from the M=0.3 present calculations (using Model 1 and Model 2 geometries) along with the wind tunnel test data and those of the MERCURY code. Overall, the results of the present study compare well with test data, and much better than those of the MERCURY code, especially for zero and positive pitching angles. Note however that the MERCURY code results may have been obtained with the erroneous geometry of Model 1. Results for the Model 1 surface obtained with CFD-ACE are better than the available MERCURY results, however, they are worse than the Model 2 results. Both CFD calculations compare better to test data at the higher pitching angles ($\alpha>0$) for drag and lift coefficients (CD and CL). The pitching moment from the present calculations using the Model 2 geometry, however, shows excellent agreement with test data at the lower pitching angle ($\alpha<0$) and some deviations at $\alpha=15$ and 30 degrees. This behavior is puzzling considering that CD and CL show very good agreement while CM shows the largest deviation from test data. The MERCURY code results for CM show a large discrepancy with test data throughout the whole pitching envelop considered (part of this deviation may be due to the geometry errors of Model 1). The reason for the larger discrepancies of CD and CL between CFD and test results at the negative pitching angles may be explained by the surface pressure coefficients shown below in Figure 4-20.

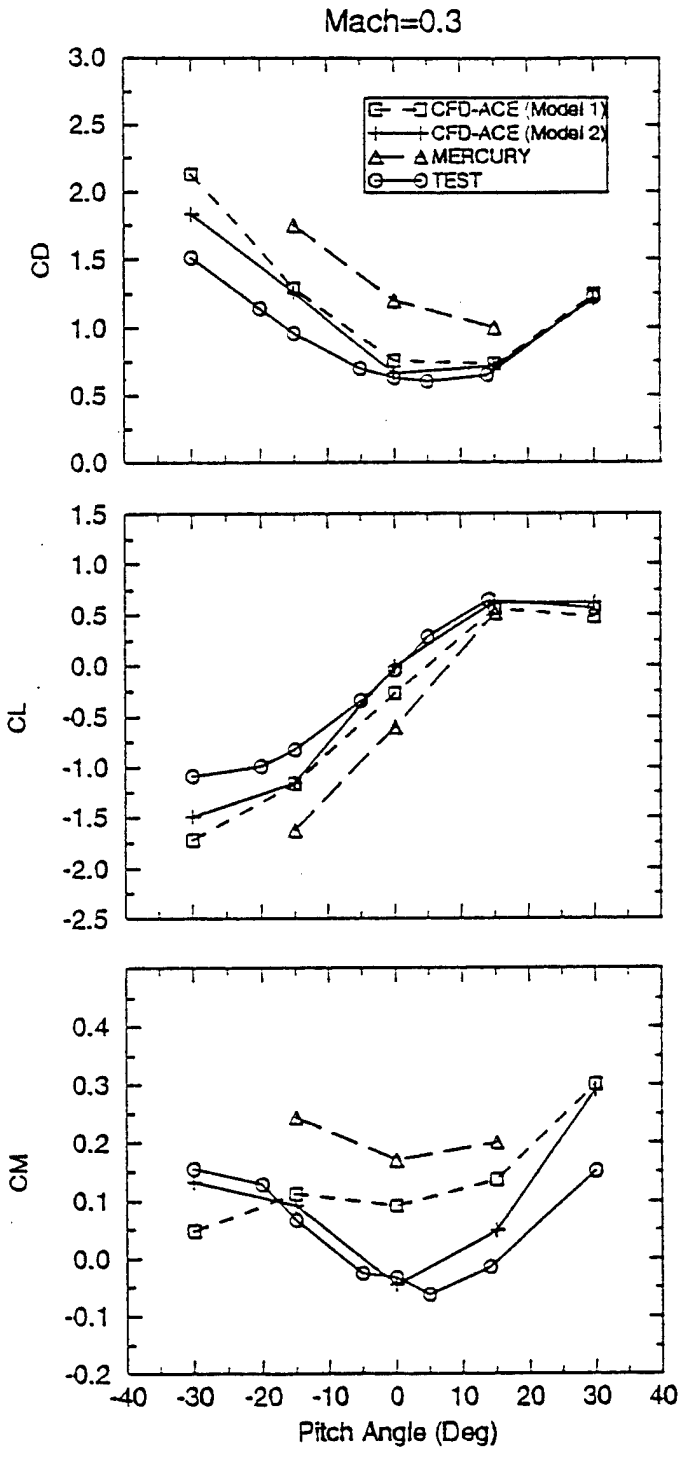

Figure 4-19. Comparison of Force and Moment Coefficients to Wind Tunnel Test Data and MERCURY Code Results; M = 0.3

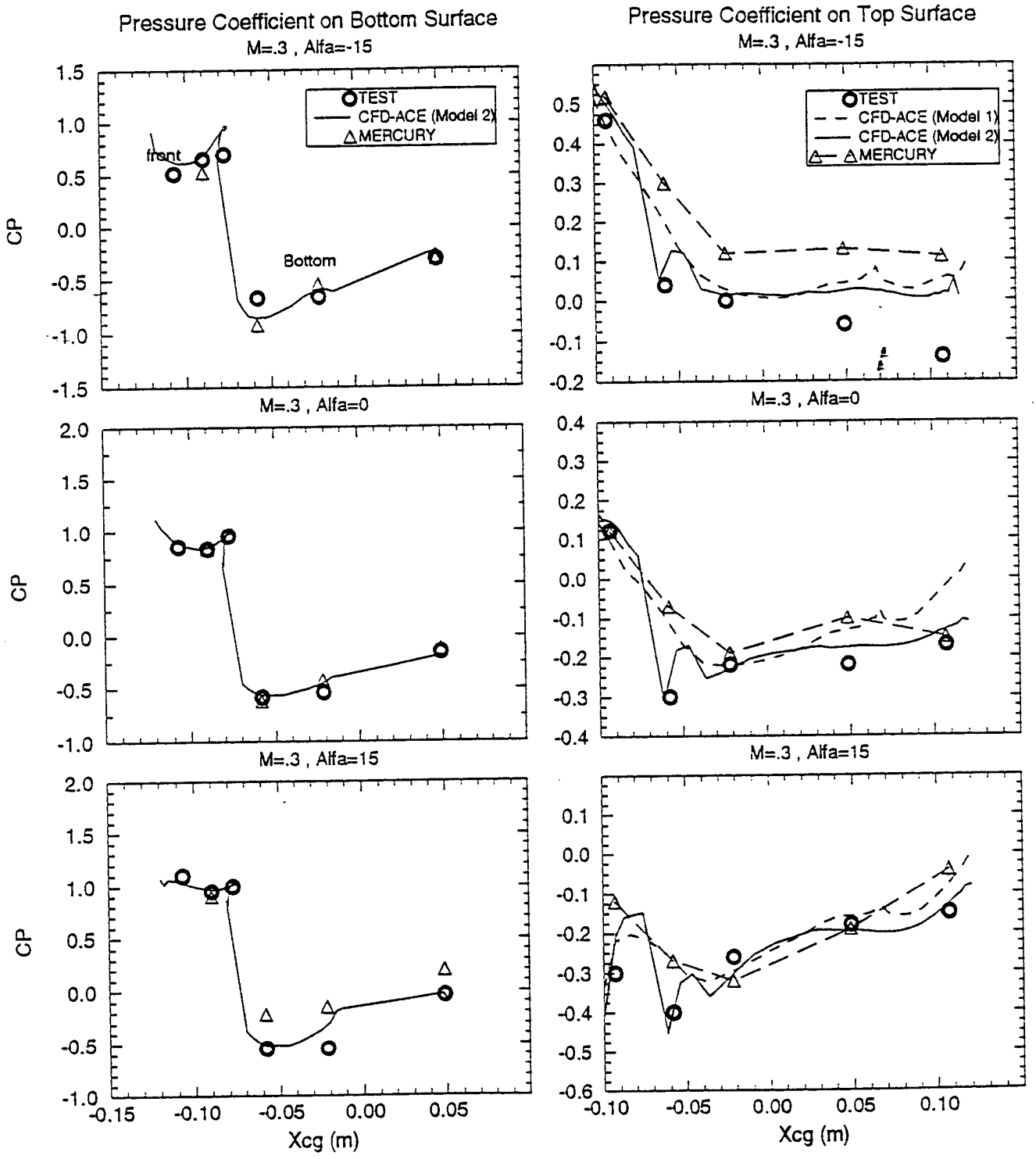

Figure 4-20. Predicted and Measured Force Coefficients for M = 0.3 for Top, Front and Bottom Surfaces

Figure 4-20 compares the surface pressure coefficient to test data at several locations where wind tunnel measurements were taken. Figure 4-21 shows the location of pressure taps where the measurements were made. Figure 4-20 (top right) shows that at α= -15, the predicted pressure coefficient for the Model 2 geometry at the top surface (points 1, 2, 3, 4, and 5 in Figure 9) of the capsule stays constant after the third measurement point while the test data show a monotonic decrease in pressure all the way to the rear of the capsule. This calculated higher pressure at the top contributes to the predicted higher CD and lower CL values shown in Figure 4-19 for α<0. At α=15 (bottom right) the comparison of Cp on the top surface is much better especially near the rear of the capsule.

The reason for the discrepancy in Cp values at α= -15 may be due to the lack of capturing a growing boundary layer at this orientation due to not using a fine enough grid resolution in this region. Figure 4-20 (right) also illustrate the magnitude of the error introduced by the surface geometry. Model 1 predictions show large errors near the nose of the capsule and at the rear especially at α=0 and 15 degrees. The major part of this error is due to the differences in the top surface geometry shown earlier. Therefore, based on this finding it is believed that better agreement may have been obtained with the MERCURY code if the correct surface geometry was used.

Figure 4-20 (left) also presents comparisons of Cp values between the present Model 2 calculations, test data and MERCURY code results at the front and bottom surfaces of the capsule. At α=0 and 15 degrees the agreement with test data is excellent at the front surface (points 15, 16, and 24). This is due to the front surface being almost perpendicular to the oncoming flow at these orientations (see pressure contours presented in Figure 4-24). At α=-15, the spoiler affects the flow on the front face and introduce some perturbations which in turn result in a small discrepancy between predicted and test results. On the bottom surface (points 19 20 and 21 in Figure 4-21) the present results compare well to test data especially at α=0 and -15 degrees. This indicates that the present CFD code captures the viscous effects due to the flow recirculations caused by the presence of the spoiler.

Figure 4-22 shows comparisons of the pressure coefficient at the rear bottom surface (point 33) and rear upper surface (point 34). The agreement between the present calculations and test data at the upper surface (point 34) is excellent for all orientations and better than the MERCURY predictions as expected. At the lower rear surface (point 33) the agreement is not as good. This may be due to the strong viscous interaction not completely being captured because of lack of grid resolution in that region. This agreement is worst at a=-15 degrees where the recirculation zone is the biggest.

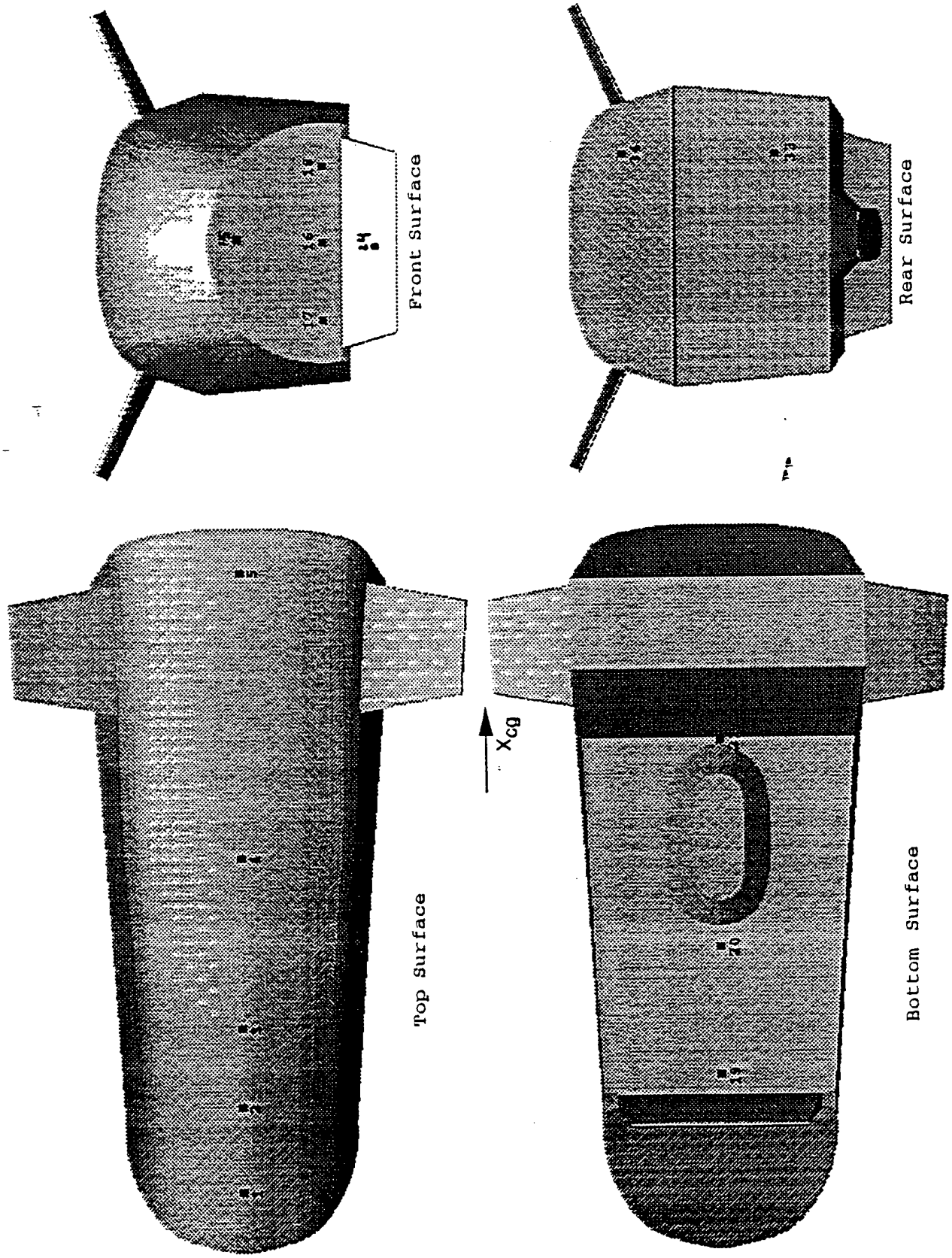

Figure 4-21. Selected Pressure Taps on the Surface of the B-1A Escape Capsule Used for Wind Tunnel Surface Pressure Measurements

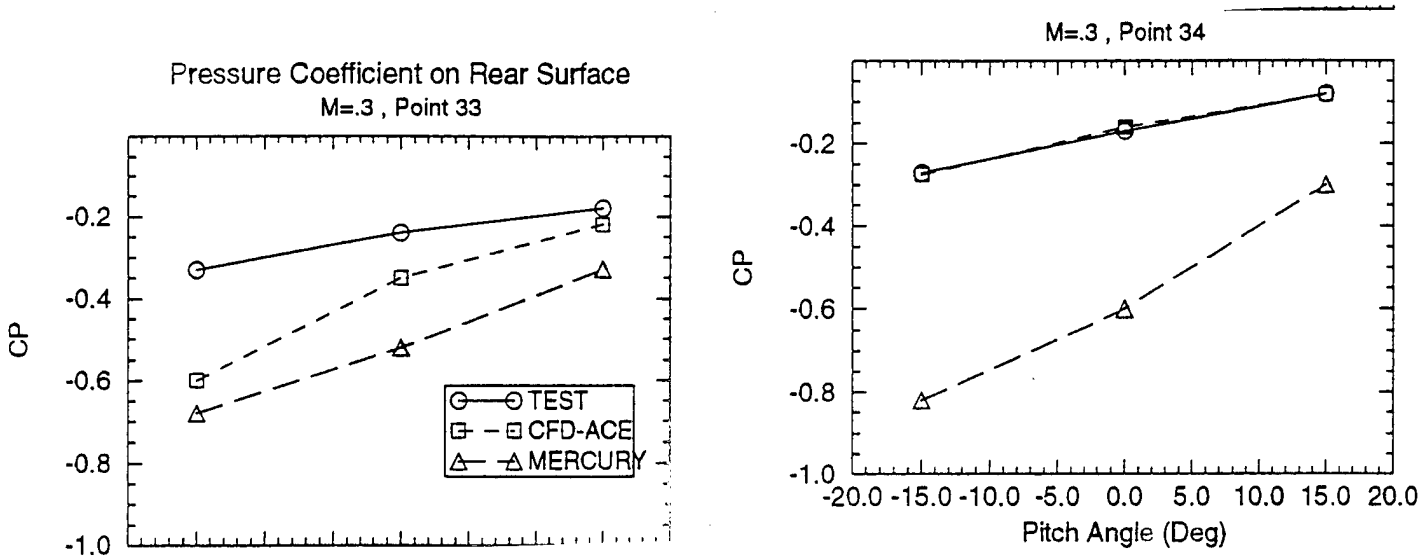

Figure 4-22. Comparison of the Pressure Coefficient to Wind Tunnel Test Data at (a) the bottom rear of the capsule; and (b) top rear of the capsule

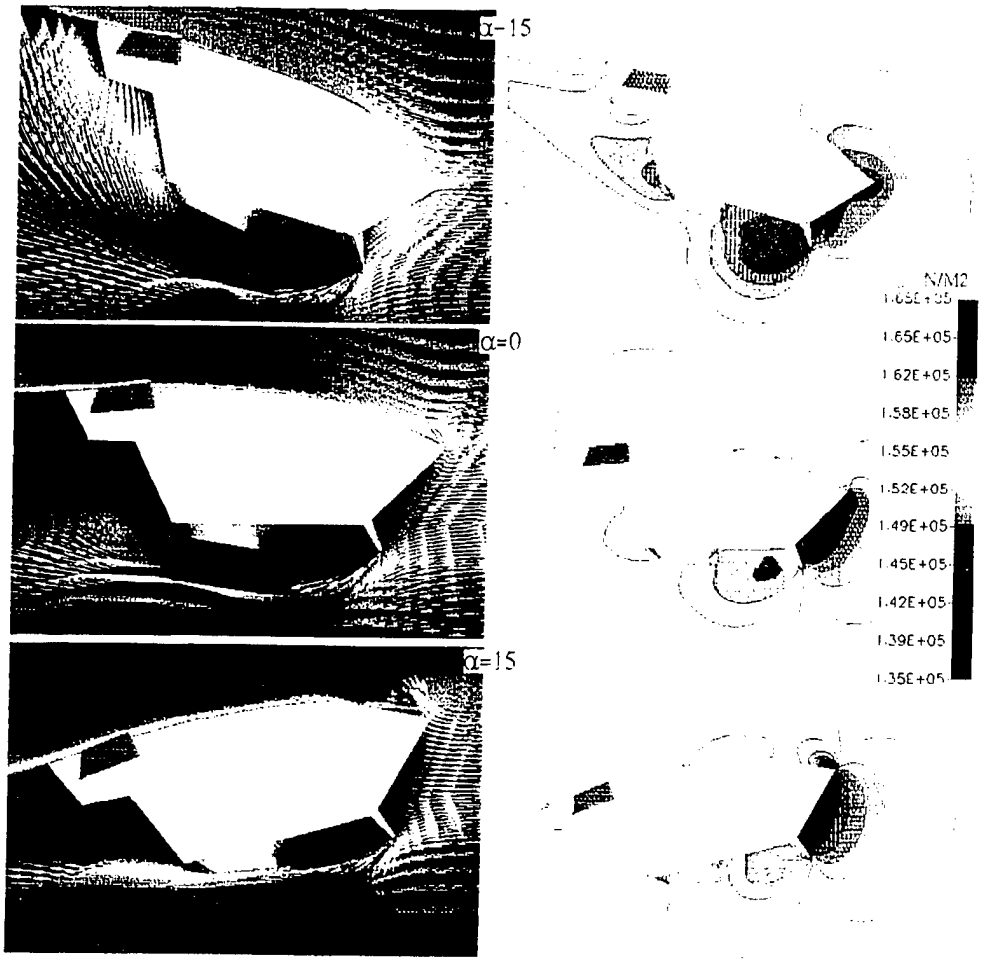

Figure 4-23. Velocity Vectors at the Symmetry Plane for Various Pitch Orientations; M = 0.3

Figure 4-24. Pressure Contours at the Symmetry Plane for Various Pitch Orientations; M = 0.3

The flow behavior and construction around the capsule may be better understood by the velocity vectors. Figure 4-23 shows the velocity vectors near the centerline of the capsule for α=-15, 0 and 15 degrees at M = 0.5. At α=0 and -15, the presence of the spoiler dominates the flow as it forces separation away from the bottom of the capsule creating a large recirculation zone behind it and low pressure regions are shown in Figure 4-24. Figures 4-24 also shows the high pressure encountered at the front surface of the capsule at α = 0 and 15 degrees. At the negative pitching angles the recirculation zone gets stronger and bigger as it covers the rocket housing and causes a strong upward motion of the flow that impinges on the bottom back of the capsule. Figure 4-23 also indicates that two large recirculation zones may take place near the outer surfaces of the capsule due to the strong upward motion that takes place near the symmetry plane separating between the two zones on the sides. To investigate this further the velocity vectors are drawn at several cross planes along the capsule and in the wake to show the progression of the flow and the formation of the recirculation zones as shown in Figure 4-25. A strong recirculation zone forms below the capsule right after the flow goes past the spoiler (Figure 4-25a). The recirculation zone gets wider as the flow moves downstream and eventually occupies most of the area below the tail of the capsule (Figure 4-25d). This large recirculation zone moves upward and gets weaker as the flow moves away from the capsule (Figure 4-25g and 4-25h). Figure 4-25 also shows that a swirling flow forms downstream of the tip of the fins and gets bigger and weaker finally disappearing as the flow moves farther downstream of the capsule (Figure 4-25h).

Figure 4-26 presents the force and moment coefficients from the present calculations and compares them to test results at M=0.95 and M=2.2. Overall the agreement is much better between CFD predictions and test data at the higher Mach numbers than at M=0.3. This is expected due to the weaker viscous interaction and smaller recirculation zones which makes the results less dependent on turbulence and other numerical and physical modeling. The agreement is within 15 percent throughout except for the pitching moment at α=30 for M=.95 and α=-30 for M=2.2. Like the pitching moment for M=0.3 at α>15, this behavior could not be explained since both CD and CL compare very well at these conditions. Figure 4-27 and 4-28 compare the pressure coefficient at the front, bottom and top surfaces to test data at M=0.95 and M=2.2 respectively. At M=0.95 the agreement on the front face is excellent, however at M=2.2 some discrepancies are observed and may be due to the presence of the bow shock located very close to the nose of the capsule as shown later in Figure 4-29. Some numerical noise usually takes place around the shock especially when using a high order differencing scheme like the Osher-Chakravarthy third order scheme used for these cases. At the bottom face agreement is better at M=2.2 due to the narrower and smaller recirculation zones and in turn weaker viscous effects. At the top surface the agreement is good for M=2.2 and some discrepancies are shown for M=0.95 especially at the back of the capsule at a=15 degrees.

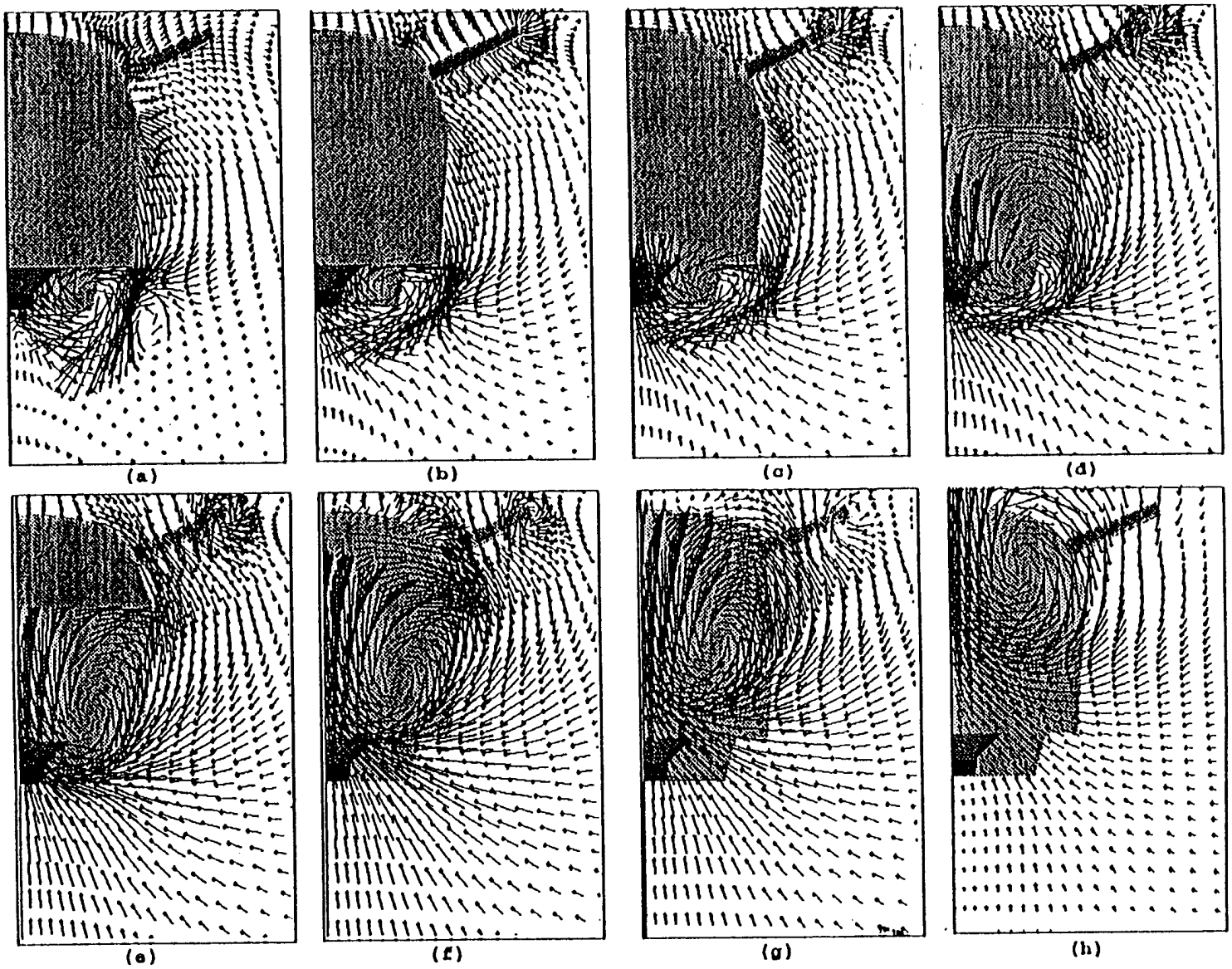

Figure 4-25. Velocity Vectors at Selected Computational Planes Along the B-1A Capsule; M = 0.3, α = 0, (a)-(h): from front to rear of the capsule

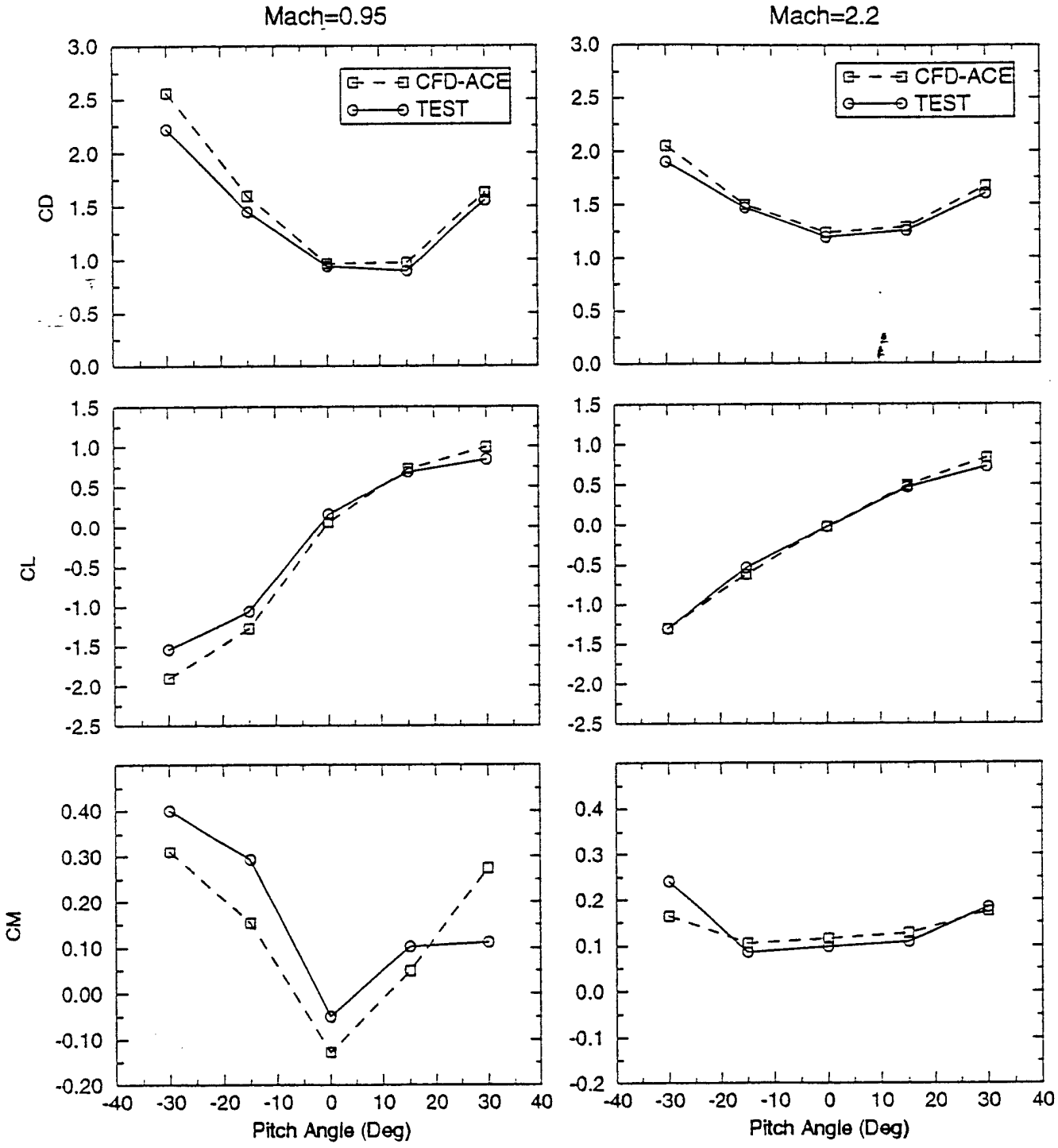

Figure 4-26. Comparison of Force and Moment Coefficients to Wind Tunnel Test Data

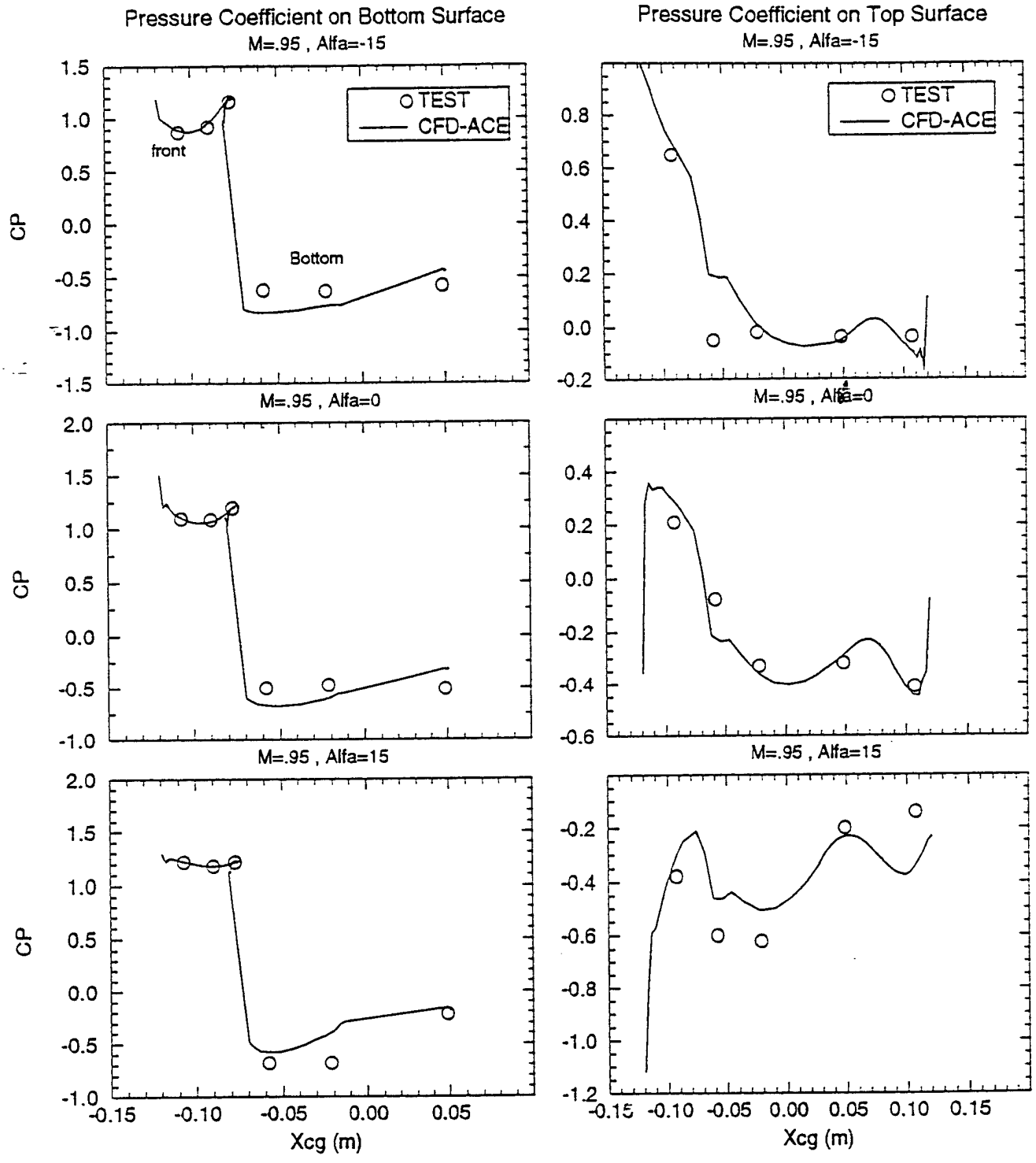

Figure 4-27. Predicted and Measured Force Coefficients for M = 0.95 for Top, Front, and Bottom Surfaces

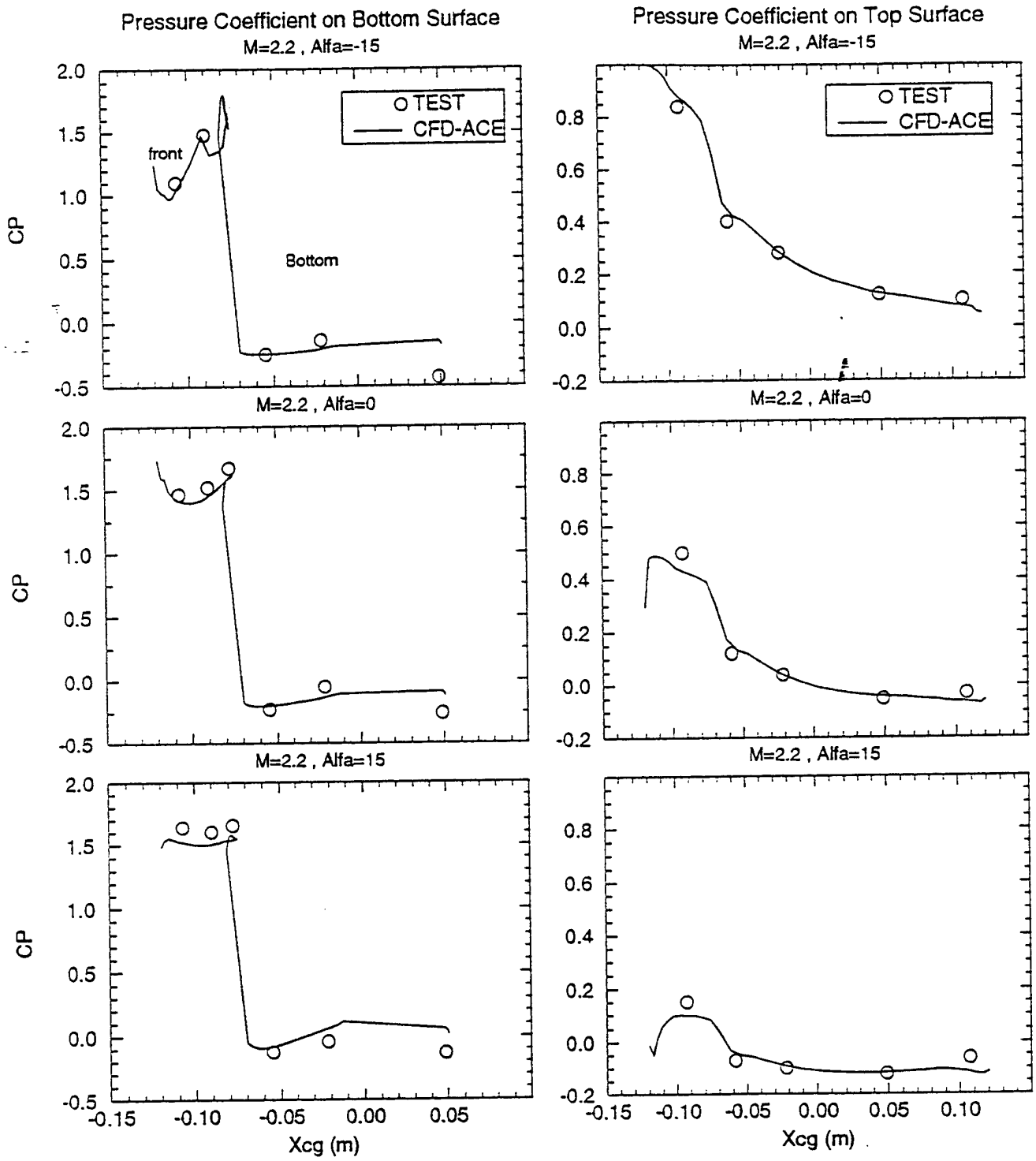

Figure 4-28. Predicted and Measured Force Coefficients for M = 2.2 for Top, Front, and Bottom Surfaces

Finally, to show the differences in the flow structure and progression for the various free stream Mach numbers, the Mach number contours at the symmetry plane are shown in Figure 4-29. At the subsonic M=0.3 condition, the flow approaches the capsule with increasing pressures and decreasing Mach numbers. Separation is formed at the bottom of the spoiler and at the rear top of the capsule. At M=0.95 several reflected shocks are observed including one at the spoiler and one on the top surface at the end of the windshield. An expansion fan is also formed at the rear of the top surface. At M=2.2, the flow is dominated by a strong bow shock located near the front nose of the capsule and the spoiler. Several shocks also take place at the fins surface which is not shown in this figure.

4.3 ACES-II with Mounted Propulsion System Demonstration

This concept utilizes a mounted propulsion system on the ACES-II seat. This propulsion system design is a part of an ongoing 4th generation ejection seat development. This analysis has been conducted to determine the effects the mounted rockets would have on the seat aerodynamic characteristics. Note that the propulsion system is not activated and only the aerodynamic effects of the physical structure of the system are considered.

The modeling of the geometry and grid are discussed next followed by the presentation of the demonstration results.

4.3.1 Geometry and Grid

The geometry for the rocket attachments was obtained from the Navy via another IGES file describing the 4th generation ejection seat. Since a series of baseline CFD simulations had been created for the ACES-II seat, the rockets were attached to the ACES-II seat rather than complete a new grid for the 4th generation seat. The ACES-II seat and 4th generation seats described in the provided IGES files were very similar except in the head box region; the 4th generation seat had a much larger headbox. The rockets were attached to the ACES-II seat very near the same attachment location for the 4th generation seat.

Figure 4-30 shows surface and shaded surface grids for the ACES-II seat with and without rocket attachments from two different viewpoints. Note that several more vertical grid cells exist in the ACES-II seat with rockets than without due to the need to further refine the region near the rockets. Other than this difference, the surface grids are very similar.

Figure 4-31 shows a side view computational plane at the centerline for the seat without rockets and a side view computational plane at the rocket location for the seat with rockets. Note that the relative clustering between the seat with and without rockets is similar.

Computational Results: To analyze the effects of the propulsion system, the ACES-II seat with the propulsion system was simulated at three different pitch angles (a = 0, 15 and 30 degrees) at M = 0.6.

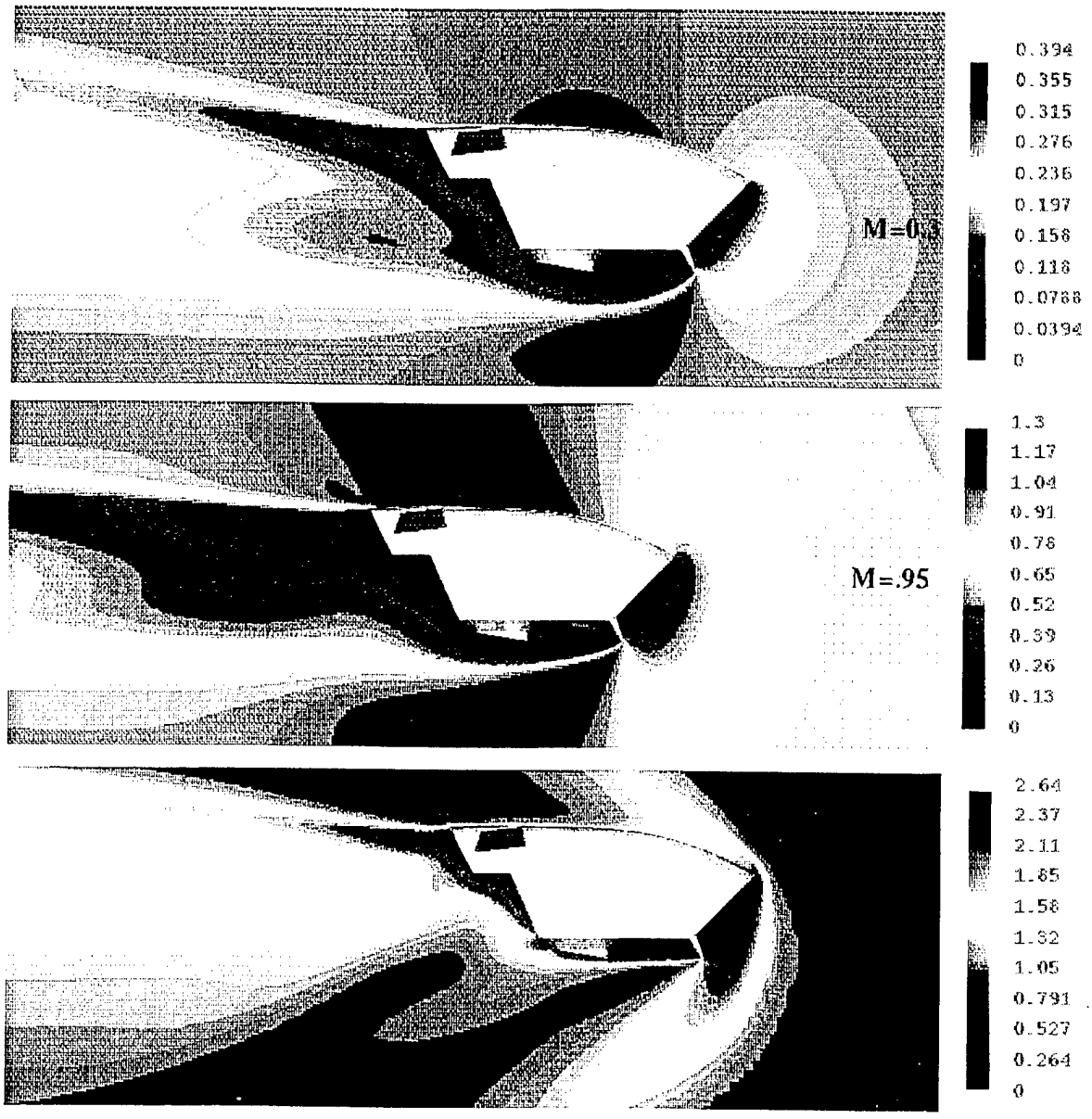

Figure 4-29. Mach Number Contours at the Symmetry Plane for Various Free Stream Mach Number Conditions

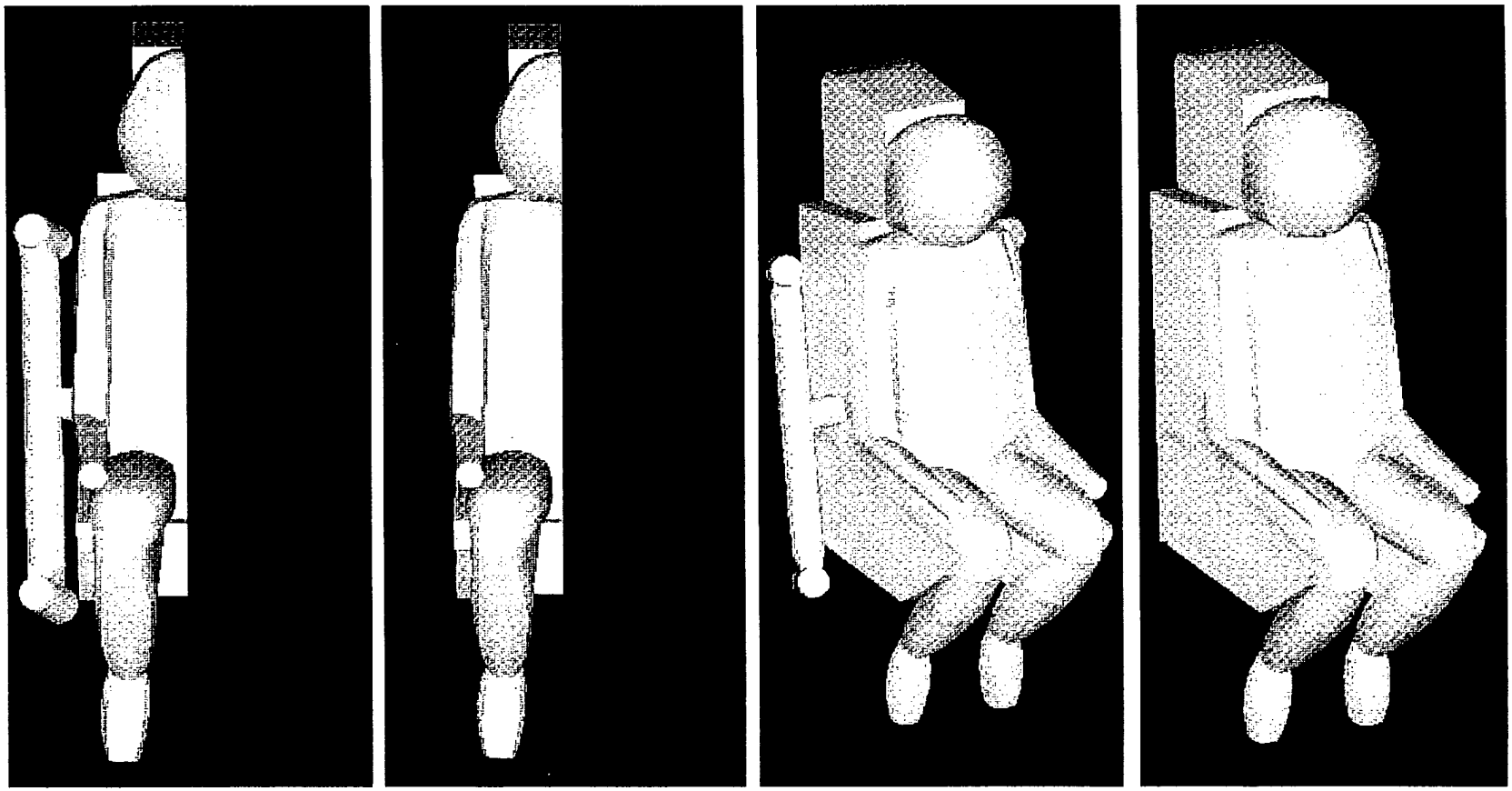

Figure 4-30. Two Views of the Surface and Shaded Surface Grids for the ACES-II Seat with and without Rockets

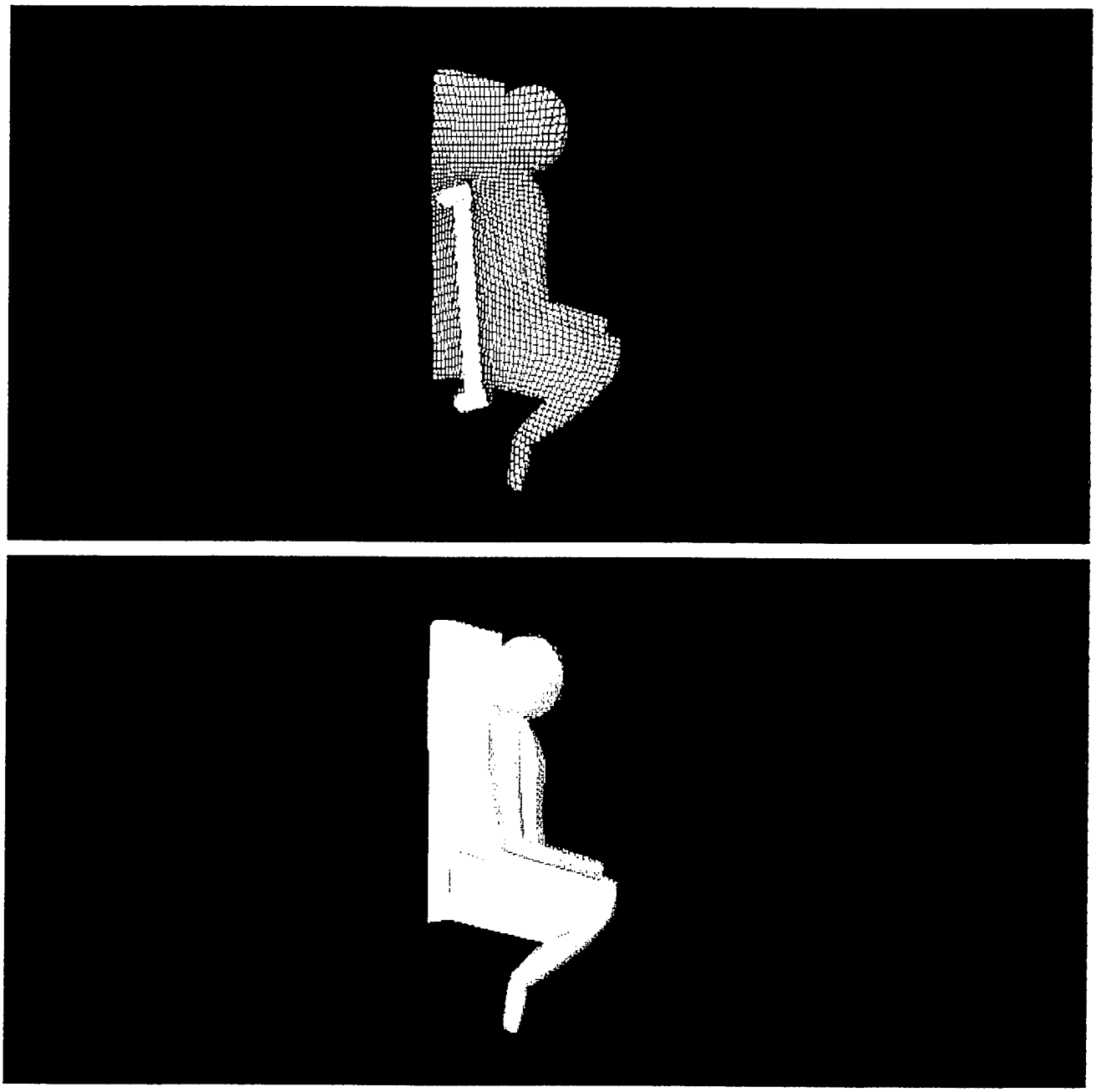

Figure 4-31. Side View Computational Planes for the ACES-II Seat
Upper: ACES-II with Rockets at the Side Plane of the Rockets
Lower: ACES-II without Rockets at the Centerline Plane

Figure 4-32 shows the axial force coefficient, the normal force coefficient, and the pitching moment coefficient vs. pitching angle for the ACES-II seat with and without the mounted rockets compared to wind tunnel test data for the ACES-II seat without the propulsion system. The results of the seat without rockets were discussed earlier in this report. When the rockets are mounted to the ACES-II seat the axial force coefficient decreases throughout mainly due to the increase of the projected frontal area which is used in the coefficient normalization. The calculated projected frontal area for the ACES-II seat with propulsion system is 8.5 ft2 compared to 6.7 ft2 for the seat without rockets. The normal force coefficient of the seat with propulsion system increases sharply at the pitching angle of 15 degrees. This is due to the high pressure on the surface of the rockets and manifold which acts downward at 15 degrees pitch (see Figure 4-33). The high pressure results mainly in an axial force at the zero degree pitch orientation therefore the normal force coefficient does not change much at that orientation. At 30 degrees pitch, the seat is inclined far enough so that the higher pressures would only act on the lower part of the lower rocket, therefore resulting in a minimal change of normal force coefficient. The pitching moment coefficient decreases considerably when the rockets are mounted due to the higher pressure zones encountered on the lower rocket and lower part of the manifold. These high pressure zones results in a pitching moment reduction since they are located below the seat reference point.

Figure 4-33 shows the surface pressure contours for the ACES-II seat with the mounted propulsion system. As indicated above, the high pressures on the lower surface of the rockets and manifold result in a pitching moment reduction and an increase in the normal force coefficient. Figure 4-34 shows the total pressure contours in a computational plane through the seat SRP with and without the propulsion system mounted. This figure shows the effects the propulsion system structure has on the free stream conditions and their location with respect to the seat. This information is valuable in the determination of the location of seat sensors such as the Pitot tubes. This figure shows that the rockets structure has minimal effects on the shape of the flow disturbance region around the seat in that specific plane. Figure 4-35 shows the Mach number contours in an axial computational plane with and without the rockets. For both configurations, the flow decelerates as it approaches the seat with decreasing Mach numbers and higher pressures, then it accelerates past the seat and separates near the shoulders of the occupant creating a large wake behind the seat. When the rockets are mounted, the wake region is much larger and the flow separates at the outer edge of the rockets. An investigation of the wake pressures revealed that the seat with rockets has higher base pressures than the seat without rockets as shown in Figure 4-36. This is expected due to the larger and weaker wake region.

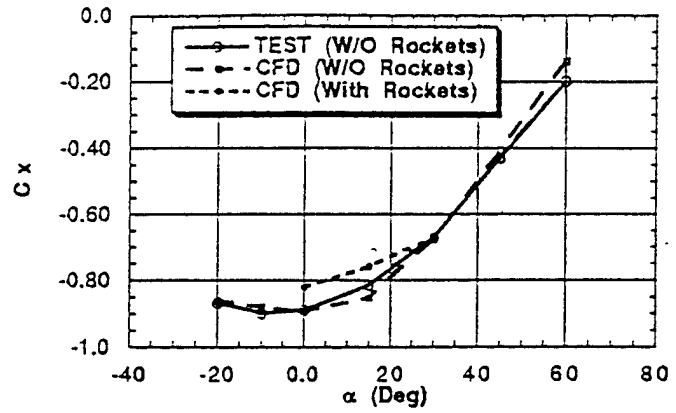

(a)

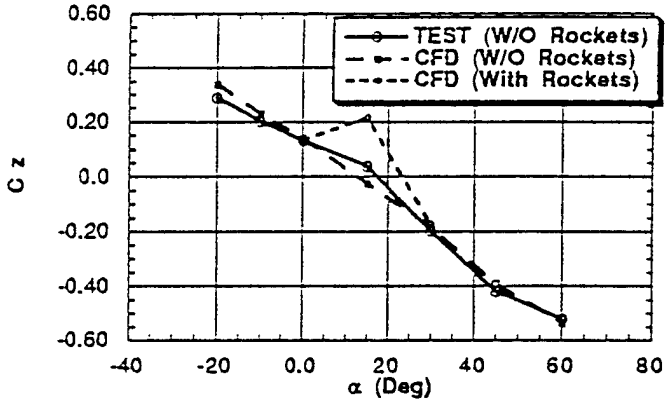

(b)

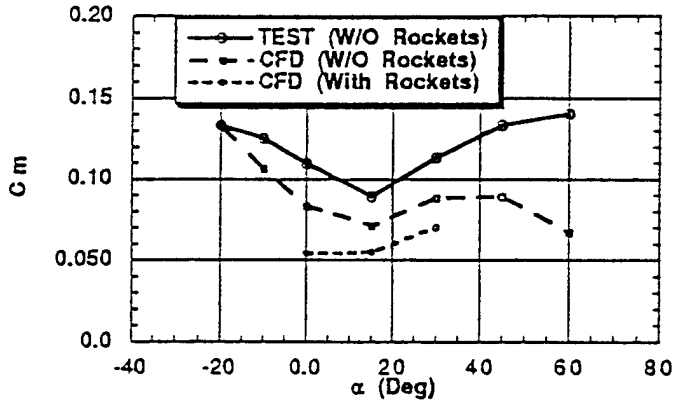

(c)

Figure 4-32. (a) Axial Force Coefficient, (b) Normal Force Coefficient, and (c) Pitching Moment Coefficient of the ACES-II Seat with and without Propulsion System Compared to Wind Tunnel Test Data

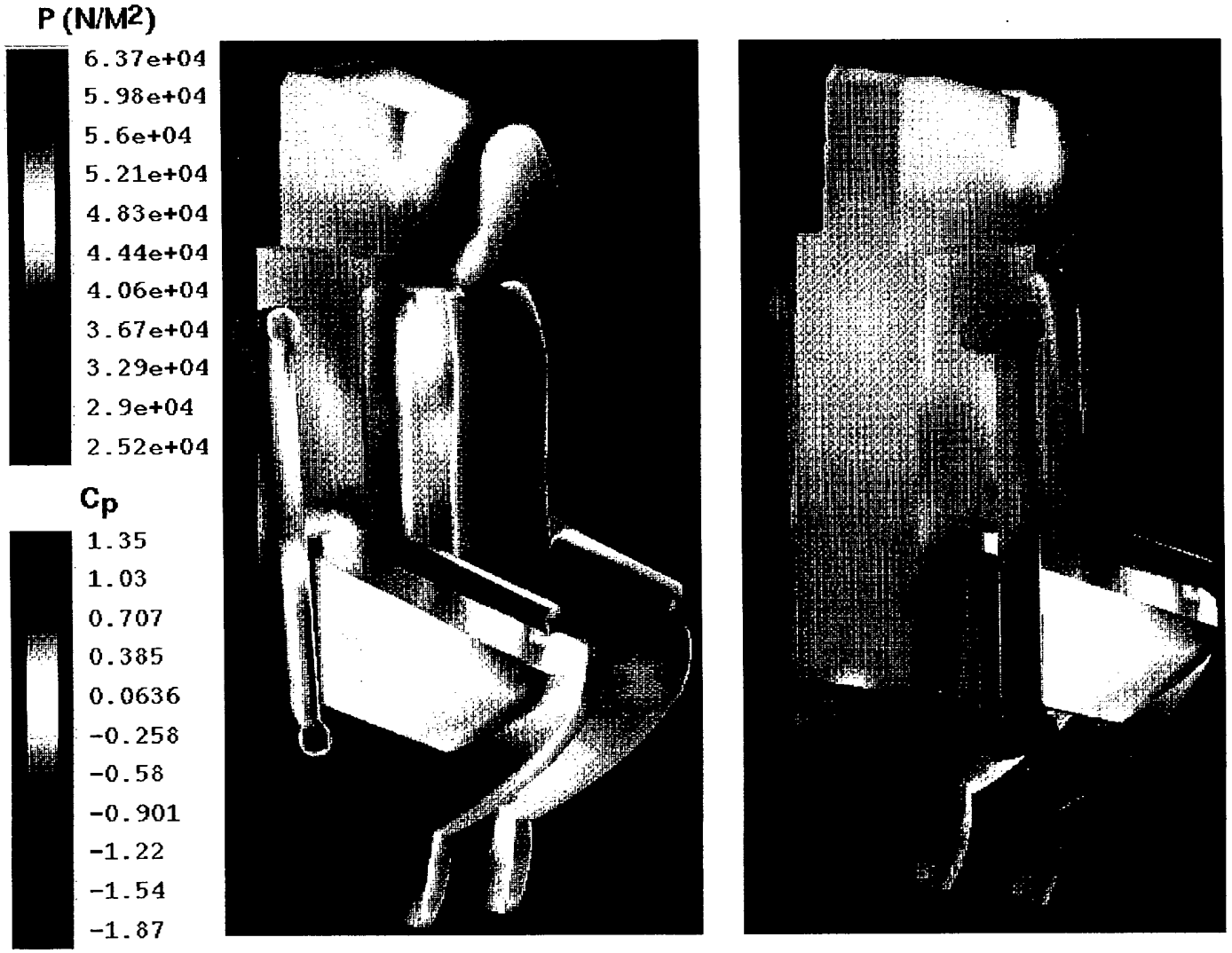

Figure4-33. Surface Pressure Contours for the ACES-II Seat with Propulsion System fo hte Baseline Orientation at Mach = 0.6

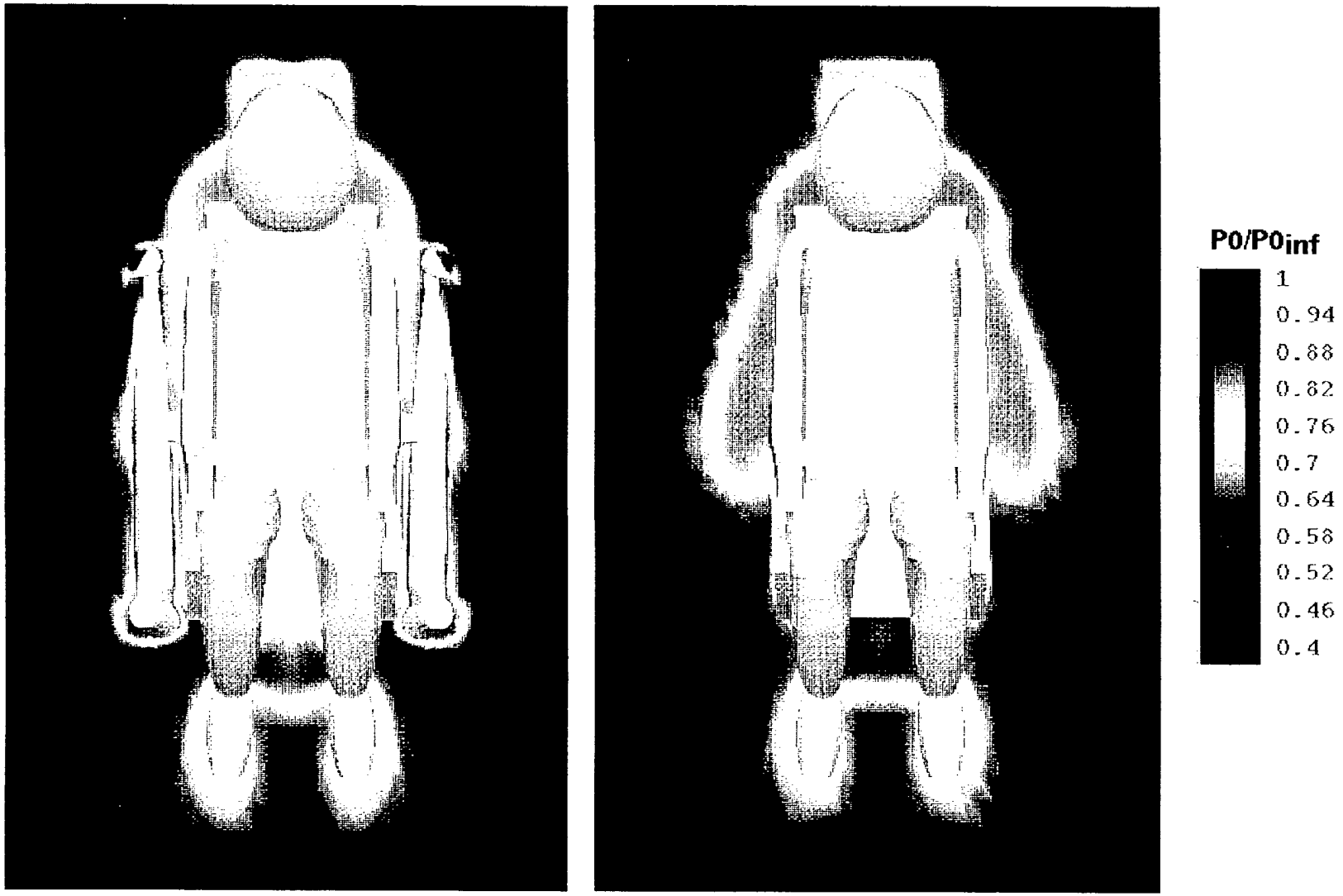

Figure 4-34. Stagnation Pressure at the Plane of the SRP for the ACES-II Seat with and without the Propulsion System Mounted for the Baseline Orientation at Mach = 0.6

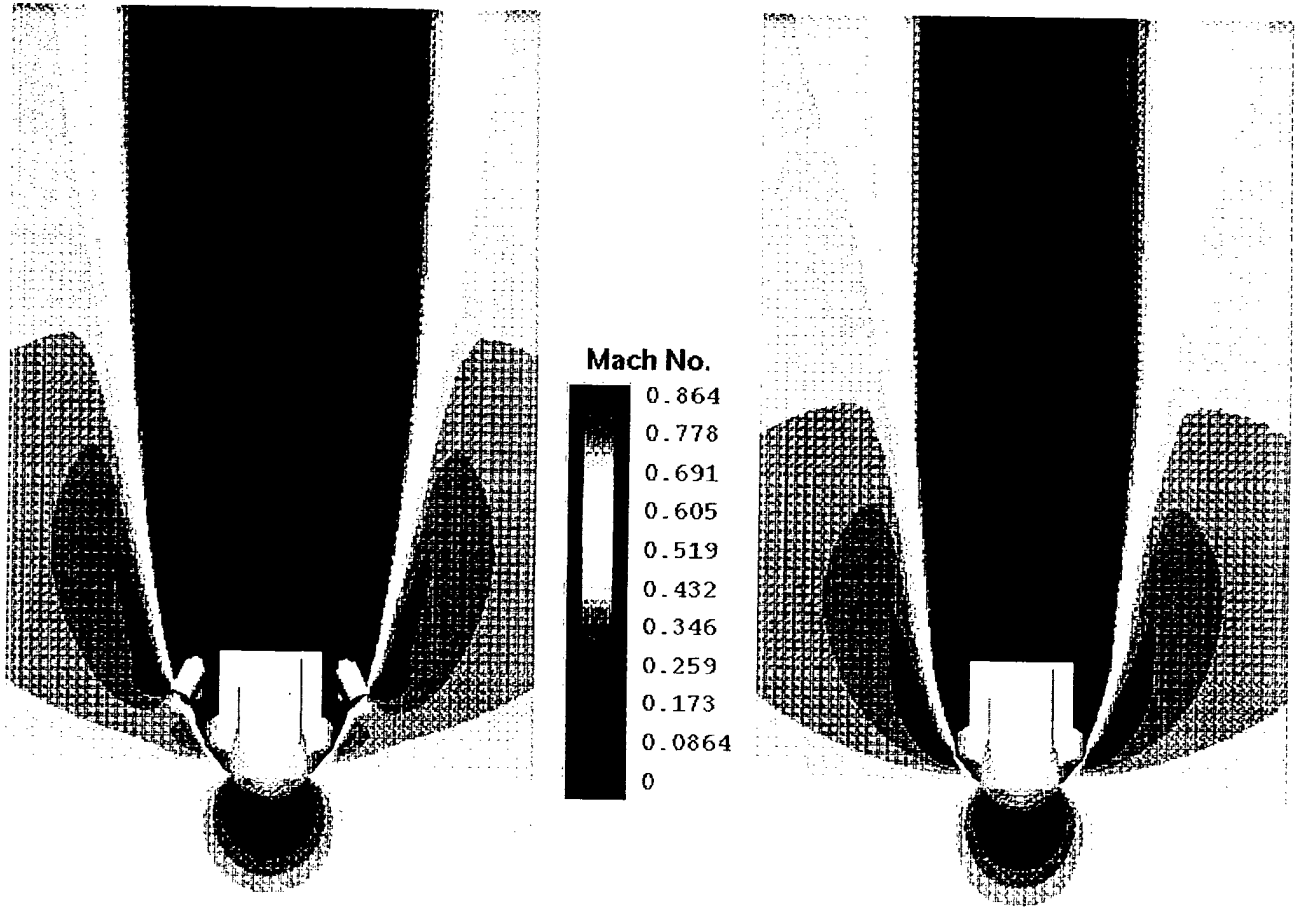

Figure4-35. Top View of the Mach Contours near the Occupant's Head with and without the Rockets Mounted

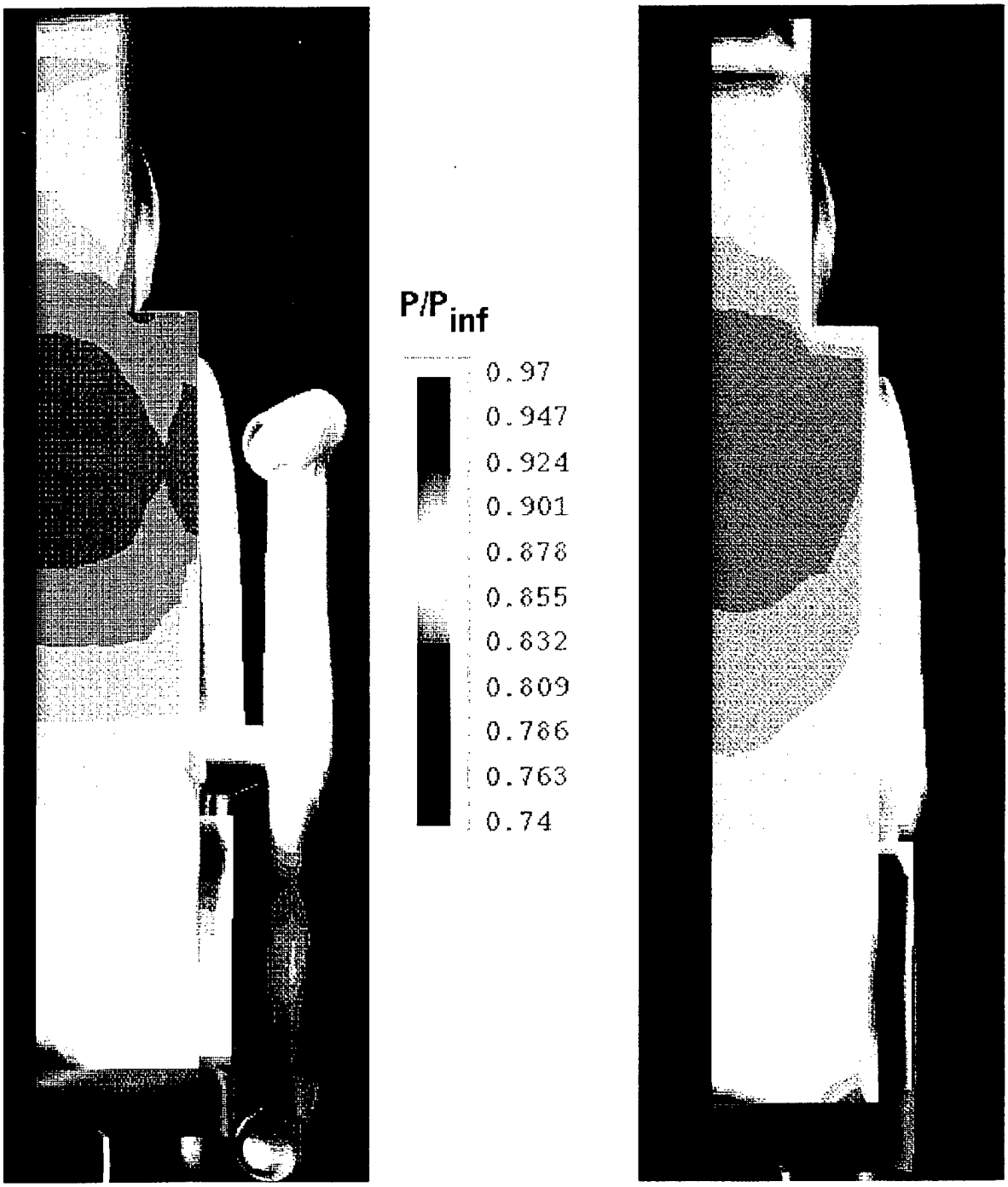

Figure 4-36. Static Pressure Contours on the Back of the ACES-II Seat with and without the Propulsion System Mounted; M = 0.6

5. UNSTEADY SEAT/OCCUPANT FLOW ASSESSMENT AND SIMULATIONS

Besides the validation efforts, several unsteady flow demonstration studies (called demonstrations due to the lack of test data) took place under this project. The results and conclusions from this effort were documented in an AIAA technical paper (AIAA-95-1837) which is included in Appendix A. These demonstrations include:

- Cylinder simulations for unsteady assessment,
- Fixed seat unsteady simulations for transient effects assessment,
- Pitching (rotating around SRP) seat unsteady simulation for transient effects assessment.
- Seat/Aircraft demonstration calculations.

5.1 Cylinder Simulations

The cylinder is a classic unsteady blunt body problem which results in Karman vortex shedding even when the cylinder is not rotating. Substantial experimental work has been completed on stationary as well as rotating and oscillating cylinders which is summarized in Schlichting [32]. In particular work by Jones [21] and Roshko [22] provides dual experimental results at the turbulent subsonic Reynolds number of M = .177, Re = 8.27 x 10^6. Additionally a substantial amount of previous steady state numerical work on turbulent subsonic cylinders has been previously presented in Section 3. The focus of the steady state numerical work was to determine the effects of grid resolution and turbulence modeling on the predicted drag coefficients and their comparison to the experimental results. The work presented in this section presents analogous unsteady CFD results for the unsteady turbulent cylinder problem and the resulting comparisons to experiment and the previous steady state work. Specifically results were obtained at M=0.177 for Reynolds numbers of $1.4x10^4$, $1.4x10^5$, $1.4x10^6$, and $8.27x10^6$.

Before presenting the results, the issue of the initial conditions for these simulations and the resulting effect on solution uniqueness must be addressed. In the steady state simulations an unperturbed free stream condition was used to obtain the familiar steady state two vortex flow pattern shown in Figure 5-1. If the same initial condition is used in an unsteady simulation, the solution converges to the same steady state two vortex pattern of Figure 5-1. However, if a perturbed asymmetric initial condition is used with all other parameters unchanged (i.e., same time-step, boundary conditions, differencing schemes and grid) a periodic Karman vortex shedding pattern is realized as shown in Figure 5-2. Different perturbed initial conditions have been used to obtain the same periodic vortex shedding pattern. Thus, the ability exists to obtain a non-unique numerical solution to the cylinder problem depending on the initial condition used. In nature (or the wind tunnel) the periodic vortex shedding pattern is observed. The ability to obtain a steady state numerical solution (even if a transient simulation is done) suggests that the vortex shedding pattern observed in nature is triggered by the inherent perturbations present in the initial flow field. These observations show that even though

steady state numerical solutions may be obtained for the blunt body problem, they may not be unique solutions.

Even though the flow field pattern for the steady state and periodic solutions are somewhat different, the real question from a design and analysis point of view is: How different are the force and moment coefficients obtained from the unsteady results as opposed to the steady state results?

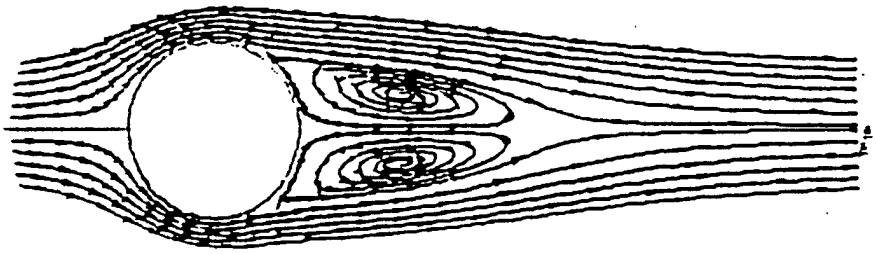

Figure 5-1. Typical Steady State Flow Field Pattern; M=0.177, Re = 8.27×10^6

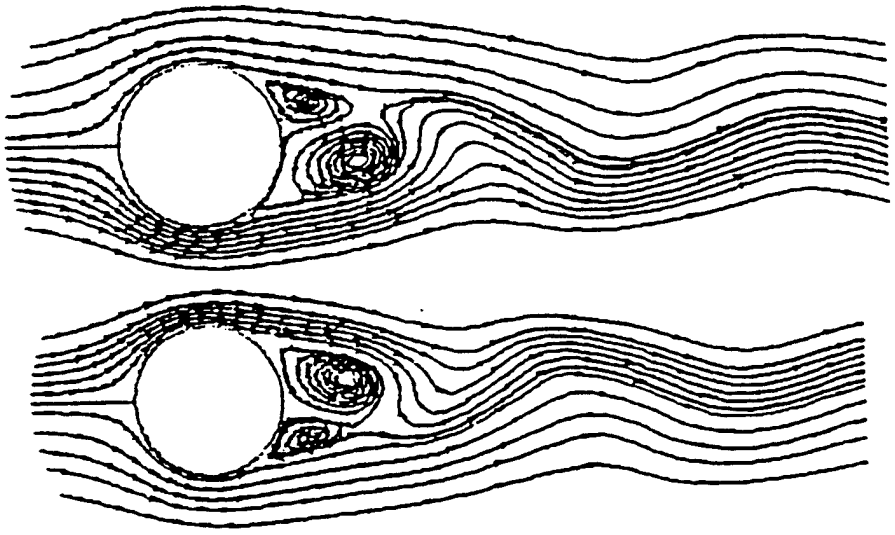

Figure 5-2. Typical Unsteady Vortex Shedding; M = 0.177, Re = 8.27×10^6

Before lift and drag experimental comparisons are made a comparison of the shedding frequency (Strouhal number) to experimental results is useful. An example of the unsteady vortex shedding frequency is observed by plotting the u and v-velocities as a function of time at a location of 1 cylinder diameter behind the cylinder as shown in Figure 5-3. Note that the flow settles to a steady periodic pattern after about 0.7 seconds in this case. The time step used for each of these cases was .001 sec. Table 5-1 shows the Strouhal number comparisons to experimental values given in Schlichting. The coarse grid results refer to a 117x87 polar grid using a non dimensional first cell spacing of 2.621×10^{-3} while the fine grid results refer to a 117x175 polar grid with a non-dimensional first cell spacing of 2.621×10^{-5} At a Re = 8.27×10^{6} the coarse grid corresponds to y^+ of about 500 while the fine grid corresponds to $y^+ \sim 5$. Note at the lower Reynolds number (laminar separation) the coarse grid results produce good comparison to experiment.

At the higher Reynolds number (turbulent separation) the coarse grid results are similar to the low Reynolds result and do not compare well to experiment. The fine grid produces results much closer to experiment although the RNG turbulence model results are somewhat better than the k-e results. Note that at 1.4×10^{6} a true periodic solution does not exist in nature due to the laminar/turbulent transition which occurs in this Reynolds number range. The CFD solution, which assumes turbulent flow everywhere, finds a periodic solution.

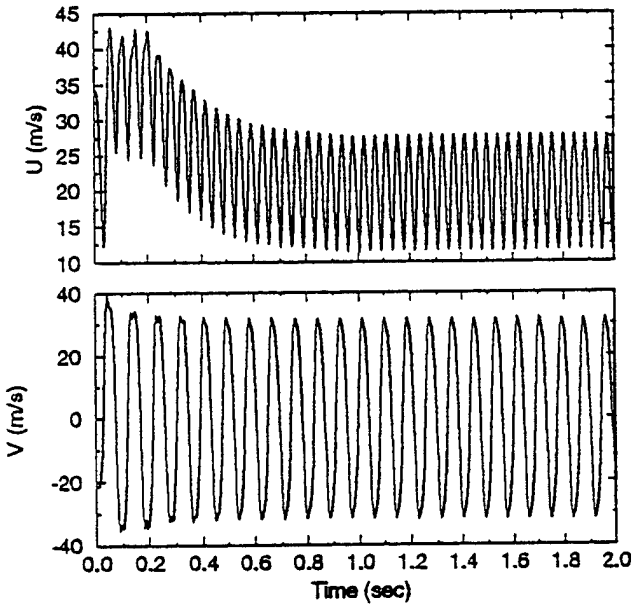

Figure 5-3. History of u and v Velocities at a Location Behind the Cylinder for M = 0.177, Re = 8.27×10^{6}

Experimental steady state results for drag at Re = $8.27x10^6$, M=0.177 have separately been obtained by Jones and Roshko to be .532 and .789 respectively. The difference in their results is due to a differing constant back pressure value in the separated region. Table 5-2 shows drag results at M = .177, Re = $8.27x10^6$ for the steady and unsteady cases. The unsteady value represents a time averaged value once the periodic vortex pattern was established. Figure 5-4 shows the drag and lift histories for the coarser grid with k-e turbulence model case. The steady state (2 vortex pattern) drag results do not compare very well to experiment. A thorough analysis of numerical factors affecting the steady state drag was presented in Section 3. In particular the grid resolution and turbulence model constants significantly affect the resulting drag, an observation confirmed by the results in Table 5-2. The unsteady results in each case produced significant improvement in the drag predictions, especially for the RNG turbulence model. Even the coarse grid case, which did not compare well for Strouhal number, has significant improvement although, less pronounced than the other 2 cases.

The difference in drag results for steady state simulations as opposed to time averaged unsteady simulations was significant. Additionally the magnitude of the difference was dependent on the grid and turbulence model employed. These results underscore the possible differences between steady state and unsteady numerical results for the blunt-bodied vortex shedding case.

Table 5-1. Computational Strouhal Numbers for M = .177

Re	Turbulence Model	Grid	S	Experiment (Schlicting)
$1.4x10^4$	k-e	coarse	.185	.198
$1.4x10^5$	k-e	coarse	.179	.196
$1.4x10^6$	k-e	coarse	.179	--
$8.27x10^6$	k-e	coarse	.189	.292
$8.27x10^6$	k-e	fine	.353	.292
$8.27x10^6$	RNG	fine	.311	.292

Table 5-2. Steady and Unsteady Drag Results for Re = 8.27x106, M = .177

Case	Grid	C_D	Case	Grid	C_D
Steady k-e	coarse	.235	Unsteady k-e	coarse	.303
Steady k-e	fine	.19	Unsteady k-e	fine	.37
Steady RNG	fine	.28	Unsteady RNG	fine	.76
CD from Experiment: Jones .532, Roshko .789					

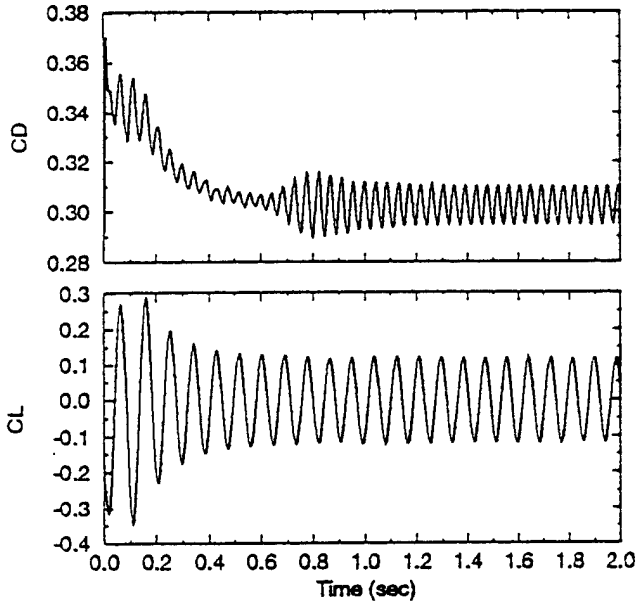

Figure 5-4. Lift and Drag Coefficients for M = 0.177 and Re = 8.27 x 10^6

5.2 2-D Ejection Seat Simulations

To understand the flow characteristics around a typical ejection seat geometry and to assess the importance and effects of flow unsteadiness on aerodynamic coefficients, several calculations have been performed on a 2D ejection seat geometry. The 2D geometry was chosen for strictly economic purposes, for, to conduct a study of this magnitude on a full 3D ejection seat grid (similar grid resolution) would be economically very expensive in terms of needed computer resources. It is anticipated, however, that the unsteady effects will be more pronounced with the 2D geometry than the 3D geometry because larger flow separation and increased wake size with the 2D geometry. To assess this effect a limited 3D coarser grid resolution unsteady simulation is performed and the results are presented in the following section.

For the 2D ejection seat geometry, several calculations have been performed. The history of the calculations is as follows: first steady state calculations were performed on a typical mid plane 2D ejection seat geometry and grid and aerodynamic coefficients were calculated. Second, unsteady calculations were performed on the same geometry for 1.5 seconds in steps of .001 seconds starting from a perturbed solution (as discussed in the cylinder section above). Then unsteady calculations were performed on a seat pitched from 0 to 45 degrees and then pitched back from 45 to 0 degrees. A utility was developed to rotate the seat and adjust the grid for the new seat orientation. Several initial conditions, time step and pitching angle increments were used. The results from all the above discussed calculations are presented below.

5.2.1 Steady State Calculation

Figure 5-5 shows the elliptically smoothed computational grid used for the 2D fixed ejection seat geometry. The calculation domain extends about 5 seat heights around the ejection seat. Calculations were performed at M = 0.6 and Re = 8×10^6. A first order upwind scheme was used to get the results shown in Figure 5-6. Attempts to use a higher order central differencing scheme failed as convergence was difficult due to oscillations. Figure 6 presents the upwind results where the streamline and pressure contours are shown. The streamline contours indicate the presence of two recirculation eddies in the back of the seat.

The flow separates near the head and feet of the occupant and reattaches about 2.5 seat/occupant heights downstream. The drag and lift coefficients were normalized by the seat/occupant height which is 1.848 m. The calculated CD and CL were 1.38 and -.257, respectively.

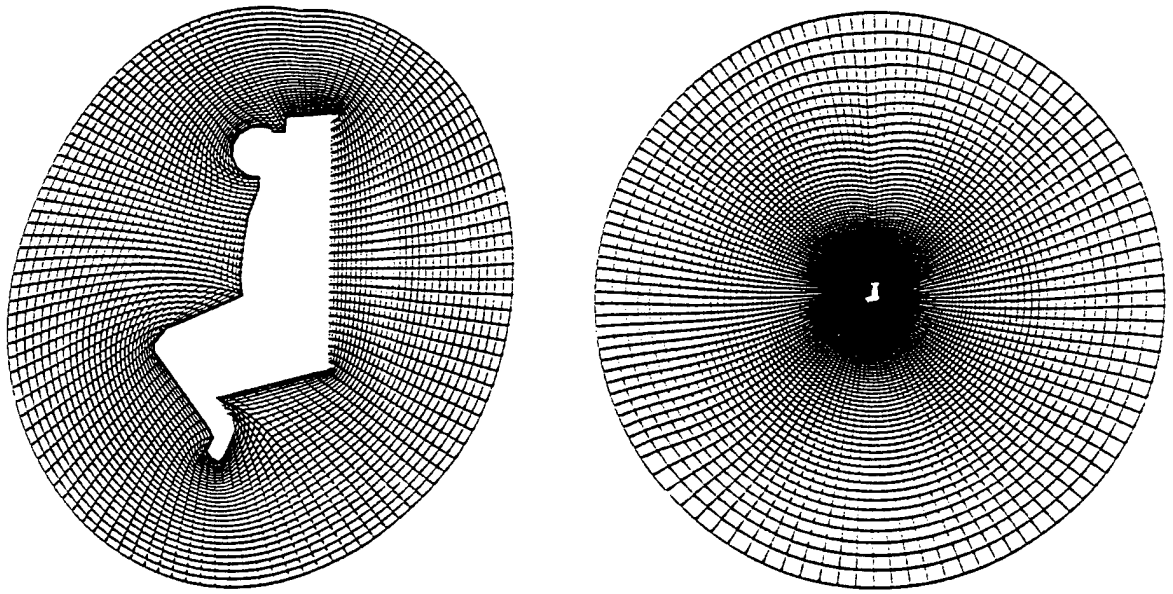

Near Field Far Field

Figure 5-5. Near Field and Far Field Views of 2D Ejection Seat Grid

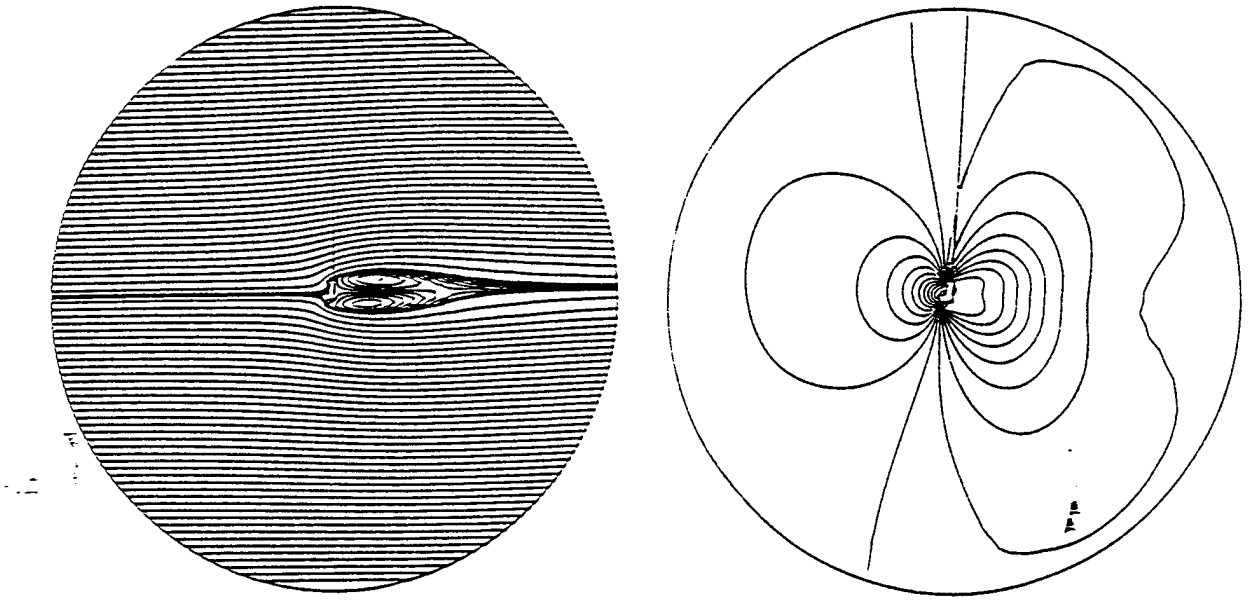

Streamline Contours Pressure Contours

Figure 5-6. Streamline Contours (a) and Pressure Contours (b) from 2D Ejection Seat Steady State Calculations

5.2.2 Unsteady Calculations/Fixed Seat

Unsteady calculations were then performed on the same geometry to observe the vortex shedding formation and their effects on the calculated drag and lift coefficients. When converged steady state results were used for the initial conditions, the solution would converge and settle to that of steady state solution and no perturbations or oscillations would be formed. To get an unsteady vortex shedding solution, a perturbed initial condition was used. Calculations were performed for 1.5 seconds in time step increments of .001 seconds.

The flow for the first 150 time steps (time = .15 seconds) seems unstable and does not show any cyclical or repetitive patterns. After this initial stage a clear cyclical pattern is observed (as seen in Figure 5-7) and a typical vortex shedding flow pattern is formed as seen in the streamline contours shown in Figure 5-8. Figure 5-7 shows the history of drag and lift coefficients and the perfect oscillations associated with vortex shedding flows. Note that the average values of CD and CL are about 2.0 and -.325 respectively and they differ considerably from the steady state results which were calculated to be 1.38 and -.257 for CD and CL.

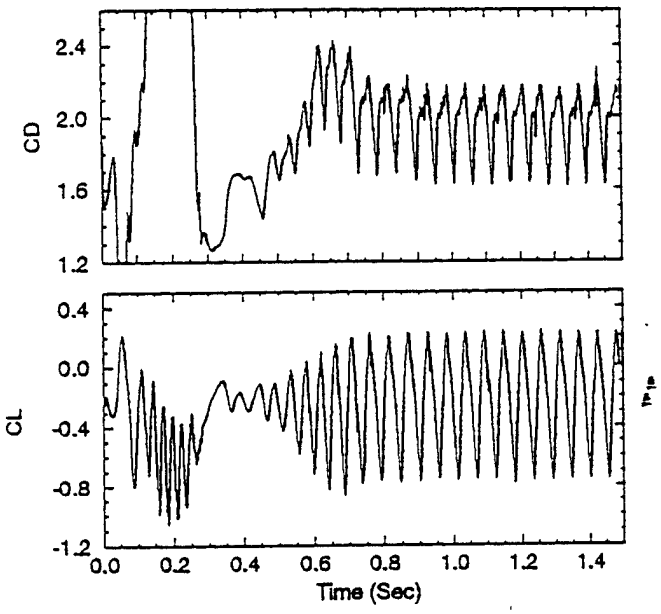

Figure 5-7. Drag and Lift Coefficients From Unsteady Calculations Over a 2D Fixed Ejection Seat

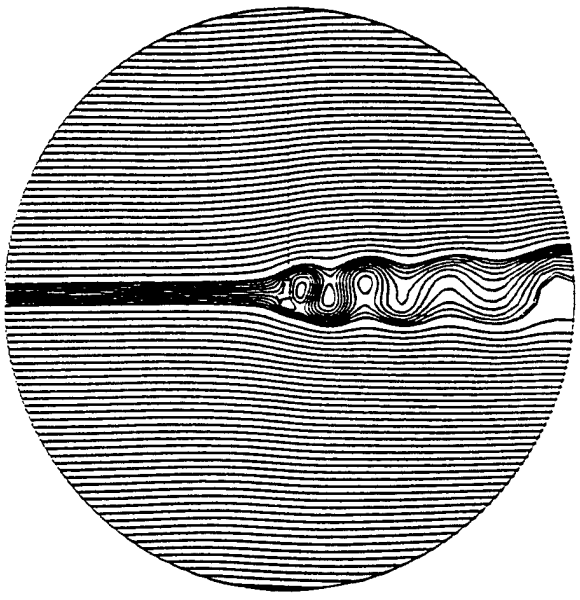

t = 40

Figure 5-8. Typical Vortex Shedding Behind 2D Ejection Seat Geometry from Transient Calculation; M = 0.6

The discrepancy between the time average and steady state results is about 30 and 20 percent for CD and CL respectively which is very similar to the discrepancies found for the cylinder geometry. Figures 5-6 and 5-8 reveal that the size of the wake is larger for the unsteady calculation. The larger wake results in lower overall back pressure which in turn results in the higher time average drag and lower lift (due to inclination of bottom surface).

5.2.3 Unsteady Calculations/Rotating Seat

Several calculations were performed for a pitching (i.e. rotating) seat. The same computational grid used for the fixed orientation was utilized for these calculations. The seat was pitched each time step according to an assigned pitching angle increment and the computational grid was adjusted accordingly. A grid adjustment routine that retains the elliptic smoothness of the original grid was used for this purpose. CFD-ACE moving grid capability was used to retain full conservation as the grid is moved each time step.

Figure 5-9 presents the lift and drag coefficients for the case using unsteady fixed seat initial conditions and timestep of .0011 seconds and pitching angle increments of .05 degrees. The pitching envelope goes from 0 to 45 degrees and back from 45 to 0 degrees. The drag coefficient decreases as the pitching angle increases as expected due to the lower projected frontal area. The oscillation patterns persist throughout and the amplitude becomes smaller at the higher pitching angles. As the seat is pitched back from 45 to zero degrees, the same type of oscillations are observed and the lift and drag pattern traceback around an imaginary time averaged line of the 0 to 45 degree results.

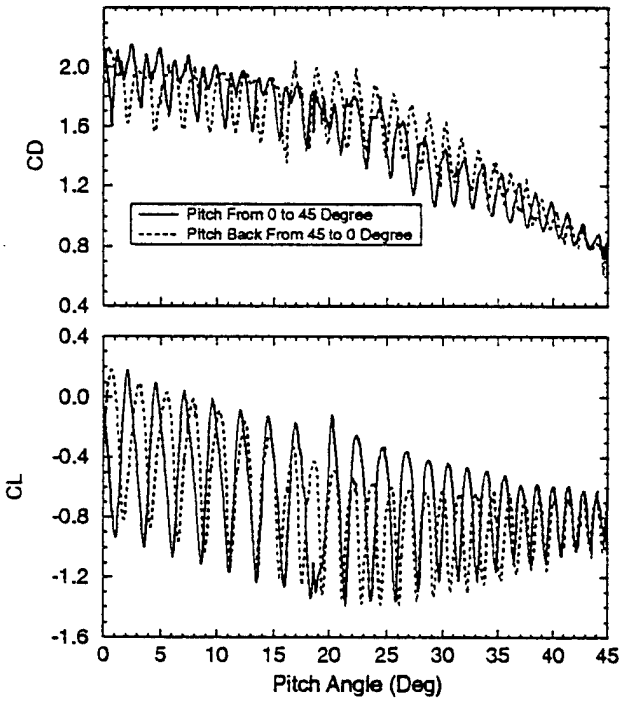

Figure 5-9. Lift and Drag Coefficient for a Pitching Seat Using Unsteady Initial Conditions

Figure 5-10 shows the streamline contours at different pitching orientations. The vortex shedding pattern is observed throughout, however, the amplitude becomes smaller and dies down as the pitch angle increases.

Several other calculations were performed using the steady state results as the initial conditions. Pitch angle increments of .05, .1, .2, and .5 were used. The corresponding time steps were .0011, .0022, .0044 and .011, respectively. The purpose of these calculations was to observe the formation of flow oscillations if any and at what time step and pitching angle increments they would form and how the results compare to the above results (starting from unsteady fixed seat results).

Figure 5-11 presents the drag and lift coefficients for all the calculations performed on the pitching seat including the steady state results. It is observed that a large discrepancy exists between steady state and transient initial conditions, at the lower pitching angles (i.e. α=0) as discussed above for the fixed seat. As the pitching angle increases the discrepancies become smaller due to the shrinking size of the wake and therefore the reduction of the vortex shedding effects. At Δt = .011 and $\Delta\alpha$ = .5, the drag and lift coefficients along with the streamline contours (presented in Figure 5-12) show no oscillations throughout the pitching envelope and no vortex shedding is formed. As smaller time steps are used (and in turn smaller pitching angle increments) oscillations start to form, and they ultimately appear to follow the same pattern as the unsteady initial condition case especially at Δt = .0011 and $\Delta\alpha$ = .05 degrees. This behavior is different from the unsteady calculations on a fixed seat using steady state converged results for initial conditions where the solution always stayed at that of the steady solution and no oscillations were formed.

It seems like the pitching of the seat introduces the perturbations that ultimately result in the oscillations and vortex shedding mechanism. What is interesting is that these oscillations seem to converge on a unique solution irrespective of the initial conditions as long as the perturbations are introduced.

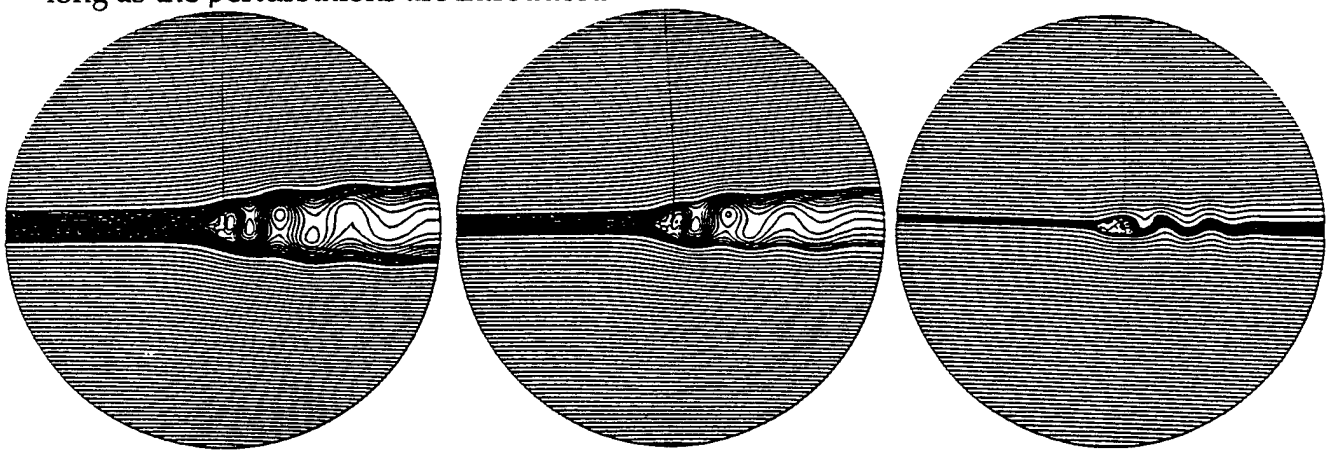

Figure 5-10. Streamline Contours for 2D Seat at Different Pitch Angles; Unsteady Initial Conditions

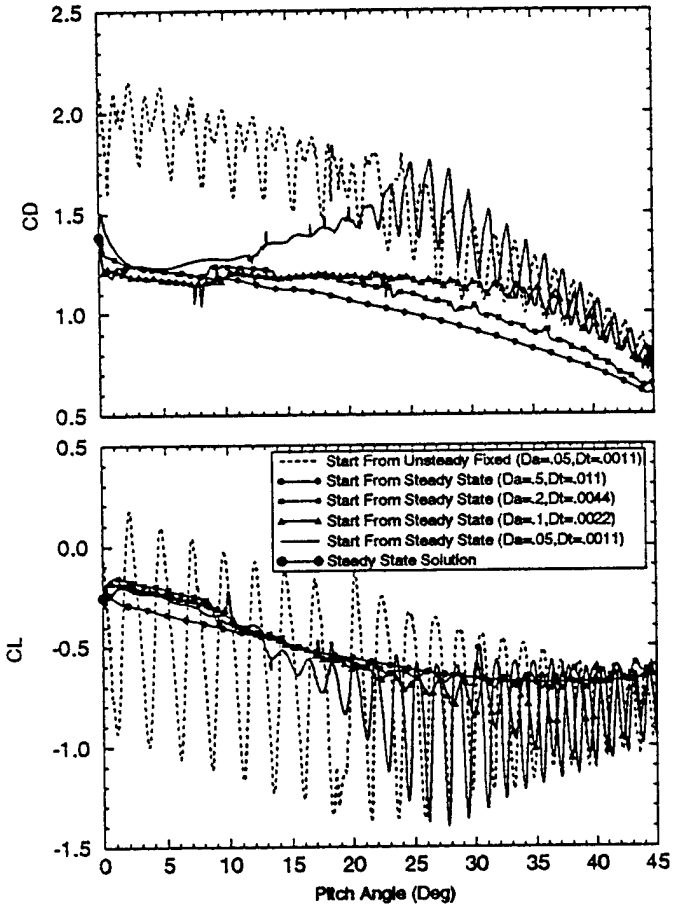

Figure 5-11. Drag and Lift Coefficients for a 2D Pitching Set

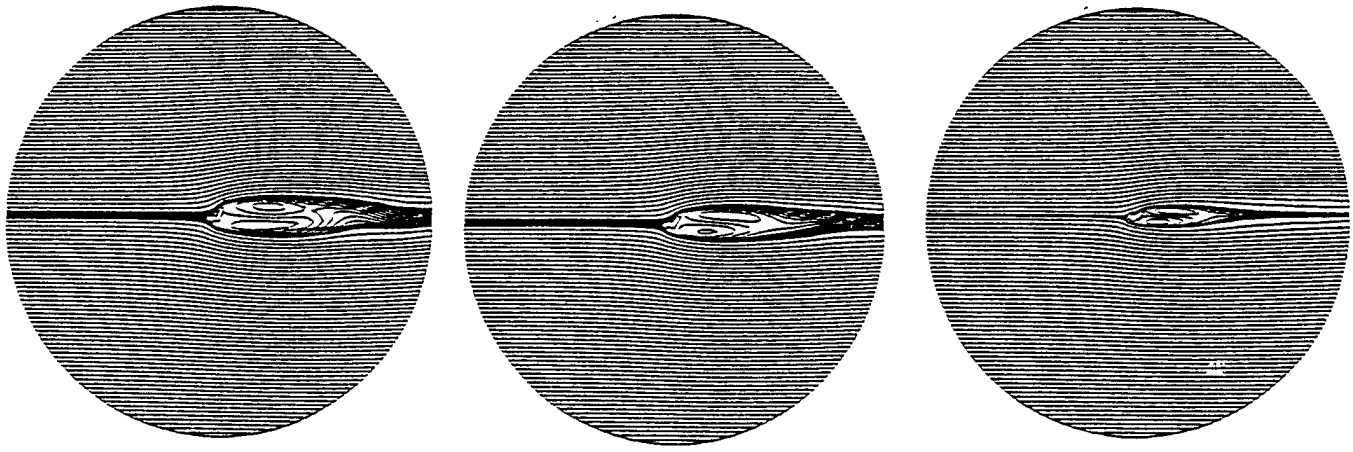

$\mu = 10$ $\mu = 25$ $\mu = 40$

Figure 5-12. Streamline Contours at Different Pitch Orientations; Steady State Initial Conditions

5.3 3-D Ejection Seat

Steady state calculations have previously been performed on a 3D ejection seat (ACES-II seat) and results have compared well with wind tunnel test. The surface geometry and computational grids algorithm results were presented in Section 4.1.2.

To assess the importance of unsteady effects on the 3D ejection seat results a limited unsteady analysis was conducted on the 3D ejection seat geometry. Note however, that the grid resolution (as seen in Figure 4-5) is much coarser than the 2D ejection seat grid resolution (shown previously in Figure 5-5). The grid resolution may be an important factor in predicting flow oscillations and vortex shedding.

Unsteady calculations were performed for a fixed as well as a rotating seat using both steady state and perturbed initial conditions. Results are presented for: unsteady calculation of flow over a full ejection seat geometry starting from perturbed initial conditions, and unsteady calculation of flow over a pitching half ejection seat geometry starting from steady state solutions.

Results from unsteady calculations over a 3D ejection seat geometry starting from steady state solutions showed no oscillations and quickly converged to the steady state solutions as was observed in the 2D ejection seat calculation. The above calculations were repeated with perturbed initial conditions. In this case the steady state solution was run for few iterations only to get a perturbed non-converged solution which was used as the initial condition. Figure 5-13 presents the axial velocity and pressure vs. time at a monitoring point behind the seat near the symmetry plane. Some perturbations and oscillations are observed initially however, these oscillations die out monotonically as time increases and the solution eventually approaches the steady state solution. These results are indeed different than the 2D results (although same time step was used) when starting from perturbed solutions. The 2D results showed flow fluctuations and oscillations that persisted throughout with constant frequency and amplitude which indicated that the flow was actually unsteady in nature with vortices shedding from the wake.

The force and moment coefficients were also calculated at each time step and presented in Figure 5-14 along with the steady state results. It is also shown that the coefficients quickly converge to a steady state solution.

3D unsteady calculations were also performed over a half 3D pitching ejection seat geometry. The half geometry was selected due to symmetry conditions and because of economic reasons. Note that calculations were also performed on a fixed half ejection seat geometry and the results were identical to those of the full geometry presented in Figure 5-13 and 5-14. For this case the initial conditions were the steady state converged solution. Two different simulations were performed that correspond to two different time steps and pitching angle increments. In each case the solution was run for 1 second and a pitching envelope from 0 to 45 degrees. In one case the pitching increment was 0.5

degrees while in the other case the increment was 0.1 degrees which correspond to a time step of 0.011 and 0.0022 seconds, respectively. The grid was automatically adjusted after the seat is pitched as was done for the 2D seat calculations. Also, the CFD-ACE moving grid capability was used to retain full conservation of the governing equation.

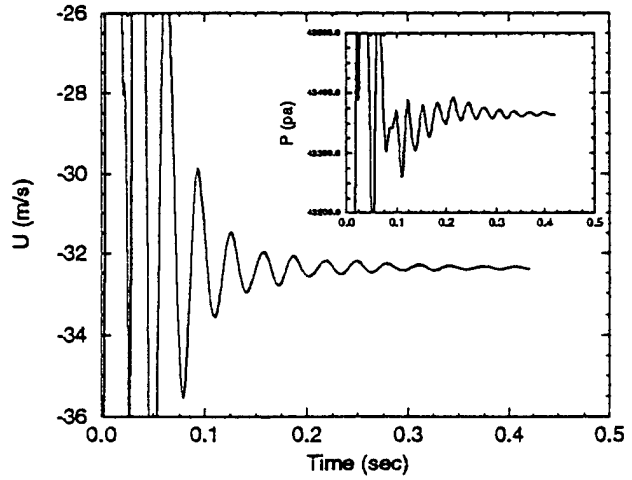

Figure 5-13. History of Velocity and Pressure at a Location Behind the 3D Full Ejection Seat Geometry

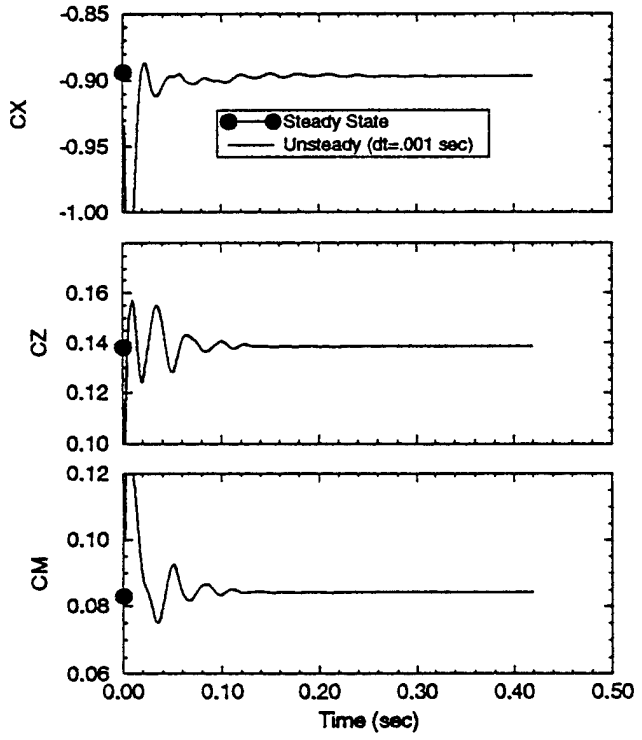

Figure 5-14. History of Aerodynamic Coefficients from 3D Ejection Seat Calculations

The force and momentum coefficients were calculated at each time step and are presented in Figure 5-15. The calculated steady state and unsteady results are virtually identical which seems to suggest that flow unsteadiness is negligible for both pitching angle increments. In fact, the solution from both unsteady calculations is exactly the same as shown in Figure 5-14 which means reducing the time step and pitching angle increment did not contribute to any flow unsteadiness. It should be mentioned that the 2D calculations on a pitching seat showed vortex shedding and flow oscillation developing after $\alpha = 25$ degrees for the increment of 0.1 degrees.

All of the 3D calculations so far produced no flow unsteadiness, vortex shedding or any perturbations. In every case the results converge to a steady state solution after a short time. Flow unsteadiness were expected to have much less of an effect on the aerodynamic characteristics of the seat in 3D than the previous 2D calculations showed. However, it is surprising that no flow oscillations or perturbations persisted for all the cases simulated no matter how small the time step used.

Reasons for the lack of flow unsteadiness in the 3D calculations are probably due to the coarseness of the grid used in the 3D calculations as compared to the 2D calculations.

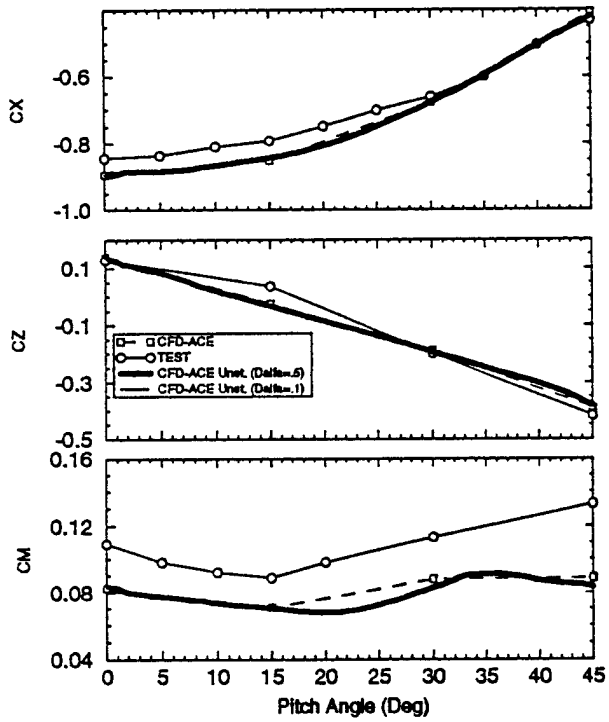

Figure 5-15. Aerodynamic Coefficients vs. Pitching Angle for Steady and Unsteady 3D Ejection Seat Simulations

5.4 Conclusions from Unsteady Simulations

Steady state and unsteady turbulent CFD simulations were performed on blunt-bodied type geometries with special interest in aircraft ejection seat geometries. The purpose of these simulations was to assess the importance of the unsteady flow effects on the calculated ejection aerodynamics characteristics. Simulations for a 2D cylinder geometry showed several characteristic, some of which persisted with a 2D mid-plane ejection seat geometry. These characteristics include: Selection of initial condition is critical to obtaining asymmetric solution with unsteady oscillations, and drag and lift coefficient values significantly differ between steady and time averaged unsteady solutions. The values of drag and lift coefficients are largely dependent on grid resolution and turbulence model used.

The 2D ejection seat results showed that the discrepancies between steady state and unsteady solution became smaller as the seat pitching angle increases and the wake size shrinks. Also, unsteady results for a rotating seat converge to a unique solution (irrespective of initial condition) if a small enough pitching angle and time step increments are used.

Limited unsteady analysis on a 3D ejection seat geometry showed no flow oscillation and resulted in aerodynamic coefficients similar to those of steady state. These results compared well to experiment (within 20%). To capture unsteady aerodynamic effects a much larger grid must be employed. At this time the anticipated benefit from these results does not justify the additional cost. For engineering purposes the 3D steady state results appear adequate